BODY WAVE SYNTHESIS FOR SHALLOW EARTHQUAKE SOURCES: INVERSION FOR SOURCE AND EARTH STRUCTURE PARAMETERS

Thesis by

Charles Adam Langston

In Partial Fulfillment of the Requirements

for Degree of

Doctor of Philosophy

California Institute of Technology

Pasadena, California

1976

(Submitted May 10, 1976)

Acknowledgments

I would like to thank the many people at the Seismological Laboratory, students and staff, who helped shape the ideas presented in this thesis. In particular, I owe thanks to Don Helmberger for suggesting the line of study that I have pursued. Larry Burdick and George Mellman provided many fruitful hours of discussion on inversion theory and source modelling which facilitated a greater understanding of the problems and pitfalls involved with these techniques.

I also thank Tom Heaton and Wayne Thatcher for providing critical reviews of the Koyna Earthquake study. Larry Burdick provided his well appreciated services by reviewing the chapter on the Puget Sound earthquake. To Dave Blum I owe special thanks for doing much of the hard work of digitizing and data processing for the Puget Sound study and whose enthusiasm was a major factor in formulating the final models for the earthquake.

I thank Barbara Sloan on her excellent job of typing the manuscript. Laszlo Lenches drafted nearly all of the figures contained in this thesis and proved to be a very helpful coordinator in the final stages of its completion.

A special note of appreciation goes to my wife, Kathleen, who persevered through the writing process and who provided much needed moral support and motivation.

This research was supported by the Advanced Research Projects Agency of the Department of Defense and was monitored by the Air Force Office of Scientific Research under Contract F44620-72-C-0078 and F44620-72C-0083. The author was also supported during the 1974-75 academic year by the Louis D. Beaumont Foundation Fellowship in Geophysics.

Abstract

Expressions for displacements on the surface of a layered half space due to an arbitrary oriented shear dislocation are given in terms of generalized ray expansions. Useful approximations of these expressions for shallow events as recorded at teleseismic distances for realistic earth models are presented. The results of this procedure are used to generate synthetic P, SV and SH waveforms for various assumptions of stress-drop. The Thomson-Haskell layer matrix method for computing far-field body wave displacements from shear dislocations is also formulated to complement the ray theory methods when complicated earth structures are considered. An iterative generalized inverse technique is developed using analytic partial derivatives for estimating source parameters from data sets of P and S seismograms from shallow earthquakes.

With the inverse technique and ray theory methods long period P and SH waveforms are analyzed from the Koyna, India, earthquake of 10 December 1967. Using published crustal models of the Koyna region and primarily by modelling the crustal phases P, pP, and sP, the first 25 seconds of the long-period waveforms are synthesized for 17 stations and a focal mechanism obtained for the Koyna earthquake which is significantly different from previous mechanisms. The fault orientation is 67° dip to the east, -29° rake plunging to the northeast, and N16°E strike, all angles ± 6°. This is an eastward

dipping, left-lateral oblique-slip fault which agrees favorably with the trend of fissures in the meizoseismal area. The source time duration is estimated to be 6.5 ± 1.5 sec, from a triangular time pulse which has a rise time of 2.5 sec and a tail-off of 3.9 sec, source depth of 4.5 ± 1.5 km, and seismic moment of $3.2 \pm 1.4 \times 10^{25}$ dyne-cm. Some short period complexity in the time function is indicated by modelling short-period WWSSN records but is complicated by crustal phases. The long-period P waveforms exhibit complicated behavior due to intense crustal phase interference caused by the shallow source depth and radiation pattern effects. These structure effects can explain much of the apparent multiplicity of the Koyna source. An interpretation of the Koyna dam accelerograms has yielded an S-P time. Taken together with the I. M. D. epicenter and present depth determination, it places the epicenter directly on the meizoseismal area.

Simultaneous modelling of source parameters and local layered earth structure for the April 29, 1965, Puget Sound earthquake was done using both the ray and layer matrix formulations. The source parameters obtained are: dip 70° to the east, strike 344°, rake -75°, 63 km depth, average moment of $1.4 \pm 0.6 \times 10^{26}$ dyne-cm, and a triangular time function with a rise time of 0.5 sec and fall-off of 2.5 sec. An upper mantle and crustal model for southern Puget Sound was determined from inferred reflections from interfaces above the

source. The main features of the model include a distinct 15 km thick low velocity zone with a 2.5 km/sec P wave velocity contrast lower boundary situated at approximately 56 km depth. The crustal model is less than 15 km thick with a substantial sediment section near the surface. A stacking technique using the instantaneous amplitude of the analytic signal is developed for interpreting short period teleseismic observations. The inferred reflection from the base of the low velocity zone is recovered from short period P and S waves. An apparent attenuation is also observed for pP from comparisons between the short and long period data sets. This correlates with the local surface structure of Puget Sound and yields an effective Q of approximately 65 for the crust and upper mantle.

To substantiate the unusual structure found from the Puget Sound waveform study the structure under Corvallis, Oregon, was examined using long period Ps and Sp conversions and P reverberations from teleseismic events as recorded at the WWSSN station COR. By modelling these phases in the time domain using a data set composed of six deep and intermediate depth earthquakes a similar low velocity zone structure is again inferred. The lower boundary occurs at 45 km depth and has S and P velocity contrasts of 1.3 and 1.4 km/sec, respectively. The material comprising the low velocity zone has a Poisson ratio of at least 0.33 and is constrained by the average P and S travel times determined from the converted phases.

TABLE OF CONTENTS

Introduction

The information contained in the seismic signature almost defies understanding because of complexities in both the seismic source and in the propagation of the resultant waves through the earth. Basic progress in understanding these processes usually comes not from developing new technologies but from reorganizing and clarifying existing ideas with, maybe, an extrapolation or two. This thesis will be concerned with an old problem in geophysics: given an earthquake seismogram, what can be said about the natural processes which formed it? In particular, we will be concerned about explaining the body wave radiation from shallow depth seismic sources by looking at the source from places on the earth where wave propagation effects are minimized, i.e., $30° < \Delta < 90°$. The existing ideas and techniques of radiation patterns and reflection seismology will be reorganized and cast into a form which will hopefully be useful in understanding shallow earthquakes where near surface structure effects are quite pronounced.

Shallow sources are interesting from several points of view. The most obvious is that the most devastating earthquakes are shallow, justifying any study of them in order to find their source processes. Secondly, a moderate sized shallow focus earthquake is a direct consequence of and can illuminate the geologic history of a region; a fact of increasing importance in the geologic sciences. Finally, the seismology itself can present previously unsuspected tools for deducing earth structure.

Since there is a basic duality between source and propagation effects, relatively sophisticated methods have to be employed in order to test hypotheses about either. In the first part of this work we will concentrate on developing the theory and practical methods for calculating body wave synthetic seismograms from dislocation sources imbedded in a layered elastic medium for comparison to the actual observed seismogram. The theory will then be used in subsequent chapters to deduce the source parameters of a shallow focus event and to determine near-source earth structure from another event.

Chapter 1 consists of three parts. The first part contains the theoretical development for calculating the total far-field response of an arbitrarily oriented shear dislocation point source in a layered elastic medium using the ray theory approach. This work appears in Langston and Helmberger (1975). The second section of Chapter 1 presents the same dislocation theory cast in the propagator matrix formulation. Each method has certain advantages over the other and, hence, are complimentary. The ray approach enables a full understanding of the problem through direct interpretation of ray arrival times and amplitudes; quantities which are directly measurable. Ray summation, however, becomes unwieldy and inconvenient for calculating the total response of sources in complicated structures. This is where the propagator matrix approach becomes desirable. Since the problem is formulated in the frequency domain, rather than the time domain as done with rays, the total response is simply a number

of matrix multiplications at each desired frequency. The resultant spectra are inverted via the Fourier Transform to obtain time domain seismograms. Taken by itself, however, the propagator matrix method only yields a mathematically correct answer with little physical insight into processes involved in the model.

The last part of Chapter 1 is concerned with formulating the inversion problem for estimating relevant source parameters from a set of data seismograms. This section contains standard linear inverse theory with emphasis on the numerical methods. In particular, analytic forms for the partial derivatives are presented as summarized by Langston (1976).

Chapter 2 illustrates the application of the dislocation and inversion theories through the analysis of the Koyna, India, earthquake of December 10, 1967, which appears in Langston (1976). This particular earthquake has been exceedingly problematical in yielding consistent focal parameters by other means, e.g., P first motions and surface waves. The Koyna event, however, provides an ideal vehicle for demonstrating the power of the theoretical methods and the underlying basic seismology of a very shallow earthquake.

Chapter 3 completes the conceptual framework of this thesis by considering the feasibility of using earthquake sources for deducing the local source earth structure. The Puget Sound earthquake of April 29, 1965, is modelled by considering both structure and source parameters simultaneously. The remarkable result of a substantial and very distinct low velocity zone in the uppermost

mantle under Puget Sound deduced from underside reflections is the principal conclusion of this chapter. To provide further constraints and credibility to this earth model the crust and upper mantle structure under Corvallis, Oregon, is examined by using teleseismic recordings of deep and intermediate focus events as recorded by the WWSSN station COR. Interpreting the times and amplitudes of Sp, Ps, and P phases through waveform synthesis yields a similar conclusion; again, a very substantial low velocity zone occurs in the uppermost mantle. These successful analyses are given as justification of the concept of analyzing simple earthquakes for earth structure determinations.

In addition to these chapters two Appendices are provided for involved mathematical treatments. Appendix I outlines the details of the Cagniard derivation from the dislocation source potentials to the first motion approximations discussed in Chapter 1. Appendix II contains the explicit forms for the analytic partial derivatives also discussed in Chapter 1.

Chapter 1

A PROCEDURE FOR MODELLING SHALLOW DISLOCATION SOURCES

Introduction

Application of body wave first-motions in seismic source studies has long been a standard tool in seismology. In fact, much of the bridge between seismology and geologic processes has been founded upon focal mechanisms inferred mostly from body wave interpretations. Stauder (1962) gives a good review of the history and techniques involved in the first-motion method. There are other parameters besides orientation which are of interest and have been pursued using various methods also involving body waves. These include such quantities and concepts as source time functions, directivity, and source multiplicty. Fukao (1970, 1972) has studied deep focus events by modelling their long period P and S waveforms, taking into account receiver structure, Q, and time function effects. Abe (1974) has tried to extend the same methods of waveform synthesis to the study of shallow crustal events where the assumption of homogeneous source structure, appropriate for deep events, is still used. Bollinger (1968), using assumptions on source time functions, directivity, and earth structure, interpreted long period P waveforms for the purpose of determining faulting direction in both deep and shallow events.

Closely related to time domain waveform methods are those which make extensive use of spectral analysis. Notably, Teng and Ben-Menahem (1965) using the methods outlined in Ben-Menahem, Smith, and Teng (1965) analyzed P and S waves from a deep focus Banda Sea event. This method is completely equivalent, of course, to modelling using time domain representations of structure, Q, etc. if the amplitude and phase spectra are both incorporated. In the last few years a simplified variation of Ben-Menahem et al. (1965) has become popular in conjunction with Brune's (1970) ideas on the behavior of the seismic source time functions. Hanks and Wyss (1972), making simplifying assumptions about earth structure, have outlined a spectral technique which compares an observed body wave spectrum to that of a Brune time function. Making assumptions about the relations between frequency content and source dimensions they obtain the stressdrop and moment for observed earthquakes.

In addition to these involved analysis techniques there are many studies of source mechanisms which include interpretations of the arrival time of observed phases. The "multiplet" technique (Oike, 1971), for instance, seems to be a simple, yet powerful method for determining source propagation effects in deep earthquakes. Very closely related are the ideas first put forth by Wyss and Brune (1967) on multiple sources. Interpreting various arrivals on short period observations from the Alaskan earthquake of March 28, 1964, as multiple sources, they established a seismological precedent in

source studies. Numerous authors studying other shallow events have appealed to such source complications in the same way, a few being Wu (1968), Niazi (1969), and Gupta et al. (1971).

Most of the techniques discussed above suffer some serious form of limitation by themselves or when a shallow crustal source is involved. First motions have an intrinsic difficulty in that the very first motion of an earthquake may have nothing to do with the rest of the earthquake. The spectral techniques involve a transformation from the time domain into the frequency domain so that the details and characteristics of the observed record become obscured and harder to interpret. The effect of local earth structure around the source is the largest unknown factor in all of the shallow source interpretations mentioned. It is nearly always neglected, but, as will be shown in this Chapter, is the most important and obvious feature of a shallow seismic source.

This Chapter will be concerned about the presentation of a general technique of modelling shallow dislocation sources embedded in a layered elastic medium by constructing synthetic seismograms. We will first derive the far field solution for the point dislocation problem using a generalized ray development, the Cagniard-de Hoop method, discussed by Helmberger (1974). Helmberger's results will be extended and generalized for a point dislocation of arbitrary orientation. Solutions involving dislocation sources and other types of point-force configurations have been treated this way by many authors with varying

degrees of applicability to seismological problems. A partial list of recent contributors include Muller (1969), Sato (1972), Ben-Menahem and Vered (1973), and Johnson (1974). However, for the problem at hand, involved numerical contour integrations can be avoided by considering the valid and simple first motion approximations. These are equivalent to plane wave ray theory solutions except for geometrical spreading corrections for phase conversions near the source.

The second portion of this chapter will deal with formulating the far-field body wave solutions in terms of Thomson-Haskell propagator matrices. In particular, the notation and methods of Harkrider (1964) and Fuchs (1966) will be used to obtain identical results to the ray formulation. Other investigations have formulated this particular problem somewhat differently but still using frequency domain methods, notably, Hudson (1969a, 1969b) and Fukao (1971). Even though the mathematics for these methods have been around for several years very little modelling or data inversion has been done. It is my contention that both the propagator matrix and ray techniques should be used together to effect the greatest understanding for the problems involved. One possible reason for the delayed practical use of propagator matrix methods is the shear obtuseness of trying to visualize a series of ray transmissions and reflections in the frequency domain. Transforming the spectra

back into the time domain certainly helps, but little can be gained if, for example, the modeller cannot identify the portion of the earth model where a particular phase originated.

The last part of this chapter will be concerned with formulating the inversion problem for body wave forms. That is: given a set of P and S wave forms from stations distributed azimuthally and in distance from an earthquake and having previous estimates for the local source earth structure, what source parameters, e.g., time function, orientation, and depth, satisfy the data best? We will use Wiggin's (1972) generalized inverse techniques and an important contribution from Mellman, Burdick, and Helmberger (1975) for describing the comparison of the observed seismogram with a synthetic. The principal contribution that this section presents to the source estimation problem comes from finding analytic forms for the partial derivatives.

Ray Theory for the Point Shear Dislocation

In this section, we will cover the model assumptions and the full expressions for an arbitrarily oriented point dislocation in a layered medium.

The first and commonly held assumption is that shallow earthquakes, epicentral depths less than 100 km, are caused by movements along faults, very thin planar zones of weakness. Using this precept, we can specify the entire problem of calculating elastic displacements from this kind of source by use of a finite continuous displacement

dislocation in a homogeneous elastic medium. By use of the Green's function solution or representation theorem for movements at a closed surface in an infinite elastic space, one can avoid the problem, somewhat, of nonlinear processes at the fault. By placing this surface around the fault zone and saying that each side 'knows' what the other is doing (continuity of stress), including a particular fault surface geometry, one can construct the solution for displacements everywhere in the medium given the displacements on the hypothetical surface around the fault. In practice, and mathematically, we assume this surface is very close to the fault and reflects exactly what the real movements are along the fault. This, of course, must be borne out eventually by observations on source finiteness.

Following De Hoop's (1958) form of the elastodynamic representation theorem Harkrider (1975) has produced displacement potentials for a rectangular point shear dislocation in an infinite elastic medium. In terms of the wave number, k, and circular frequency, ω, for an arbitrarily oriented dislocation with the co-ordinate system of Fig. 1.1, these are:

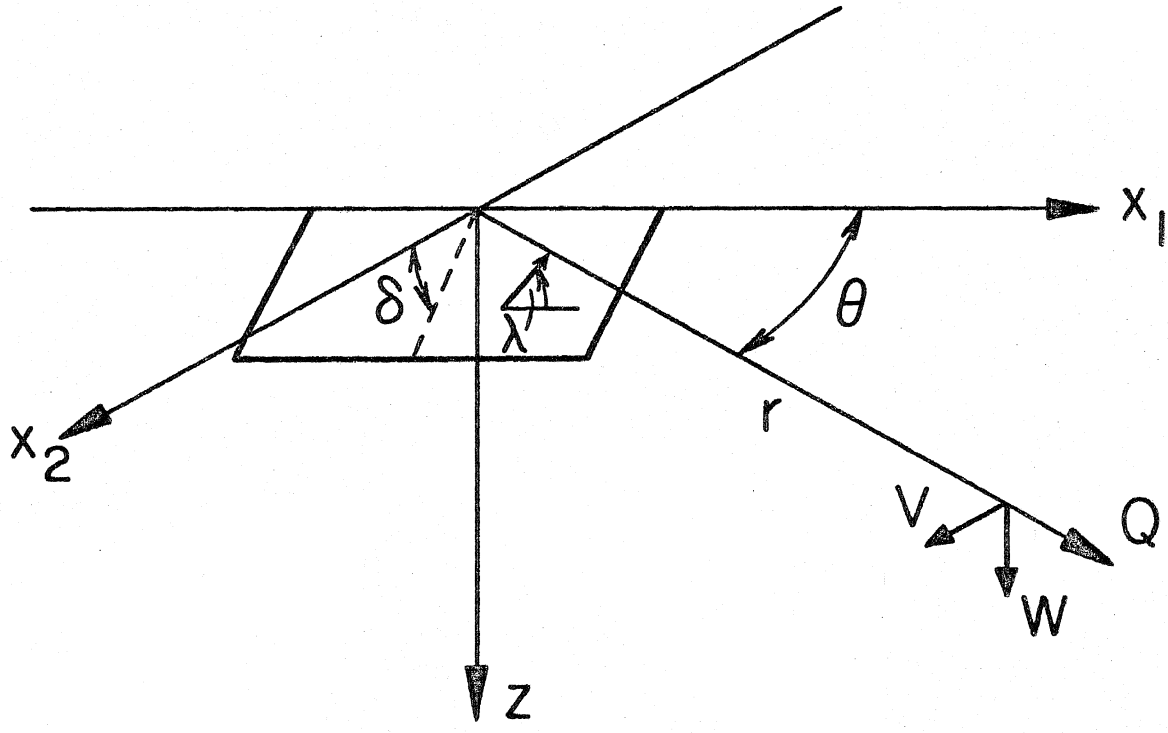

Figure 1.1. Coordinate system for the dislocation formulation. z is positive downwards.

P potential

$$\bar{\phi} = -K \int_0^\infty k^2 F_\alpha J_2(kr)dk . A_1(\theta, \lambda, \delta)$$

$$+K \int_0^\infty 2k\varepsilon F_\alpha \nu_\alpha J_1(kr)dk . A_2(\theta, \lambda, \delta)$$

$$+K \int_0^\infty (2k_\alpha{}^2 - 3k^2) F_\alpha J_0(kr)dk . A_3(\theta, \lambda, \delta).$$

SV potential

$$\bar{\psi} = -K \int_0^\infty \varepsilon\nu_\beta F_\beta J_2(kr)dk . A_1(\theta, \lambda, \delta)$$

$$-K \int_0^\infty \frac{(k_\beta{}^2 - 2k^2)}{k} F_\beta J_1(kr)dk . A_2(\theta, \lambda, \delta)$$

$$-K \int_0^\infty 3\varepsilon F_\beta \nu_\beta J_0(kr)dk . A_3(\theta, \lambda, \delta). \qquad (1.1)$$

SH potential

$$\bar{\chi} = +K \int_0^\infty k_\beta{}^2 F_\beta J_2(kr)dk . A_4(\theta, \lambda, \delta)$$

$$-K \int_0^\infty \frac{k_\beta{}^2}{k} \varepsilon F_\beta \nu_\beta J_1(kr)dk . A_5(\theta, \lambda, \delta)$$

where

α = compressional wave velocity

β = shear wave velocity

$k_v = \omega/v$

$\nu_v = (k^2 - k_v^2)^{\frac{1}{2}}$

$$F_v = \frac{k \exp(-\nu_v|z-h|)}{\nu_v}$$

h = depth to source

$$K = -\frac{\mu L H \bar{D}(\omega)}{4\pi\rho\omega^2}$$

μ = shear modulus at the source,

ρ = density at the source,

$$\varepsilon = \begin{cases} +1 & z > h \\ -1 & z < h, \end{cases}$$

L = fault length,

H = fault height,

$\bar{D}(\omega)$ = transformed dislocation time function,

$$\left.\begin{aligned} A_1(\theta,\lambda,\delta) &= \sin 2\theta \cos\lambda \sin\delta + \tfrac{1}{2}\cos 2\theta \sin\lambda \sin 2\delta, \\ A_2(\theta,\lambda,\delta) &= \cos\theta \cos\lambda \cos\delta - \sin\theta \sin\lambda \cos 2\delta, \\ A_3(\theta,\lambda,\delta) &= \tfrac{1}{2}\sin\lambda \sin 2\delta, \\ A_4(\theta,\lambda,\delta) &= \cos 2\theta \cos\lambda \sin\delta - \tfrac{1}{2}\sin 2\theta \sin\lambda \sin 2\delta, \\ A_5(\theta,\lambda,\delta) &= -\sin\theta \cos\lambda \cos\delta - \cos\theta \sin\lambda \cos 2\delta, \end{aligned}\right\} \qquad (1.2)$$

θ = strike from the end of the fault plane,

λ = rake angle,

δ = dip angle.

The displacements in the medium are given by:

$$\left.\begin{aligned} \bar{W}(r,z,\theta,\omega) &= \frac{\partial\bar{\phi}}{\partial z} + \frac{\partial^2\bar{\psi}}{\partial z^2} + k_\beta^2\bar{\psi} \\ \bar{V}(r,z,\theta,\omega) &= \frac{1}{r}\frac{\partial\bar{\phi}}{\partial\theta} + \frac{1}{r}\frac{\partial^2\bar{\psi}}{\partial z\partial\theta} - \frac{\partial\bar{\chi}}{\partial r} \\ \bar{Q}(r,z,\theta,\omega) &= \frac{\partial\bar{\phi}}{\partial r} + \frac{\partial^2\bar{\psi}}{\partial r\partial z} + \frac{1}{r}\frac{\partial\bar{\chi}}{\partial\theta}. \end{aligned}\right\} \qquad (1.3)$$

The first, second, and third terms of the P-wave and SV-wave potentials, excluding the angle terms, A_i, correspond to a vertical strike-slip dislocation, a vertical dip-slip dislocation, and a dislocation dipping at 45° seen at 45° azimuth, respectively. The SH potential contains the vertical strike-slip and vertical dip-slip dislocations, respectively. This order will be kept throughout this thesis.

Changing variables into a form more convenient for generalized ray theory, that is, k into p, the ray parameter, and ω into s, the Laplace Transform variable, we obtain:

P-waves

$$\hat{\phi} = -\frac{M_0}{4\pi\rho}\frac{2}{\pi} Im \int_0^{+i\infty} \frac{p^3}{\eta_\alpha} \exp(-s\eta_\alpha|z-h|) K_2(spr) dp . A_1(\theta, \lambda, \delta)$$
$$+ \frac{M_0}{4\pi\rho}\frac{4}{\pi}\varepsilon Im \int_0^{+i\infty} p^2 \exp(-s\eta_\alpha|z-h|) K_1(spr) dp . A_2(\theta, \lambda, \delta)$$
$$- \frac{M_0}{4\pi\rho}\frac{2}{\pi} Im \int_0^{+i\infty} \left(\frac{2}{\alpha^2} - 3p^2\right)\frac{p}{\eta_\alpha} \exp(-s\eta_\alpha|z-h|) K_0(spr) dp . A_3(\theta, \lambda, \delta).$$

SV-waves

$$\hat{\Omega} = -\frac{M_0}{4\pi\rho}\frac{2}{\pi}\varepsilon Im \int_0^{+i\infty} p^2 \exp(-s\eta_\beta|z-h|) K_2(spr) dp . A_1(\theta, \lambda, \delta)$$
$$- \frac{M_0}{4\pi\rho}\frac{2}{\pi} Im \int_0^{+i\infty} \frac{(2p^2 - (1/\beta^2))}{\eta_\beta} p \exp(-s\eta_\beta|z-h|) K_1(spr) dp . A_2$$
$$+ \frac{M_0}{4\pi\rho}\frac{6}{\pi}\varepsilon Im \int_0^{+i\infty} p^2 \exp(-s\eta_\beta|z-h|) K_0(spr) dp . A_3.$$

SH-waves

$$\hat{\chi} = +\frac{M_0}{4\pi\rho}\frac{2}{\pi}\frac{1}{\beta^2} Im \int_0^{+i\infty} \frac{p}{\eta_\beta} \exp(-s\eta_\beta|z-h|) K_2(spr) dp . A_4$$
$$- \frac{M_0}{4\pi\rho}\frac{2}{\pi}\frac{\varepsilon}{\beta^2} Im \int_0^{+i\infty} \exp(-s\eta_\beta|z-h|) K_1(spr) dp . A_5 \qquad (1.4)$$

where the following transformations have been made,

$$\omega = -is$$
$$k = -isp$$
$$\hat{\Omega} = -sp\hat{\psi}, \quad SV \text{ potential transformation}$$
$$M_0 = LHD_0\,\mu, \quad \text{fault moment}$$
$$\hat{D}(s) = \frac{D_0}{s}, \quad \text{a step function weighted by } D_0$$
$$\eta_v = \left(\frac{1}{v^2} - p^2\right)^{\frac{1}{2}}$$
$$\hat{} = \text{Laplace transformed}$$

The nature of the variable changes and SV potential transformation is discussed in Helmberger (1974). The displacements after these transformations are:

$$\left.\begin{aligned} \hat{W} &= \frac{\partial\hat{\phi}}{\partial z} + sp\hat{\Omega} \\ \hat{V} &= \frac{1}{r}\frac{\partial\hat{\phi}}{\partial\theta} - \frac{1}{spr}\frac{\partial^2\hat{\Omega}}{\partial z\partial\theta} - \frac{\partial\hat{\chi}}{\partial r} \\ \hat{Q} &= \frac{\partial\hat{\phi}}{\partial r} - \frac{1}{sp}\frac{\partial^2\hat{\Omega}}{\partial r\partial z} + \frac{1}{r}\frac{\partial\hat{\chi}}{\partial\theta}. \end{aligned}\right\} \qquad (1.5)$$

The potential forms (1.4) are well suited in calculations involving layered structure since one just multiplies the appropriate generalized reflection coefficients into the integrals before evaluation. Our expressions can be further simplified by using the asymptotic expansion for the modified Bessel functions.

We have:

$$\left.\begin{aligned}
\hat{\phi} &= \frac{M_0}{4\pi\rho}\sum_{j=1}^{3} A_j(\theta,\lambda,\delta)\frac{2}{\pi}Im\int_0^{+i\infty} C_j\frac{p}{\eta_\alpha}\sqrt{\left(\frac{\pi}{2spr}\right)} \\
&\qquad \times\exp\left(-s(pr+\eta_\alpha|z-h|)\right)dp \\
\hat{\Omega} &= \frac{M_0}{4\pi\rho}\sum_{j=1}^{3} A_j(\theta,\lambda,\delta)\frac{2}{\pi}Im\int_0^{+i\infty} SV_j\frac{p}{\eta_\beta}\sqrt{\left(\frac{\pi}{2spr}\right)} \\
&\qquad \times\exp\left(-s(pr+\eta_\beta|z-h|)\right)dp \\
\hat{\lambda} &= \frac{M_0}{4\pi\rho}\sum_{j=1}^{2} A_{(j+3)}(\theta,\lambda,\delta)\frac{2}{\pi}Im\int_0^{+i\infty} SH_j\frac{p}{\eta_\beta}\sqrt{\left(\frac{\pi}{2spr}\right)} \\
&\qquad \times\exp\left(-s(pr+\eta_\beta|z-h|)\right)dp
\end{aligned}\right\} \qquad (1.6)$$

where

$$\left.\begin{aligned}
&C_1 = -p^2 && SV_1 = -\varepsilon p\eta_\beta && SH_1 = \frac{1}{\beta^2} \\
&C_2 = 2\varepsilon p\eta_\alpha && SV_2 = (\eta_\beta{}^2 - p^2) && SH_2 = -\frac{\varepsilon}{\beta^2}\frac{\eta_\beta}{p} \\
&C_3 = (p^2 - 2\eta_\alpha{}^2) && SV_3 = 3\varepsilon p\eta_\beta.
\end{aligned}\right\} \qquad (1.7)$$

One final form which is useful is the first motion approximation. This approximation supposes that the above functions can be taken outside the integral and evaluated at the appropriate ray parameter yielding the standard vertical radiation patterns (see Knopoff and Gilbert 1959; Helmberger 1974). Transforming into the time domain, these forms become:

$$\left.\begin{aligned}
\phi &= \frac{M_0}{4\pi\rho}\sum_{j=1}^{3} A_j(\theta,\lambda,\delta)C_j\frac{H(t-(R/\alpha))}{R} \\
\Omega &= \frac{M_0}{4\pi\rho}\sum_{j=1}^{3} A_j(\theta,\lambda,\delta)SV_j\frac{H(t-(R/\beta))}{R} \\
\chi &= \frac{M_0}{4\pi\rho}\sum_{j=1}^{2} A_{j+3}(\theta,\lambda,\delta)SH_j\frac{H(t-(R/\beta))}{R}
\end{aligned}\right\} \qquad (1.8)$$

where

H(t - (R/V)) = step function delayed by travel time R/V,

R = distance the ray travels.

Corrected phases such as the pulse pS can be written,

$$\hat{\Omega} = \frac{M_0}{4\pi\rho}\sum_{j=1}^{3} A_j(\theta,\lambda,\delta)\frac{2}{\pi}Im\int_0^{i\infty} C_j R_{PS}\frac{p}{\eta_\alpha}\sqrt{\left(\frac{\pi}{2spr}\right)} \times\exp\left(-s(pr+\eta_\alpha z_0+\eta_\beta z)\right)dp \qquad (1.9)$$

as discussed by Helmberger (1974). Performing the first motion approximation this expression reduces to:

$$\Omega = \frac{M_0}{4\pi\rho}\sum_{j=1}^{3} A_j(\theta,\lambda,\delta)\,C_j\left(R_{PS}\frac{\eta_\beta}{\eta_\alpha}\right)\frac{H(t-R/\beta)}{R}. \qquad (1.10)$$

Similar expressions for the other converted phases are easily expressed in the same manner by including the appropriate ratio of η_v's along with the generalized reflection or transmission coefficient. The ratio of η_v's was omitted in the earlier study (Helmberger, 1974),

which led to over-emphasized sP contributions. The exact details of the preceding analysis are covered in Appendix I for the specific case of the strike-slip P potential. These first motion results are useful for wave calculations when the signal duration is short compared to the travel times and will be the basis for all ray calculations in the remaining parts of this thesis.

Shallow source modelling 30° - 90°

Ben-Menahem, Smith and Teng (1965) have given a very thorough discussion of the procedures used for body-wave analysis of deep and intermediate depth earthquakes. Essentially, the methods outlined here are very similar except for the important and justifiable difference of including the earth structure effect through the use of potentials and reflection-transmission coefficients.

We introduce our technique of categorizing the various effects by means of a representative calculation.

Consider the problem setup displayed in Fig. 1.2 where the goal is to produce a P-wave synthetic seismogram at the receiver for the rays shown. The total vertical response at the receiver can be given by the following equation:

$$W = R_{PZ}\left[\dot{\phi} + R_{PP}\dot{\phi}\cdot H(t-\Delta t_1) + \left(R_{SP}\frac{\eta_\alpha}{\eta_\beta}\right)\dot{\Omega}\cdot H(t-\Delta t_2)\right] * S(t) * I(t) * Q(t) \qquad (1.11)$$

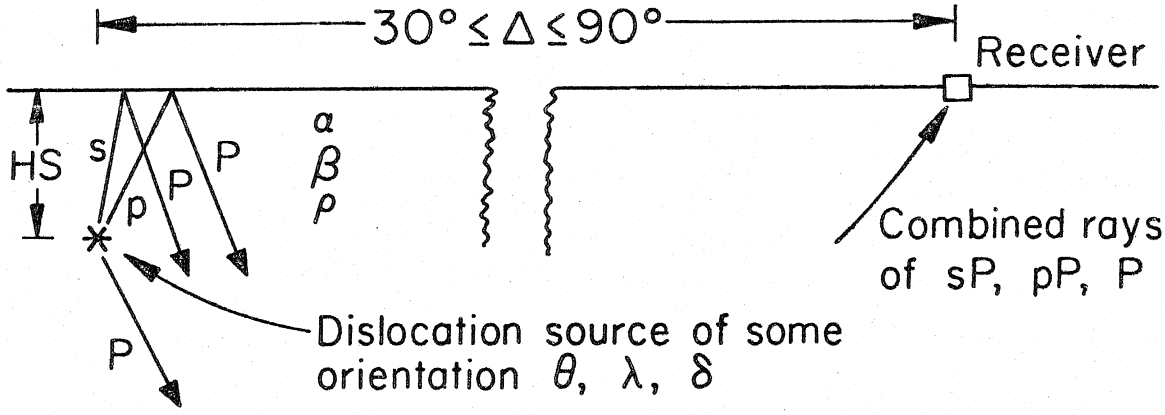

Figure 1.2. Schematic representation of equation (1.11).

where

R_{PZ} = vertical P-wave receiver function
R_{PP} = reflection coefficient for pP
R_{SP} = reflection coefficient for sP
$S(t)$ = far-field dislocation time function
$I(t)$ = impulse response of an instrument
$Q(t)$ = Q operator
$*$ = convolution operator
Δt_1 = time lag of pP relative to the direct wave
Δt_2 = time lag of sP relative to the direct wave
$H(t-\Delta t)$ = lagged Heaviside step function.

Remember that z is positive downward. Note also that the SV potential, Ω, appears in this P-wave calculation since it must serve as an amplitude weighting function for the ray sP. In practice, for these ranges, one ray parameter is used for all near source interactions. For shallow sources the error introduced by this approximation is negligible. For the same ray parameter then, we have the time lags given simply as

$$\left.\begin{aligned} \Delta t_1 &= 2HS\eta_\alpha \\ \Delta t_2 &= HS(\eta_\beta+\eta_\alpha). \end{aligned}\right\} \qquad (1.12)$$

For an arbitrary layered medium the problem becomes one of simply specifying the path of the ray through the layers. The amplitude will be given as a product of reflection and transmission coefficients weighted by the appropriate wave potential. The relative travel time

will be given by

$$\Delta t = \sum_i \left(n_i \cdot Th_i \ \eta_{v_i} \right) \tag{1.13}$$

where i is the layer index and n_i the total number of ray legs in the layer of a particular mode, P or S.

The reflection and transmission coefficients are those used by Helmberger (1968) and, in this case, are simple multiplicative constants. If evaluated inside the integrals (1.7) or (1.4), as the general case, a range of complex ray parameters defined by the Cagniard contour is used.

The far-field time function, S(t), is the derivative of the actual dislocation displacement time function. This comes about by setting $\hat{D}(s) = D_o/s$ in (1.4) to get the step-function response of the potentials. The impulse response, which is needed for the convolution operations, is simply the time derivative. For convenience, and by superposition, we do this derivative on the displacement time function to give the far-field time function. Also, since we weighted the step-function response by D_o, the final offset, we must set the final offset of each displacement time function used to be unity.

Denoting the displacement time function by f(t), this corresponds to:

$$\int_{-\infty}^{+\infty} \frac{\partial f(t)}{\partial t} dt \equiv \int_{-\infty}^{+\infty} S(t) dt \equiv 1. \tag{1.14}$$

The fault moment, M_o, contained in the potentials (1.4), (1.7) and (1.8), is taken to be expressed in the conventional units of dyne-cm and density, ρ, in g cm^{-3}.

The instrument response, I(t), is usually normalized to one of its particular frequency components. For example, using Hagiwara's (1958) equations, one can construct the instrument response for the 15-100 WWSSN long-period instrument, such that the amplitude of the 15-s period spectral component is equal to unity. This form is used in all the synthetic seismogram calculations of this section.

Futterman's Q operator (1962) using a constant T/Q ratio (Carpenter, 1966) will be the basis for the Q(t) term in all calculations. It has the property of preserving pulse area so that no scaling problems arise from using it.

In the frequency domain, this operator is given explicitly as

$$\bar{Q}(\omega) = e^{-\frac{\omega T}{2Q_o}\left\{1 - e^{-x}\right\} + i\frac{\omega T}{\pi Q_o}\ln\gamma x} \qquad (1.15)$$

where,

T = average travel time

Q_o = average quality factor over the ray path

γ = 0.5772157..., Euler's constant

$x = \omega/\omega_o$

ω_o = low frequency cutoff.

In use, x is much greater than fifteen so that the 'e^{-x}' term in equation 1.15 can be ignored.

The receiver functions R_{PZ}, R_{PR}, R_{SZ} and R_{SR} are explicitly given in Helmberger (1974) and behave as simple real functions of p over the ranges considered. The letter index of this notation indicates the wave type and receiver component, respectively. A fifth receiver function defined by $R_T = (2p)$ describing the tangential displacement at the free surface is added for completeness, see expressions (1.5). Table 1.1 shows the variations expected in these functions for different receiver crust models and ranges. The table is made with z positive upwards. As can be seen, these functions are fairly slow varying over these ranges.

The expressions for the potentials were derived for a homogeneous earth with the spreading term (1/R). The effective (1/R) for a real earth is somewhat smaller, see Fig. 1.3, and can be approximated by the method used by Helmberger (1973a). The amplitudes were measured directly from synthetic step function responses generated from an earth-flattened Jeffreys-Bullen model and plotted versus range. This curve is equivalent to a smoothed geometrical optics calculation and contains some theoretical uncertainty as pointed out by Chapman (1974). There is also the problem of earth structure uncertainty which could easily produce significant wave-shape distortions. We will neglect these interesting problems here and

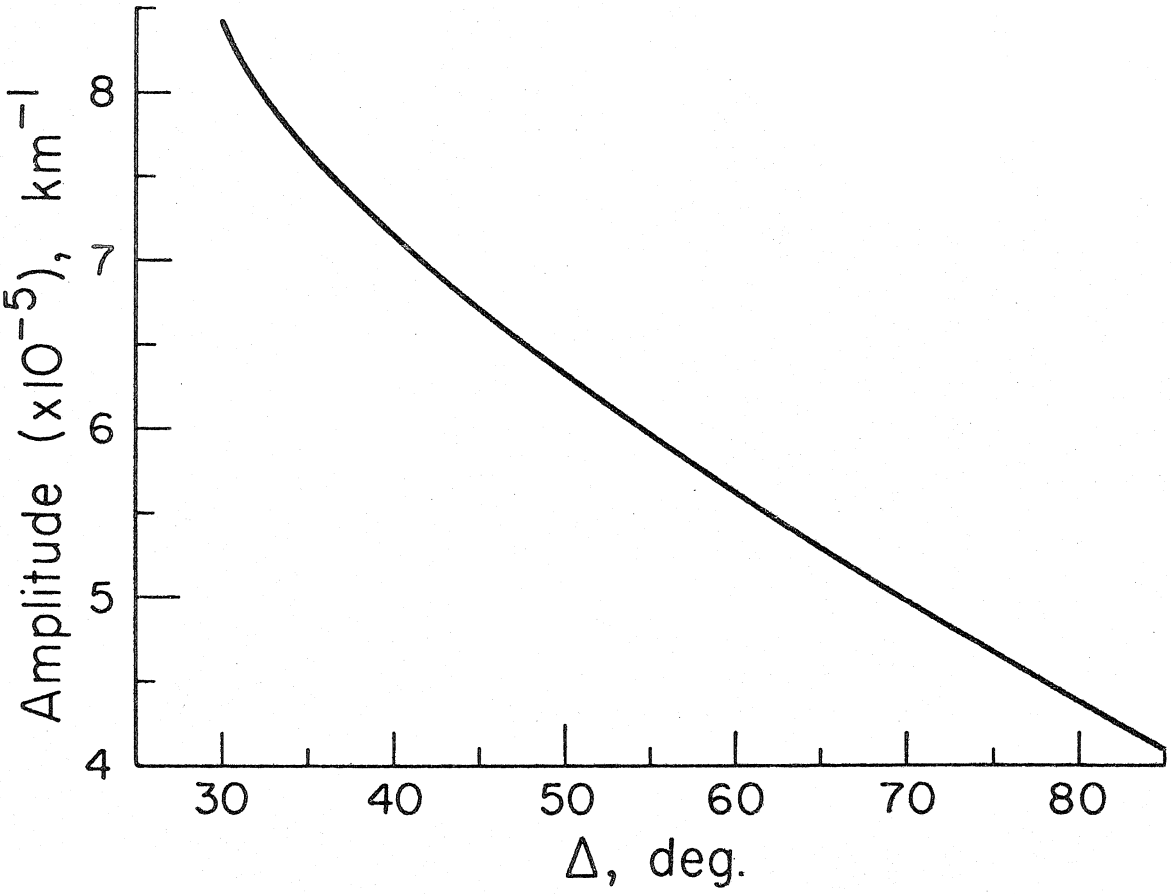

Figure 1.3. Graph of the effective 1/R decay in a Jeffreys-Bullen spherical earth.

Table 1.1

Evaluation of the receiver functions for various ray parameters and crustal models

Crust Model	$\Delta^{(0)}$	p (P-waves)	p (S-waves)	R_{PZ}	R_{PR}	R_{SZ}	R_{SR}	R_T
α = 6.0	90°	0.040	0.069	-0.321	-0.093	-0.158	0.545	0.138
β = 3.5	60°	0.060	0.104	-0.306	-0.138	-0.231	0.511	0.208
	30°	0.080	0.139	-0.285	-0.182	-0.288	0.484	0.278
α = 5.5	90°	0.040	0.069	-0.353	-0.093	-0.158	0.600	0.138
β = 3.2	60°	0.060	0.104	-0.339	-0.138	-0.232	0.570	0.208
	30°	0.080	0.139	-0.320	-0.182	-0.296	0.536	0.278
α = 5.0	90°	0.040	0.069	-0.390	-0.092	-0.158	0.667	0.138
β = 2.9	60°	0.060	0.104	-0.378	-0.138	-0.234	0.640	0.208
	30°	0.080	0.139	-0.036	-0.182	-0.301	0.605	0.278

concentrate on waveshapes produced by the source and accompanying surface reflections. This curve was constructed by using a compressional velocity of 6.5 km/sec and shear velocity of 3.5 km/sec for the surface crustal layer. For other source layer velocities and depths consider Figure 1.3 to be generated from classical geometrical spreading theory by using the following equation on a hypothetical set of smoothed ray paramters (Bullen, 1965)

$$C_o^2 = \frac{\rho_1 v_1}{\rho_o v_o} \frac{v_1}{r_o^2 r_1} \frac{\text{Tan } i_1}{\cos i_o \sin \Delta} \left| \frac{d^2T}{d\Delta^2} \right| \qquad (1.16)$$

where,

C_o^2 = squared amplitude spreading factor

r_o = radius of the earth

r_1 = radius that the source is situated at

i_1 = vertical takeoff angle at the source

i_o = vertical takeoff angle at the receiver

Δ = range in degrees

$\frac{d^2T}{d\Delta^2}$ = second derivative of the travel time curve

The amplitude adjustment factor for a different source depth and layer velocity is then given by

$$C_R^2 = \frac{C_o^2\big|_n}{C_o^2\big|_o} = \frac{\rho_{s_n} v_{s_n}}{\rho_{s_o} v_{s_o}} \frac{r_n^2}{r_o^2} \frac{\text{Tan } i_{s_n}}{\text{Tan } i_{s_o}} \tag{1.17}$$

where the 's' subscript stands for 'source' and 'n' and 'o' stand for 'new' and 'old', respectively. The multiplicative correction factor for Figure 1.3 is therefore

$$C_R = \frac{v_{s_n} r_n}{v_{s_o} r_o} \sqrt{\frac{\rho_{s_n} \text{Tan } i_{s_n}}{\rho_{s_o} \text{Tan } i_{s_o}}} \tag{1.18}$$

Source time function scaling for the synthetic seismogram calculation

Making certain assumptions about the seismic source one can derive scaling laws for the source time function which include parameters such as stress-drop, fault moment, and corner frequencies, see Brune (1970). The basic relationship is that the ratio of fault displacement, D_o, to fault dimension, r, is proportional to the ratio of stress drop, σ, to μ, the rigidity. We can derive Brune's results rather easily from shear dislocation theory. Starting with the SH potential, χ, of equation (1.8), assuming a vertical strike-slip fault ($\delta = 90°$, $\lambda = 0°$), and taking the necessary derivative indicated by (1.5) we get for the far-field tangential displacement

$$v = \frac{M_0}{4\pi\rho} \frac{1}{\beta^3} R_{\phi\theta} \frac{\delta(t-(R/\beta))}{R} \tag{1.19}$$

where we have set $R_{\phi\theta}$ = sin ϕ cos 2θ, the radiation pattern. The sin term comes from the relation p = sin ϕ/β, where ϕ is the take-off angle from vertical. Assuming the far-field time history discussed above, we have

$$v = \frac{M_0}{4\pi\rho}\frac{1}{\beta^3}R_{\phi\theta}\left(\frac{1}{R}\right)\frac{\partial f(t-(R/\beta))}{\partial t}. \tag{1.20}$$

For an assumed Brune time history, this leads to

$$\frac{\partial f}{\partial t} = \alpha^2 t \exp(-\alpha t) \tag{1.21}$$

and assuming a circular fault (Keilis-Borok, 1960)

$$v = R_{\phi\theta}\left(\frac{\sigma}{\mu}\right)\beta\left(\frac{r}{R}\right)t\exp(-\alpha t)\ . \tag{1.22}$$

By further assuming that

$$\alpha = \sqrt{\left(\frac{(7\pi)}{2}\right)\left(\frac{\beta}{r}\right)}\ , \tag{1.23}$$

the spectrum corresponding to (1.22) is simply

$$\Omega(\omega,\theta,\phi,R) = R_{\phi\theta}\left(\frac{\sigma}{\mu}\right)\beta\left(\frac{r}{R}\right)\left(\frac{1}{\omega^2+\alpha^2}\right) \tag{1.24}$$

which leads to the 'corner frequency' phenomenon. Generally speaking then, this model says that the frequency of the time function is inversely proportional to the fault dimension; the longer the fault

(or lower the stress-drop) the longer the time function lasts. We will incorporate this idea in a semiquantitative way in the discussion of the synthetic seismograms.

The far-field source time function assumed here will be a trapezoid of unit height described by three time parameters, δt's. The time length of the positive, zero and negative slopes will be represented by δt_1, δt_2, and δt_3, respectively. These three δt's allow relative time scaling of such things as rise time, fault duration, and stopping time. This time function will be normalized by the convention assumed, that is, of equation (1.14).

Synthetic seismograms

Synthetic seismograms were computed for P, SV and SH waves for a point dislocation source in a half-space using relations (1.8) after the method described by equation (1.11). The half-space model has a compressional velocity of 6.0 km s^{-1}, shear velocity of 3.5 km s^{-1}, and density equal to 2.7 g cm^{-3}. The distance from the source was taken as 80° which corresponds to a ray parameter of about 0.05 for P-waves and about 0.087 for S-waves.

For P-waves a constant T/Q ratio of 1.0 was used in Futterman's Q operator, Helmberger (1973b). For S-waves a conservative estimate of T/Q = 3.0 was used.

The impulse response for the 15-100 WWSSN instrument was used in all calculations.

Each of the respective sets of synthetic seismograms, P, SV and

SH of Figs. 1.4, 1.5, and 1.6 are arrayed with the purpose of showing the contribution and effect of each of the jth terms of equation (1.8). Each one of these terms (j = 1, 2, 3) can be given a separate physical interpretation. Not considering the radiation pattern, A_j, j = 1 represents a vertical strike-slip fault, j = 2 a vertical dip-slip fault, and j = 3 a 45° dipping dip-slip fault as seen at 45° azimuth. To produce any other oriented point dislocation, one just multiplies the appropriate A_j for each orthogonal term and sums. This particular orthogonality relationship came originally from the way the Green's function solution grouped together as double-couple representations.

The P waveforms all contain the direct wave and the surface interactions pP and sP as described by equation (1.11). Likewise, by analogous calculations, the SV waveforms contain S, sS and pS and the SH waveforms S and sS. The left-hand side of each diagram contains a representation of the medium impulse response for the source depth considered. The relative spike height corresponds to the weights of the delta functions. In each column to the right are the synthetic seismograms obtained by convolving in the instrument, Q, and the particular source time function considered. The 'stress-drop' connotation used here is a very simple one based on the length of the time function as discussed before. Table 1.2 displays the time function parameters used for the various designated stress-drop calculations.

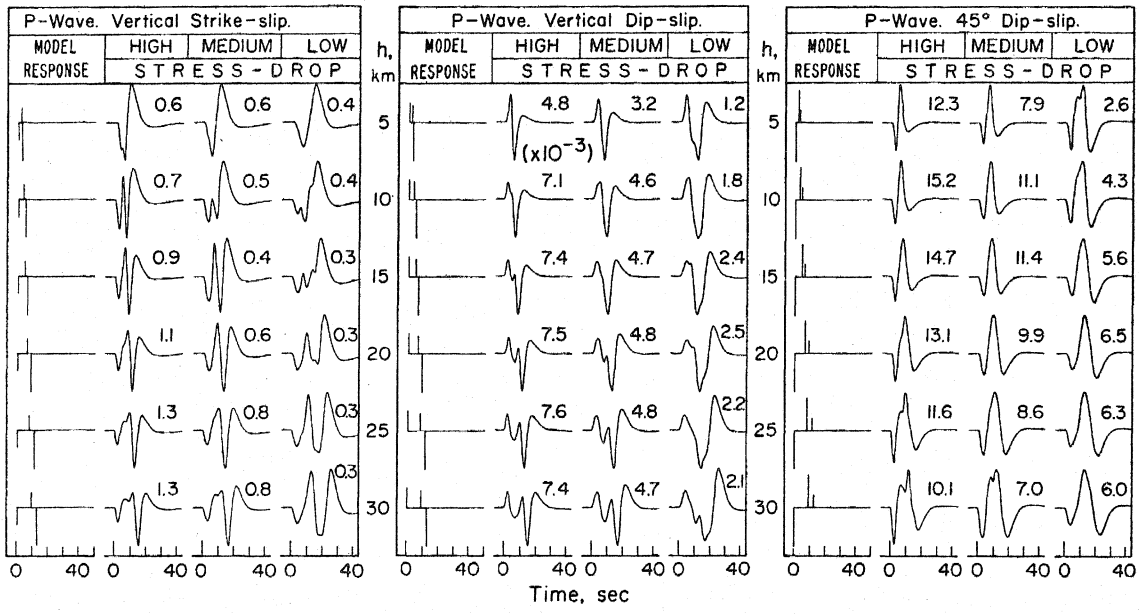

Figure 1. 4. P-wave synthetic seismograms for the three potential terms with varying depth and time functions. The numbers to the upper right are actual potential amplitudes without the moment $1/4\pi\rho$, 1/R decay, and receiver functions included.

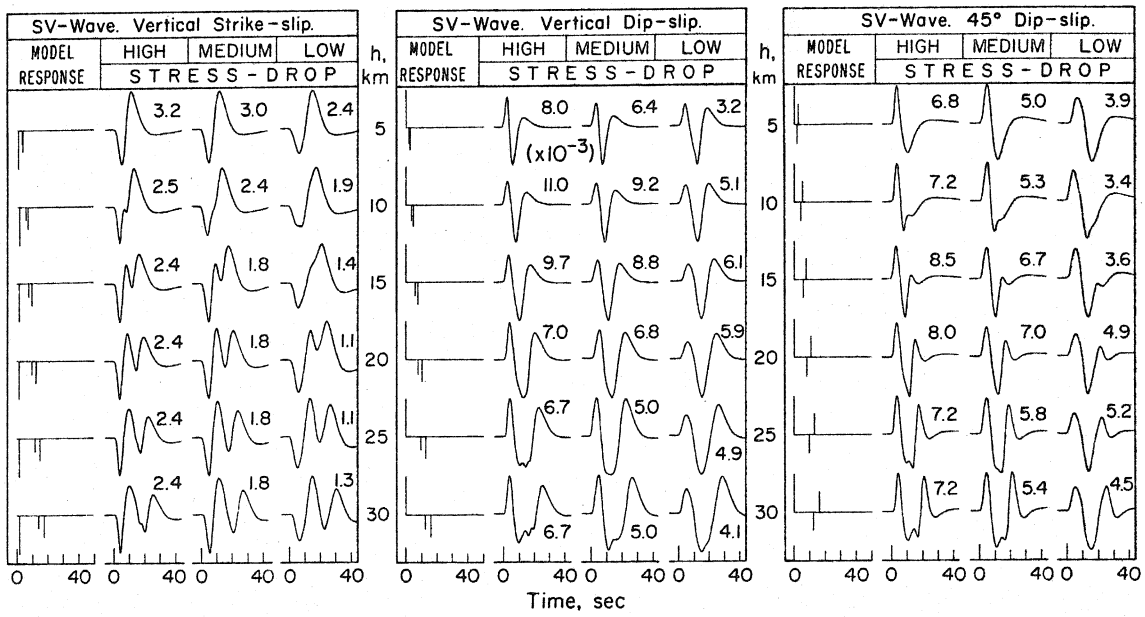

Figure 1.5. SV-wave synthetic seismograms. Same scheme as Figure 1.4.

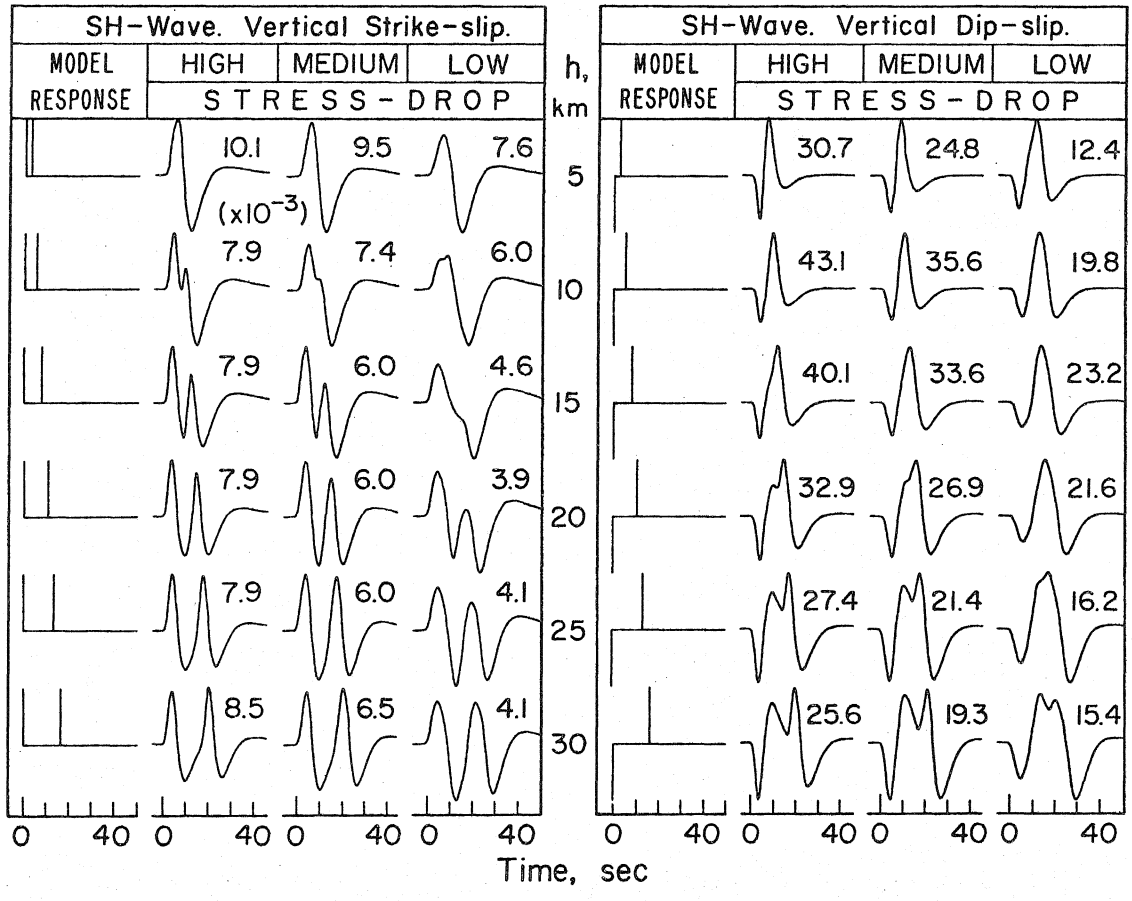

Figure 1.6. SH-wave synthetic seismograms. Same scheme as Figure 1.4.

Table 1.2

Source time function parameters

	High Stress-drop	Medium Stress-drop	Low Stress-drop
δt_1	0.5	1.0	2.0
δt_2	1.5	3.0	6.0
δt_3	0.5	1.0	2.0

Even a cursory examination of Figs. 1.4 and 1.5 shows that the phases pP, sP and sS are often as large, if not larger, an effect as the direct wave. Compare, for contrast, Fig. 1.7, which displays what the waveform would look like without the surface interactions.

The amplitudes indicated by each synthetic of Figs. 1.4, 1.5 and 1.6 do not contain the factors of $M_o/4\pi\rho$, 1/R, the appropriate receiver function, or an instrument magnification. To get the amplitude, one just multiplies in the appropriate constants and also a conversion constant, 10^{-20}, for units of centimeters, or 10^{-16}, for microns.

Note that the polarity of sP in the dip-slip case of Fig. 1.5 is different from that of Helmberger (1974) due to a sign error in the SV potential as mentioned earlier.

Fig. 1.8 shows a sample calculation for summing the three orthogonal faults. These synthetics are appropriate for a station at 80° distance and 30° azimuth from a northward striking fault plane of Fig. 1.1. The amplitudes are scaled with a fault moment of $M_o = 10^{25}$ dyne-cm, taking all the factors discussed above into account.

Two important observations can be made from this figure. The first, and obvious one, is that the waveforms are complicated due to the surface interactions. They do not look like Fig. 1.7. The second is that, due to the increased relative travel time between S and sS as opposed to P and pP and also the increased T/Q for

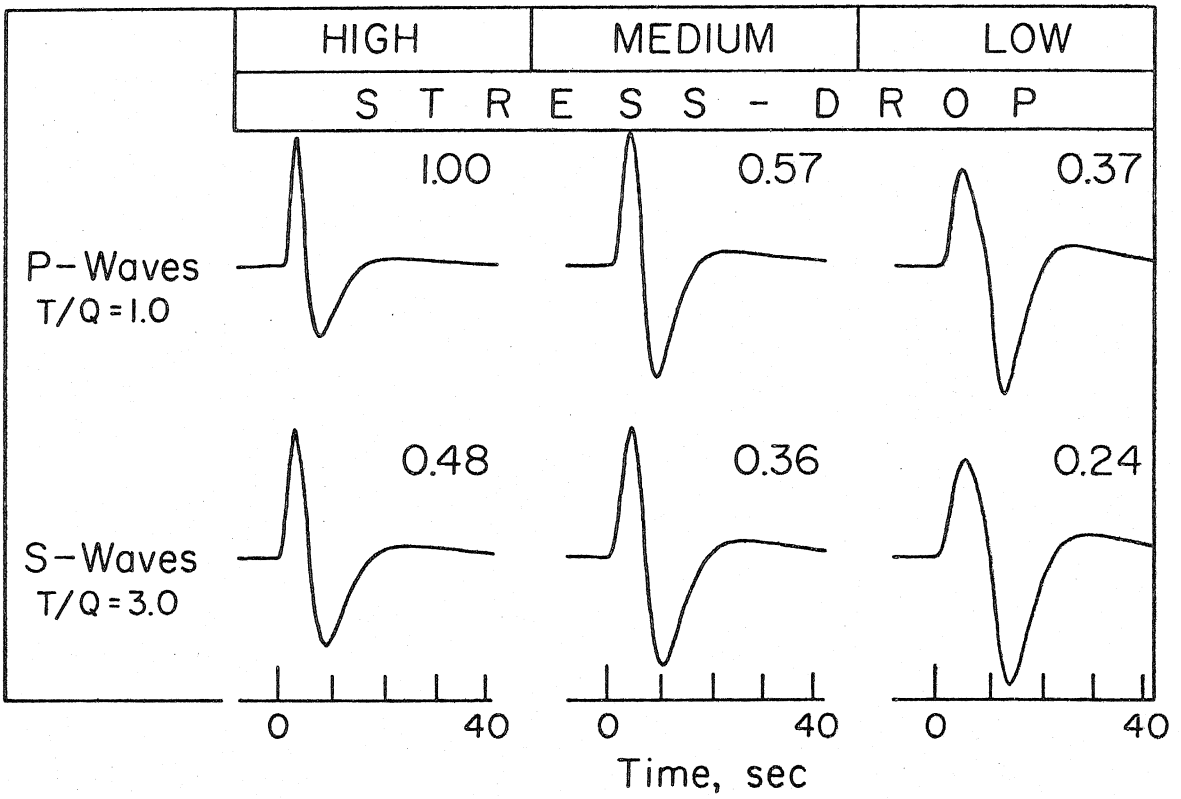

Figure 1.7. Synthetics of the time function indicated convolved with the 15-100 instrument with no crustal interactions. Amplitudes scaled to the high stress-drop P-wave.

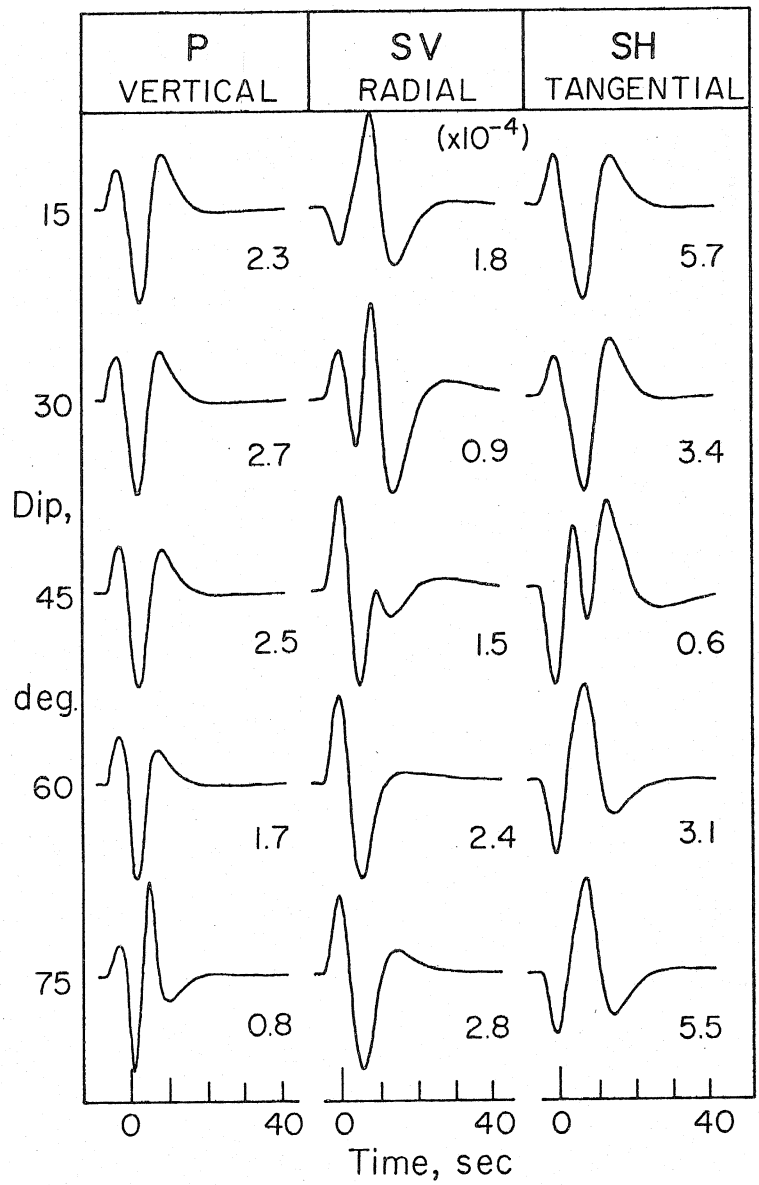

Figure 1.8. Synthetics of P, SV and SH waves from a 15 km deep medium stress-drop dislocation with a moment of 10^{25} dyne-dm seen at 80° distance, for various fault plane dips. The rake angle for all dips is 90° representing a thrust fault. Amplitudes are in cm. Positive P starts as a compression, positive SV is motion away from the source, and positive SH is clockwise motion looking from above.

S-waves, the S-waves appear to be longer period than the P-waves. A number of recent investigators have suggested the S-waves have a corner frequency at longer periods than that of the P-waves. Here is a simple mechanism of producing such an effect with a simple shear dislocation without recourse to more complicated source mechanisms.

Discussion of Ray Results

The use of the potentials and methods presented here provides a useful tool for modelling shallow earthquakes. By separating the reflected phases from the direct arrivals, one can gain a clearer picture of the source mechanism and, hopefully, a better appreciation of the processes that produce earthquakes.

An interesting feature of this method of waveform analysis is that for earthquakes with relatively simple time functions the information contained in a seismogram increases dramatically for use in focal mechanisms. Each of the phases pP, sP, sS and pS contain just as much information about the source as do the direct waves. By recognizing these phases, the seismogram can be put to much better use than has been previously possible. For example, it is theoretically possible, in many cases of fault-plane orientations, to find a well-constrained fault plane solution using very few stations by modelling the P and S waveforms and relative amplitudes.

This approach of seismic modelling using point sources will also be very useful in the near-field. Using generalized ray theory, layered earth structure can be incorporated into fault models composed of

arrays of point sources. This will allow realistic earthquake strong-motion calculations.

Propagator matrix formulation

The notation and methods of formulation for finding the far field body wave radiation from an arbitrarily oriented point dislocation is taken directly from Harkrider (1964) and Fuchs (1966). In the following, the same wave potentials (equations (1.1)) and the same coordinate system (Figure 1.1) are assumed. A full treatment of this problem will not be presented here since the above authors cover the subject quite well. It will be sufficient to state the basic concepts and to proceed directly to the solution.

The Thomson-Haskell method (Haskell, 1953) of treating wave solutions in multilayered elastic media consists basically of superposition of plane waves in the Fourier domain. Boundary conditions at each layer interface are matched by the usual way of indeterminant coefficients. The form of the wave solution is propagated across each layer by use of a four-vector and a matrix multiplication. The components of this four-vector are dependent on the 'z' coordinate only and are functions of the displacement and stress in the medium. A point source is treated by imposing jump conditions on this four-vector at the source position. These jump conditions also depend on 'z' only and can be derived from the appropriate source potentials.

The body wave problem falls naturally into two parts. Before considering the details of the solution imposed by the jump conditions at the source let us first obtain the simple potential forms for the far-field radiation in the halfspace below its layered top. The geometry is that of Figure 1.9. There are 1 to n-1 layers overlying the half-space (layer n). The source is situated in the S^{th} layer at a depth D. The indices S_1 and S_2 relate to those portions of the source layer above and below the source, respectively. The form of the potential in the halfspace will be, in general,

$$\bar{\theta}(r,z) = \int_0^{+\infty} F(k)\, e^{-ikr_v\bar{z}}\, J_\ell(kr)\,dk \qquad (1.25)$$

where, $\bar{z} = z - z_{n-1}$

$r_v = v_v/ik$

$F(k)$ = function of k which will depend on the original source potentials.

Following the details outlined by Fuchs (1966) this kind of integral can be approximated by saddle point methods to find the optic ray solution. The P and SV potentials, therefore, have the simple form, in the frequency domain,

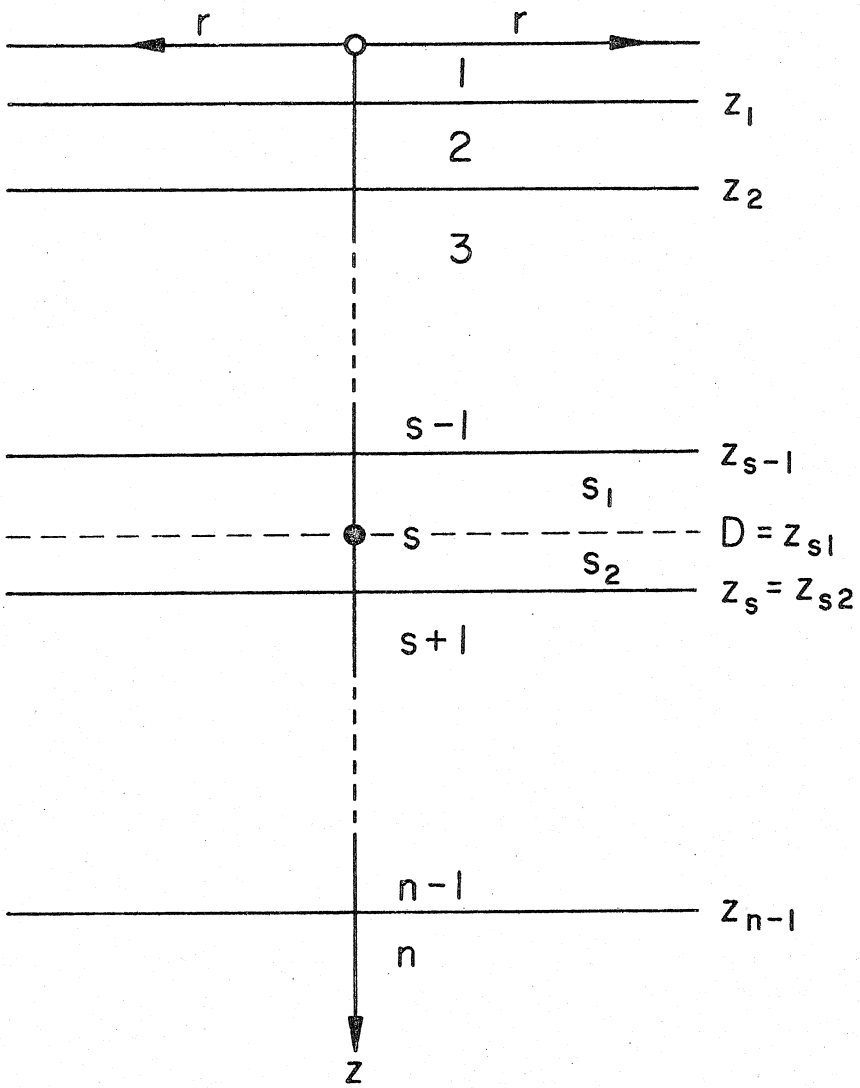

Figure 1.9. Layer geometry for matrix formulation, after Harkrider (1964).

$$\phi_n(z) = - i \left(\frac{\alpha_n}{\omega}\right)^2 \tilde{\Delta} r_{\alpha_n} e^{i \frac{\ell\pi}{2}} \frac{e^{-ik_{\alpha_n} R}}{R} \tag{1.26}$$

$$\psi_n(z) = - i \frac{\gamma_n}{k^3} \tilde{\omega} r_{\beta_n} e^{i \frac{\ell\pi}{2}} \frac{e^{-ik_{\beta_n} R}}{R}$$

where

$\tilde{\Delta}, \tilde{\omega}$ = P and SV amplitude coefficients

ℓ = Bessel function order

$\gamma_n = 2\left(\frac{\beta_n}{c}\right)^2$

c = phase velocity considered

The coefficients $\tilde{\Delta}$ and $\tilde{\omega}$ are found from the following system of equations given in Harkrider (1964):

$$\begin{bmatrix} \tilde{\Delta} \\ \tilde{\Delta} \\ \tilde{\omega} \\ \tilde{\omega} \end{bmatrix} = J \cdot \left\{ \begin{bmatrix} \frac{\dot{u}_R(0)}{c} \\ \frac{\dot{\omega}_R(0)}{c} \\ 0 \\ 0 \end{bmatrix} + A^{-1}_{R_{s1}} \begin{bmatrix} \delta\left(\frac{\dot{u}_{R_s}}{c}\right) \\ \delta\left(\frac{\dot{\omega}_{R_s}}{c}\right) \\ \delta\sigma_{R_s} \\ \delta\tau_{R_s} \end{bmatrix} \right\} \tag{1.27}$$

where,

$$J = E_{R_n}^{-1} \, a_{R_{n-1}} \, a_{R_{n-2}} \cdots a_{R_2} \, a_{R_1}$$

$$A_{R_{s1}} = a_{R_{s1}} \, a_{R_{s-1}} \cdots a_{R_2} \, a_{R_1}$$

$$\left(A_{R_{s1}}^{-1} \right)_{jk} = (-1)^{j+k} \left(A_{R_s} \right)_{\ell p}$$

$$\ell = 5 - k$$

$$p = 5 - j$$

$$E_{R_m}^{-1} = \begin{bmatrix} -2\left(\frac{\beta_m}{\alpha_m}\right)^2 & 0 & \left(\rho_m \alpha_m^2\right)^{-1} & 0 \\ 0 & \frac{c^2(\gamma_m - 1)}{\left(\alpha_m^2 \, r_{\alpha_m}\right)} & 0 & \left(\rho_m \alpha_m^2 \, r_{\alpha_m}\right)^{-1} \\ \frac{\gamma_m - 1}{\gamma_m \, r_{\beta_m}} & 0 & \left(-\rho_m c^2 \gamma_m r_{\beta_m}\right)^{-1} & 0 \\ 0 & 1 & 0 & \left(\rho_m c^2 \gamma_m\right)^{-1} \end{bmatrix}$$

and

$$(a_{R_m})_{11} = (a_{R_m})_{44} = \gamma_m \cos P_m - (\gamma_m - 1) \cos Q_m$$

$$(a_{R_m})_{12} = (a_{R_m})_{34} = i \left[(\gamma_m - 1) \frac{\sin P_m}{r_{\alpha_m}} - \gamma_m r_{\beta_m} \sin Q_m \right]$$

$$(a_{R_m})_{13} = (a_{R_m})_{24} = - (\rho_m c^2)^{-1} \left[\cos P_m - \cos Q_m \right]$$

$$(a_{R_m})_{14} = i(\rho_m c^2)^{-1} \left[\frac{\sin P_m}{r_{\alpha_m}} + r_{\beta_m} \sin Q_m \right]$$

$$(a_{R_m})_{21} = (a_{R_m})_{43} = - i \left[\gamma_m r_{\alpha_m} \sin P_m + (\gamma_m - 1) \frac{\sin Q_m}{r_{\beta_m}} \right]$$

$$(a_{R_m})_{22} = (a_{R_m})_{33} = - (\gamma_m - 1) \cos P_m + \gamma_m \cos Q_m$$

$$(a_{R_m})_{23} = i(\rho_m c^2)^{-1} \left[r_{\alpha_m} \sin P_m + \frac{\sin Q_m}{r_{\beta_m}} \right]$$

$$(a_{R_m})_{31} = (a_{R_m})_{42} = \rho_m c^2 \gamma_m (\gamma_m - 1) \left[\cos P_m - \cos Q_m \right]$$

$$(a_{R_m})_{32} = i\rho_m c^2 \left[(\gamma_m - 1)^2 \frac{\sin P_m}{r_{\alpha_m}} + \gamma_m^2 r_{\beta_m} \sin Q_m \right]$$

$$(a_{R_m})_{41} = i\rho_m c^2 \left[\gamma_m^2 r_{\alpha_m} \sin P_m + (\gamma_m - 1)^2 \frac{\sin Q_m}{r_{\beta_m}} \right]$$

$$P_m = k r_{\alpha_m} (z_m - z_{m-1})$$

$$Q_m = k r_{\beta_m}$$

The first four-vector on the right side of equation (1.27) represents the free surface boundary condition. The other vector with the '$\delta(\ )$' quantities describe the jump conditions at the source. These are given by

$$\delta\left(\frac{\dot{u}_{R_s}}{c}\right) = k^2 \left[\left(S_{01}^{+} - S_{01}^{-}\right) - ik\, r_{\beta_s}\left(S_{02}^{+} + S_{02}^{-}\right)\right]$$

$$\delta\left(\frac{\dot{\omega}_{R_s}}{c}\right) = ik\left[-ik\, r_{\alpha_s}\left(S_{01}^{+} + S_{01}^{-}\right) + k^2\left(S_{02}^{+} - S_{02}^{-}\right)\right] \tag{1.28}$$

$$\delta\sigma_{R_s} = k^2 c^2 \rho_s \left[\left(\gamma_s - 1\right)\left(S_{01}^{+} - S_{01}^{-}\right) - ik\, r_{\beta_s}\gamma_s\left(S_{02}^{+} + S_{02}^{-}\right)\right]$$

$$\delta\tau_{R_s} = k^2 c^2 \rho_s \left[-\gamma_s r_{\alpha_s}\left(S_{01}^{+} + S_{01}^{-}\right) - ik(\gamma_s - 1)\left(S_{02}^{+} - S_{02}^{-}\right)\right]$$

where

$$\phi_{S_0}(z) = S_{01}^{\pm}\, e^{-ikr_{\alpha_s}|z-D|} \qquad \pm \text{ as } z \gtrless D \tag{1.29}$$

$$\psi_{S_0}(z) = S_{02}^{\pm}\, e^{-ikr_{\beta_s}|z-D|}$$

and

$$\phi_{S_o}(r,\theta,z,k) = \int_0^\infty \phi_{S_o}(z)\, J_\ell(kr) \cos \ell\theta \, dk$$

$$\Psi_{S_o}(r,\theta,z,k) = \int_0^\infty \Psi_{S_o}(z)\, J_\ell(kr) \cos \ell\theta \, dk \qquad (1.30)$$

The values for $S_{01}^{\pm}$ and $S_{02}^{\pm}$ can be found by inspection of equations (1.1)

vertical strike-slip

$$S_{01}^{+} = S_{01}^{-} = + \frac{K\, k^2 i}{r_\alpha} \qquad (1.31)$$

$$S_{02}^{+} = - S_{02}^{-} = - K\, k$$

vertical dip-slip

$$S_{01}^{+} = - S_{01}^{-} = K\, 2k^2 \qquad (1.32)$$

$$S_{02}^{+} = - S_{02}^{-} = i\, K \frac{(k_\beta^2 - 2k^2)}{k r_\beta}$$

45° dip-slip

$$S_{01}^{+} = S_{01}^{-} = - i\, K \frac{(2k_\alpha^2 - 3k^2)}{r_\alpha} \qquad (1.33)$$

$$S_{02}^{+} = - S_{02}^{-} = - K\, 3k$$

Substituting these values into equations (1.28) gives

vertical strike-slip

$$\begin{aligned}
\delta\left(\frac{\dot{u}_{R_s}}{c}\right) &= 0 \\
\delta\left(\frac{\dot{\omega}_{R_s}}{c}\right) &= 0 \\
\delta\sigma_{R_s} &= 0 \\
\delta\tau_{R_s} &= -2k^4c^2\rho_s\, i
\end{aligned} \tag{1.34}$$

vertical dip-slip

$$\begin{aligned}
\delta\left(\frac{\dot{u}_{R_s}}{c}\right) &= 2k_\beta^2 k^2 \\
\delta\left(\frac{\dot{\omega}_{R_s}}{c}\right) &= 0 \\
\delta\sigma_{R_s} &= 2k^2c^2\rho_s\left[\gamma_s k_\beta^2 - 2k^2\right] \\
\delta\tau_{R_s} &= 0
\end{aligned} \tag{1.35}$$

45° dip-slip

$$\delta\left(\frac{\dot{u}_{R_s}}{c}\right) = 0$$

$$\delta\left(\frac{\dot{\omega}_{R_s}}{c}\right) = -4\, k^2 k_\alpha^2\, i \qquad (1.36)$$

$$\delta\sigma_R = 0$$

$$\delta\tau_R = i\, 2k^2 c^2 \rho \left[2\gamma_s k_\alpha^2 - 3k^2 \right]$$

Going back to equation (1.27) we can easily solve this system of four equations and four unknowns by Cramer's rule:

P waves $$\tilde{\Delta} = \frac{D_1}{D} \qquad (1.37)$$

SV waves $$\tilde{\omega} = \frac{D_1}{D}$$

where

$$D = (J_{32} - J_{42})\,(J_{21} - J_{11}) + (J_{41} - J_{31})\,(J_{22} - J_{12})$$

$$D_1 = (H)_{11} \left\{ J_{22}(J_{41} - J_{31}) + J_{21}(J_{32} - J_{42}) \right\}$$

$$+ (H)_{21} \left\{ J_{11}(J_{42} - J_{32}) + J_{12}(J_{31} - J_{41}) \right\}$$

$$+ (H)_{31} \left\{ J_{11}J_{22} - J_{21}\,J_{12} \right\}$$

$$+ (H)_{41} \left\{ J_{21}J_{12} - J_{11}J_{22} \right\}$$

$$D_2 = (H)_{11}\left\{J_{41}J_{32} - J_{31}J_{42}\right\}$$
$$+ (H)_{21}\left\{J_{31}J_{42} - J_{41}J_{32}\right\}$$
$$+ (H)_{31}\left\{J_{41}(J_{22} - J_{12}) + J_{42}(J_{11} - J_{21})\right\}$$
$$+ (H)_{41}\left\{J_{32}(J_{21} - J_{11}) + J_{31}(J_{12} - J_{22})\right\}$$

$$H = J\, A^{-1}_{R_{sl}} \begin{bmatrix} \delta\left(\frac{\dot{u}_{R_s}}{c}\right) \\ \delta\left(\frac{\dot{\omega}_{R_s}}{c}\right) \\ \delta\sigma_{R_s} \\ \delta\tau_{R_s} \end{bmatrix}$$

By substituting the equations (1.28)into this solution for each potential term we can form the total solution for the far field body wave radiation in the halfspace for any dislocation orientation:

$$\overline{W} = i\frac{M_o}{4\pi\rho_s}\frac{r^2_{\alpha n}\alpha^2_n}{\omega^4}\left\{-\overline{\Delta}_1\cdot A_1 + i\overline{\Delta}_2\cdot A_2 + \overline{\Delta}_3\cdot A_3\right\}\cdot\frac{e^{-ik_{\alpha n}R}}{R}$$

$$\overline{Q} = i\,\frac{M_o}{4\pi\rho_s}\frac{r^2_{\beta n}c^2}{\omega^4}\left\{-\overline{\omega}_1\cdot A_1 + i\overline{\omega}_2 A_2 + \overline{\omega}_3 A_3\right\}\frac{e^{-ik_{\beta n}R}}{R} \qquad (1.38)$$

where $\overline{\Delta}_i$ and $\overline{\omega}_i$, i = 1,2,3, stand for the coefficients of the vertical strike-slip, vertical dip-slip, and 45° dip-slip terms, respectively. Note also that

$$\begin{aligned} \tilde{\Delta}_i &= \overline{\Delta}_i K \\ \tilde{\omega}_i &= \overline{\omega}_i K \end{aligned} \tag{1.39}$$

The SH potential can be treated in a very analogous manner. Similar to equation (1.27) is Harkrider's equation (122):

$$\begin{bmatrix} \tilde{\varepsilon} \\ \\ \tilde{\varepsilon} \end{bmatrix} = E_{L_n}^{-1} A_L \begin{bmatrix} V \\ \\ T \end{bmatrix} \tag{1.40}$$

where,

$$V = - \frac{\left[(J_L)_{12} - (J_L)_{22} \right]}{\left[(J_L)_{11} - (J_L)_{21} \right]} T$$

$$V = \frac{\dot{v}_{L_o}}{c} + (A_{L_{s1}})_{22} \, \delta \left(\frac{\dot{v}_{L_s}}{c} \right) - (A_{L_{s1}})_{12} \, \delta\tau_{L_s}$$

$$T = - (A_{L_{s1}})_{21} \, \delta \left(\frac{\dot{v}_{L_s}}{c} \right) + (A_{L_{s1}})_{11} \, \delta\tau_{L_s}$$

$$A_L = a_{L_{n-1}} \; a_{L_{n-2}} \cdots a_{L_2} \; a_{L_1}$$

a_{Lm} = Haskell matrix for the mth layer

$$(a_{L_m})_{11} = (a_{L_m})_{22} = \cos(Q_m)$$

$$(a_{L_m})_{12} = \frac{i}{\rho_m \beta_m^2 r_{\beta_m}} \sin(Q_m)$$

$$(a_{L_m})_{21} = i\rho_m \beta_m^2 r_{\beta_m} \sin(Q_m)$$

$$J = E_{L_n}^{-1} A_L = \begin{bmatrix} (ik)^{-1} & 0 \\ 0 & -(ik\rho_n \beta_n^2 r_{\beta_m})^{-1} \end{bmatrix} A_L$$

and

$$\delta\left(\frac{\dot{v}_L}{\frac{s}{c}}\right) = ik^2 (S_{03}^+ - S_{03}^-) \tag{1.41}$$

$$\delta\tau_s = - ik^2 \rho_s \beta_s^2 r_{\beta_s} (S_{03}^+ + S_{03}^-)$$

The values for $S_{03}^{\pm}$ can again be found by inspection of the SH potentials in equation (1.1) as vertical strike-slip

$$S_{03}^+ = S_{03}^- = - \frac{i\, Kk_\beta^2}{r_\beta} \tag{1.42}$$

vertical dip-slip

$$S_{03}^+ = - S_{03}^- = - Kk_\beta^2 \tag{1.43}$$

Since the value for $\tilde{\varepsilon}$ can be found explicitly using equation (1.40) the total far-field tangential SH displacement is given by

$$\bar{V} = - i \frac{M_o}{4\pi\rho_s} \frac{r_{\beta_n}}{\omega^2} \left[\bar{\varepsilon}_1 \cdot A_4 \, i - \bar{\varepsilon}_2 \cdot A_5 \right] \frac{e^{-ik_{\beta_n} R}}{R} \qquad (1.44)$$

where the same conventions apply here as in the P-SV case.

A calculation comparing the two methods, ray and matrix, was carried out for an arbitrary source situated in a layer over a half-space for the P wave response. One hundred rays were summed for the ray calculation and the two responses were compared. Both seismograms were identical to the last detail indicating that all the different analysis techniques involved in formulating each method are compatible and, on the basis of their assumptions, correct.

Discussion of the matrix results

The Thomson-Haskell formulation can be a very useful tool when complicated structures are considered. In particular, gradients can be modelled by considering a series of thin layers. The ray summation technique would become unwieldy in many of these cases. However, the ray method has many more natural advantages over matrix methods, one of the major ones being the ease at which isolated phases can be studied. Once a portion of an earth model is pinpointed

by identifying a particular phase it can be studied with much more confidence and resolvability. Another important advantage by using rays is the ease and compactness the source inversion problem can be formulated and implemented. The partial derivatives become easier to manipulate and construct. This will be a topic of the next section.

Inversion Theory for Body waves

The inversion formulation used here will be taken mostly after Wiggins (1972) and will incorporate some important techniques discussed by Mellman, Burdick and Helmberger (1975). The problem of finding a better model given a set of data and some starting model reduces to the following matrix equation

$$A' \Delta P' = \Delta C' \tag{1.45}$$

where

$$A' = \begin{bmatrix} \frac{\partial C_1}{\partial P_1} & \frac{\partial C_1}{\partial P_2} & \cdots & \frac{\partial C_1}{\partial P_n} \\ \vdots & \cdots & \frac{\partial C_j}{\partial P_i} & \vdots \\ \frac{\partial C_m}{\partial P_1} & \cdots & & \frac{\partial C_m}{\partial P_n} \end{bmatrix}$$

$$\Delta P' = \begin{bmatrix} \Delta P_1 \\ \vdots \\ \Delta P_n \end{bmatrix}, \quad \Delta C' = \begin{bmatrix} O_1 - C_1 \\ \vdots \\ O_m - C_m \end{bmatrix}$$

and

O_j observations (seismograms) $j = 1,\ldots,m$

C_j calculated models (synthetics) $j = 1,\ldots m$

$C_j = F(P_i)$ $j = 1,\ldots,m$

$F(P_i)$ is a functional of the n parameters P_i

A' contains the derivatives of the model with respect to the parameters

$\Delta P'$ contains the parameter changes

$\Delta C'$ contains the difference, in some sense, between the observations and the calculated.

The inversion problem is then to solve equation (1.45) for $\Delta P'$ given A' and $\Delta C'$.

To express the difference between the observations and calculated models, $O_j - C_j$, a transformation will be made on the data and synthetic seismograms which will minimize and eliminate some undesirable effects on the inversion. After Mellman, Burdick and Helmberger (1975), define a correlation function, ϕ, by the following:

$$\phi(f(t),\ g(t,P_i)) = \frac{\max\limits_{-\infty<\tau<\infty} \int_{-\infty}^{+\infty} f(t)\ g\ (t+\tau,\ P_i)\ dt}{\left[\int_{-\infty}^{+\infty} f^2(t)\ dt \quad \int_{-\infty}^{+\infty} g^2(t,P_i)\ dt\right]^{1/2}} \qquad (1.46)$$

where,

$f(t)$ = observed time series

$g(t,P_i)$ = synthetic seismogram

This correlation function has several nice advantages. The first is that it circumvents inverting to every time point on the seismogram which would make the problem very nonlinear away from the optimal model. The function has the additional properties that it is totally insensitive to absolute travel time and absolute amplitude. It compares shapes only. It is very sensitive to relative amplitudes and relative times within the time series, however. In effect, it reduces the comparison of two time series into one number. The elements of the $\Delta C'$ vector then become:

$$O_j - C_j = 1 - \phi(O_j, C_j) \tag{1.47}$$

The elements of the derivative matrix, A', are now defined in terms of the correlation function, that is,

$$\frac{\partial C_j}{\partial P_i} = \frac{\partial \phi(O_j, C_j)}{\partial P_i} \tag{1.48}$$

The partial derivatives can be calculated numerically but this requires that at least two different models have to be calculated for every derivative. In practice, model calculations are the most time consuming operation so it is desirable to find derivatives some other way. In this section we will pursue the approach of using

analytical expressions for the derivatives. Consider equation (1.49).

$$\phi = \phi(\tau, P_i) \tag{1.49}$$

where, τ = relative time lag.

Therefore, by the chain rule,

$$\frac{\partial \phi(\tau, P_i)}{\partial P_i} = \left(\frac{\partial \phi}{\partial P_i}\right)_\tau + \left(\frac{\partial \phi}{\partial \tau}\right)_{P_i} \frac{\partial \tau}{\partial P_i} \tag{1.50}$$

We choose to evaluate this expression near $\tau = \tau_0$, the relative lag at maximum correlation, so we obtain

$$\lim_{\tau \to \tau_o} \left\{ \frac{\partial \phi}{\partial P_i} (\tau, P_i) \right\} = \left(\frac{\partial \phi}{\partial P_i}\right)_{\tau_o} + \lim_{\tau \to \tau_o} \left\{ \left(\frac{\partial \phi}{\partial \tau}\right)_{P_i} \frac{\partial \tau}{\partial P_i} \right\} \tag{1.51}$$

The second term on the right vanishes since the change in ϕ with respect to the lag, τ, at the peak of the correlation is zero. Therefore,

$$\frac{\partial \phi}{\partial P_i} (\tau_o, P_i) = \left(\frac{\partial \phi}{\partial P_i}\right)_{\tau_o} \tag{1.52}$$

Substituting equation (1.46) into (1.52), we obtain

$$\left(\frac{\partial \phi}{\partial P_i}\right)_{\tau_o} = -\left[\int_{-\infty}^{+\infty} g^2 dt\right]^{-1} \cdot \left[\int_{-\infty}^{+\infty} g\left(\frac{\partial g}{\partial P_i}\right) dt\right] \cdot \phi + \left[\int_{-\infty}^{+\infty} g^2 dt \int_{-\infty}^{+\infty} f^2 dt\right]^{-1/2} \cdot \left[\int_{-\infty}^{+\infty} f\left(\frac{\partial g}{\partial P_i}\right) dt\right] \tag{1.53}$$

The expressions for the derivatives of g are all straightforward and can be simply found by differentiating the following general equation for a seismogram (with summation convention)

$$g(t) = B_j S_j\left(t - \tau_{L_j}\right) * \left\{\alpha_{ij}\, \delta\left(t - \tau_{S_{ij}}\right)\right\} * I(t) * Q(t) \tag{1.54}$$

where,

j = index of the j^{th} point dislocation

i = index of the i^{th} ray

B_j = relative amplitude of the j^{th} source

$S_j(t-\tau_{L_j})$ = parameterized time function of the j^{th} source

τ_{L_j} = relative time lag of the j^{th} source

α_{ij} = amplitude of i^{th} ray, j^{th} source

$\tau_{s_{ij}}$ = relative travel time of i^{th} ray, j^{th} source

$\delta(\tau-\tau_{s_{ij}})$ = lagged Dirac delta function

Thus, a factor of two in speed on the computer is obtained since equation (1.53) requires only one model calculation. This savings is significant with large data sets. Storage requirements, however, are substantially increased because of all the derivatives of g needed, each of which are time series. Appendix II contains the explicit forms of these derivatives for the parameterization used in the source modelling.

The introduction of a parameter weighting matrix, W, is needed to nondimensionalize the problem. W will be diagonal and W_{ii} proportional to the dimension of the i^{th} parameter. Table 1.3 shows the values of W_{ii} used in these inversions. These were determined by examining obvious relations between the variables and trial-and-error on synthetic problems.

In addition to W, a matrix S is defined which represents the error in the observations. The elements of S will be equal to $Cov(O_i O_j)$. It will be assumed that the errors in the observations are uncorrelated so that S is diagonal and that S_{ii} is equal to σ_i^2, the variance of the i^{th} datum. Transforming the problem into these new coordinates we obtain the matrix equation

$$A\,\Delta P = \Delta C \qquad (1.55)$$

TABLE 1.3

	Times (sec) (δt's, τ_{L_j})	Distance (km) (x, y, z)	Angles (RAD) (δ, θ, λ)	Amplitudes (B_j's)
W_{ii}	1.0	5.0	.05	.05

where,

$$A = S^{-1/2} A' W^{+1/2}$$

$$\Delta P = W^{-1/2} \Delta P'$$

$$\Delta C = S^{-1/2} \Delta C'$$

Using the eigenvector-eigenvalue decomposition (Lanczos, 1961), A is transformed to

$$A = U \Lambda V^T \tag{1.56}$$

where, U contains k eigenvectors associated with the columns of A, V contains k eigenvectors associated with the rows of A, and Λ is the eigenvalue matrix of A. The rank of A is k. The particular solution of (1.55) is then

$$\Delta P = V \Lambda^{-1} U^T \Delta C \tag{1.57}$$

The determination of k is achieved through the "cut-off" method described by Wiggins (1972). The problem is to find a trade-off between the two "errors" in the inverse problem. That is, the generalized inverse should minimize both

$$\det (\varepsilon'^T S^{-1} \varepsilon')^2 \tag{1.58}$$

and

$$\det (\Delta P'^T W^{-1} \Delta P')^2 \tag{1.59}$$

where,

$$\varepsilon' = A'\Delta P' - \Delta C'$$

Equation (1.58) represents the least-squares error for the solution and (1.59) says model perturbations must be small and close to the starting model. This is accomplished by introducing a somewhat arbitrary eigenvalue cut-off level through the equation

$$\sigma^2_{p_i'} = \sigma^2 \sum_{j=1}^{m} \frac{V_{ij}^2}{\lambda^2_j} \tag{1.60}$$

where

$\sigma^2_{p_i'}$ = variance of the ith parameter change.

λ_j = jth eigenvalue.

The largest m is used such that

$$\sigma^2_{p_i'} \leq M \tag{1.61}$$

where M is the cut-off parameter determined empirically for the problem at hand. It effectively limits the size of the parameter changes by excluding those regions in the model space which are represented by very small eigenvalues. In the inversion presented in the next chapter the cut-off parameter proved to be unnecessary so that the generalized inverse reduced to the usual least-squares inverse.

By the very nature of the problem seismic noise introduces peculiar nonlinearities near the minimums in the model space (Mellman, Burdick and Helmberger, 1975). To counteract these effects a step-size parameter is introduced to further convergence. Instead of reparameterizing using $\Delta P'$, $\gamma.\Delta P'$ is used, where γ is the percentage step-size. In practice, after each iteration, several models are calculated using a certain percentage of the step-size determined by equation (1.57) in the direction of the vector ΔP. A measure of error,

$$\varepsilon_1 = \left\{ \sum_{j=1}^{m} \frac{\Delta C_j^2}{\sigma_j^2} \right\}^{1/2} \tag{1.62}$$

is used to determine the goodness of fit. After four points on the $\varepsilon_1 - \gamma$ plane have been determined, up to the full step, a cubic polynomial is fit through the points using the Lagrange interpolation formula and then analytically differentiated to find the minimum. This value is then used as the step size.

To demonstrate some of the characteristics of the inversion process consider the synthetic problem in Table 1.4. Seventeen synthetic, azimuthally distributed P waves and 5 SH waves were constructed using the 'true' model parameters. The variation between the P waveforms was small due to the particular fault geometry so that the inversion routine had to distinguish small changes in the

Table 1.4

One-Source Synthetic Problem

Parameter	True Model	Starting Model	Iteration # 1	2	3	4	5	6	
$\delta^{(0)}$	45.0	60.0	57.8	54.5	50.4	49.8	46.4	47.6	
$\lambda^{(0)}$	70.0	90.0	81.4	80.2	72.8	66.5	67.4	71.6	
$\theta^{(0)}$	-70.0	-90.0	-82.5	-86.5	-84.8	-80.8	-75.6	-71.6	
HS (km)	14.0	20.0	16.6	14.7	14.2	14.4	14.2	14.3	
δt_1 (sec)	.001	0.50	0.28	0.32	0.28	0.24	0.27	0.21	
δt_2	3.50	4.30	4.10	3.81	3.73	3.68	3.69	3.77	
δt_3	1.0	0.02	0.0	0.0	0.02	0.0	0.07	0.11	
av. fit ϕ =	1.0	.9475	.9843	.9940	.9976	.9977			17 P only
						.9964	.9979	.9968	17 P + 5 SH

shapes resulting in large changes in the parameters. Four iterations were performed using only the seventeen P waves. The average fit improved dramatically with most parameters converging to the true value. The strike was off by ten degrees for iteration four, however. This should be expected since this particular angle is notoriously unconstrained for most P wave thrust-fault solutions. Including the five SH waves improved the overall fit in the next iteration. The iterations after number five (seven and eight are not shown) started to exhibit small oscillatory changes in the parameters indicating that a local minimum had been achieved in the model space. The last time parameter, δt_3, was totally unconstrained in this test and tended to trade-off with δt_2. This might indicate that a simpler time function parameterization, say a triangle, might be just as appropriate.

The rate of convergence and how constrained any particular parameter becomes is related to the data distribution, starting model, and the parameterization. For example, anticipating the next chapter, if stations which plot on a wave node are included, some of the orientation angles could be very well constrained even with relatively low values of the correlation function, say at .96. This simple test also suggests that it would be advisable to include more types of data, e.g., P and SH, rather than a large group of similar data. This, of course, depends on the wave variation in data set.

We will now use the inverse and modelling procedures developed in this chapter to study the focal mechanism of a moderate-sized shallow earthquake.

Chapter 2

A BODY WAVE INVERSION OF THE KOYNA, INDIA, EARTHQUAKE OF 10 DECEMBER 1967 AND SOME IMPLICATIONS FOR BODY WAVE FOCAL MECHANISMS

Introduction

On December 10, 1967, a sizable earthquake, M = 6.4, occurred near the Koyna Dam and Shivajisagar Lake area of western-central India, Figure 2.1. This event is significant since it occurred in what was previously considered an aseismic part of the Indian shield. It is also unusual in that it almost certainly seems to be intimately related to the impoundment of the nearby reservoir. Many authors consider it to be the largest of the "man-made" earthquakes caused to date (Aki, 1972). Ever since the impoundment of the Koyna reservoir in 1962, seismicity steadily increased in frequency until September 13, 1967, when a magnitude 5.8 shock occurred very close to the damsite (Guha et al., 1970). Three months later the principal shock occurred and seismicity has been significant since. The Koyna earthquake was the largest earthquake ever to be felt in Peninsular India and had a radius of perceptibility of 700 km. Two hundred people were killed, several thousand injured, and two villages totally destroyed (Narain and Gupta, 1968).

Geologically,the area lies near the western margin of the Deccan

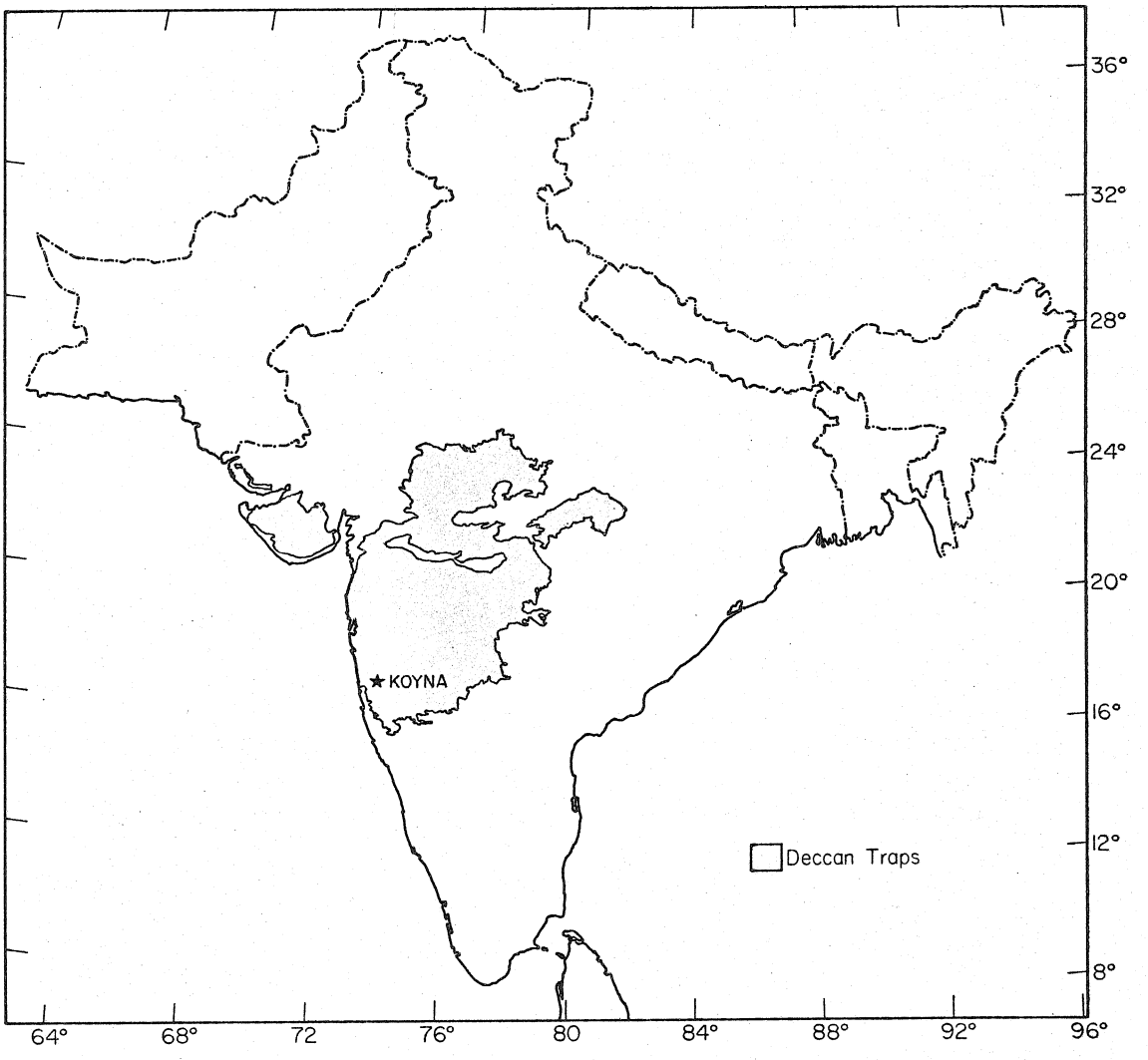

Figure 2.1 Index map of the Indian Region showing the location of the Koyna area.

trap basalts of Late Cretaceous to Paleocene age (Figure 2.1). These basalts are believed to be the thickest near their western edge, at most a few kilometers, and thin eastward. Based on earthquake body wave phase velocities and the outcrops around the basalts it appears that a granitic basement underlies the traps (Narain, 1973). From aerial photographs, drainage patterns, and field studies the trends of faults contained in the area are NNW to NNE (Snow, personal communication, 1975). Interpretations of the regional gravity field of western India indicate that the sub-trap basement is about 6-7 km deep on the coast, rises to about 1 km in the Koyna area and falls to about 3 km eastwards (Guha et al., 1973), putting the Koyna area directly over a large basement high. In general, however, the local structure of the Koyna region is very simple and it is amazing that such drastic events be centered there.

The history of study of this earthquake is as interesting and diverse as the circumstances surrounding it. For example, Figure 2.2a shows the collection of fault plane solutions done by various authors. Apparently, there seems to be some ambiguity on the orientation of the Koyna fault. Gupta et al. (1969, 1971), claim the Koyna source to be an extremely complex multiple shock with rupture propagating from south to north on a vertically dipping fault plane. This is based on interpretations made from short-period P phases in the tradition of Wyss and Brune (1967). Because the earthquake was so widely felt

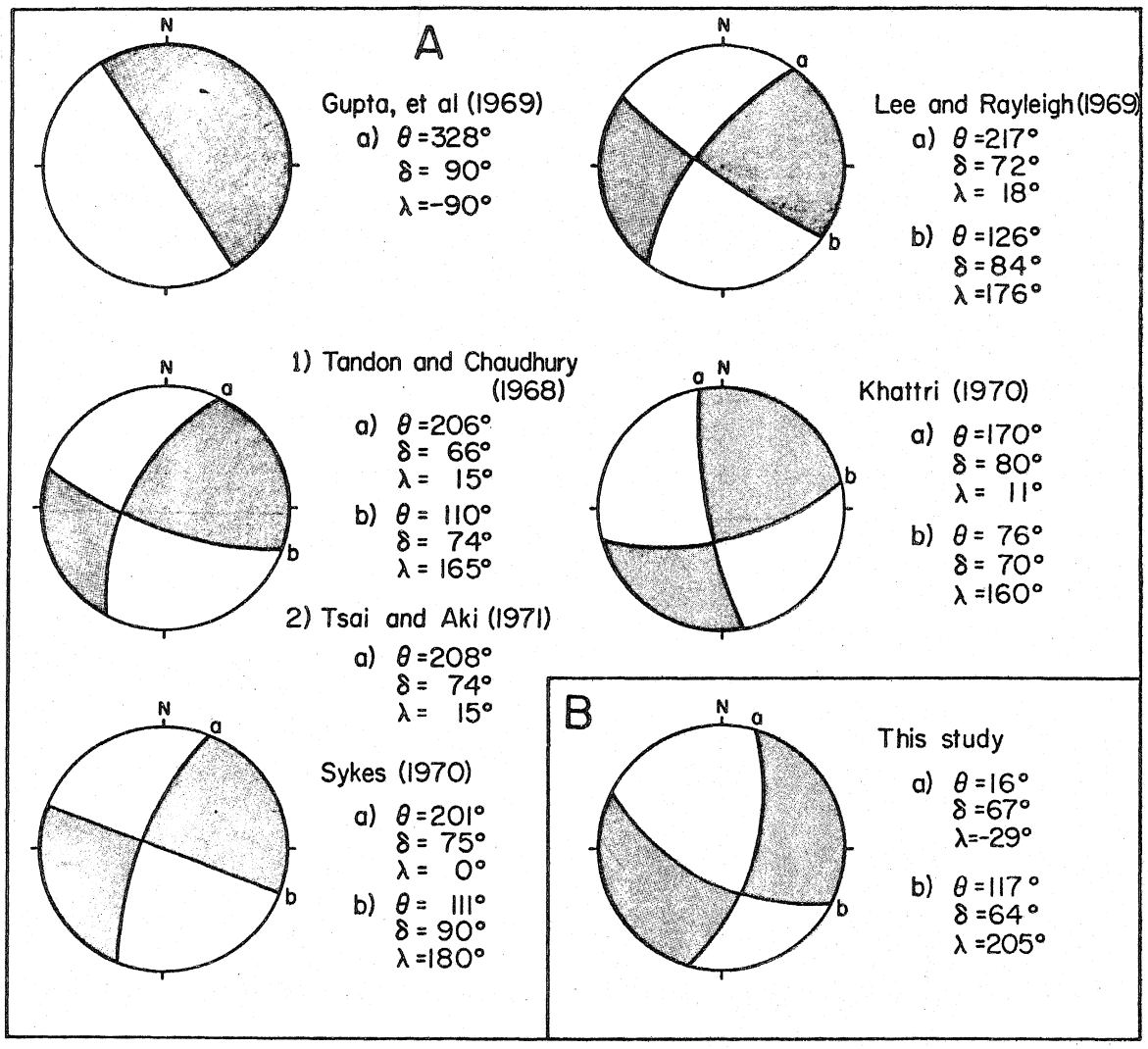

Figure 2.2. Focal mechanisms done by various authors for the Koyna earthquake.

but also caused high intensities locally, many workers support a very deep source which propagated to the surface. In particular, Gorbunova et al. (1970), from the study of P arrival times, postulate that the earthquake initiated at a depth of 80 km, propagated upwards along a steeply dipping fault plane about 25 km wide with a vertical and horizontal rupture velocity of 8 km/sec and 3 km/sec, respectively. Tsai and Aki (1971) studying surface waves from the event reach a similar conclusion obtaining a depth of about 55 km to explain the observed radiation pattern. Guha et al. (1970), however, attribute the large size of the felt area not to deep hypocentral depths but to the efficient propagation of Lg in the Indian shield due to a shallow source in the continental waveguide.

Intertwined with these interpretations are the discrepancies observed in epicentral locations. By partitioning the P wave arrival-time data set into several categories based on distance, several authors have noted trends in the computed epicenters obtained from each set. This type of calculation was the basis for the studies made by Gorbunova et al. (1970) and Gupta et al. (1971). Thus, even though there is good isoseismal evidence, the hypocentral location is very poorly known.

One of the major goals of this study will be to test these various hypotheses by examining the nature of the body wave waveform for both P and SH. We will want to determine the fault orientation, depth, and time history for the earthquake in a simultaneous inversion for these parameters.

Modelling Procedure

Independent determinations of layer parameters from travel time studies and refraction profiles are used for earth structure around the source. Assuming a simple starting model for the source based on first order epicentral locations and interpretations of the data seismograms, synthetic seismograms are computed and compared with the originals. Generally, this entails the use of only one point source in the layered medium at first. The number of rays computed for the medium depends on how much of the record is considered. For example, if thirty seconds of record is to be modelled, all rays with arrival times within this period are tested. Often, it turns out that many of the rays contribute virtually nothing to the response so these are discarded to simplify calculations. Several forward problem runs are made to improve the fits and to determine which effects, source of structure, are important in explaining various features of the seismogram. If the one-source model seems sufficient an inversion run is made. It must be emphasized that the model is initially kept as simple as possible. If the data inversion indicates that more sources or more structure are needed to explain the seismogram, then, and only then, are more complications put in and only with the highest justification. It is precisely these reasons why the point dislocation model is so well suited to this type of problem.

Data and Data Processing

Copies of all the available WWSSN long and short period recordings for the Koyna event were procured. Records for long period P and SH waves were chosen for waveform inversion on several criteria. Waveforms were used which had a signal to noise ratio of five or better and a minimum amplitude of approximately 1 cm on the enlarged record so that line thickness errors would be small. SH waves had to be naturally rotated into the ray direction with the SV component comparable or smaller than SH to eliminate PL wave problems. In addition, stations were between 30 and about 85 degrees in order to avoid upper mantle structure effects. Thirteen P waves and six SH waves were finally chosen, Table 2.1. Azimuthal coverage is good for this data set except in southeastern azimuths.

Each seismogram was digitized four times, the trace line top and bottom twice, at an irregular interval of two to three points per trace-second and interpolated at four points per trace-second. The four traces were then averaged to obtain the final digital form. A deskewing operation was also applied to the waveforms to eliminate the image skew inherent in the seismograph recording system (Mitchell and Landisman, 1969). This had negligible effect on most records but was important for some of the high amplitude SH waves.

For interpretive purposes 21 S-wave rotations into the ray direction were performed with varying degrees of success. A

TABLE 2.1

WWSSN STATIONS FOR LONG PERIOD P AND SH

(* - used in the inversion)

(√ - used, but not in the formal inversion)

STATION	$\Delta^{(0)}$	$AZ^{(0)}$	$BAZ^{(0)}$	P	SH
AAE	35.0	260.8	72.64	*	
ADE	80.6	131.0	298.7	√	*
ANP	45.0	71.6	269.8	√	
AQU	56.7	309.6	96.7	*	
ATU	48.2	305.6	100.9	√	
BAG	44.7	84.0	278.3	√	
COP	59.7	324.9	104.0	√	
CTA	80.3	114.6	292.5	*	*
DAV	51.5	94.8	286.5	√	
ESK	68.5	323.2	90.5	√	*
HKC	38.3	75.9	270.1	*	√
HNR	89.2	100.1	287.6	√	√
IST	45.0	311.1	108.0	*	*
JER	37.7	299.7	103.1	*	
KEV	59.6	342.9	126.3	√	√
KON	62.1	328.9	103.6	*	
MAT	59.5	57.5	269.7	*	√
MUN	63.8	140.2	314.0	√	
NAI	40.8	246.8	61.4	*	

TABLE 2.1 (continued)

STATION	$\Delta^{(0)}$	$AZ^{(0)}$	$BAZ^{(0)}$	P	SH
NOR	73.0	351.2	87.0	✓	✓
NUR	55.4	333.0	118.8	✓	✓
PMG	77.2	104.2	290.2	*	
PRE	61.6	227.0	50.7	*	✓
SDB	67.5	245.2	63.8	*	
SHK	55.0	59.8	267.7	✓	*
STU	60.3	316.6	97.4	✓	
TAB	31.7	316.2	123.1	*	
TOL	69.8	306.7	83.9	✓	
TRI	56.9	313.5	99.1	✓	
UME	58.8	335.4	116.2	✓	
VAL	72.9	319.9	83.7	✓	*
WIN	68.2	236.3	59.3	✓	

successful rotation was one for which the "P" amplitude was a factor of two or three lower than any S wave. Out of these only about ten were considered good.

The final P and SH waveforms were then passed through a deconvolution operator which removed the response of the WWSSN 15-100 instrument. The process was carried out in the frequency domain using the FFT and is shown by the following equation:

$$F(\omega) = \frac{S(\omega)\ a(\omega)}{I(\omega)} \qquad (2.1)$$

where

$S(\omega)$ = Fourier Transform (F.T.) of the digitized trace

$I(\omega)$ = F. T. of the instrument response

$a(\omega)$ = a light bandpass filter to remove high frequency noise

$F(\omega)$ = F. T. of the deconvolved trace.

The $a(\omega)$ used was simply the Q operator at a low value of $T/Q = 0.25$. In the time domain this is essentially a spike approximately three quarters of a second in duration. The reconvolution of the instrument with the deconvolved trace always reproduced the original record with virtually no change. Since the deconvolutions are for interpretation purposes only, this filter proved quite adequate. Figure 2.3 shows the P and SH data used with their corresponding deconvolutions. Note the African stations AAE and NAI. Gupta et al. (1969) discarded these stations on the basis of their anomalously

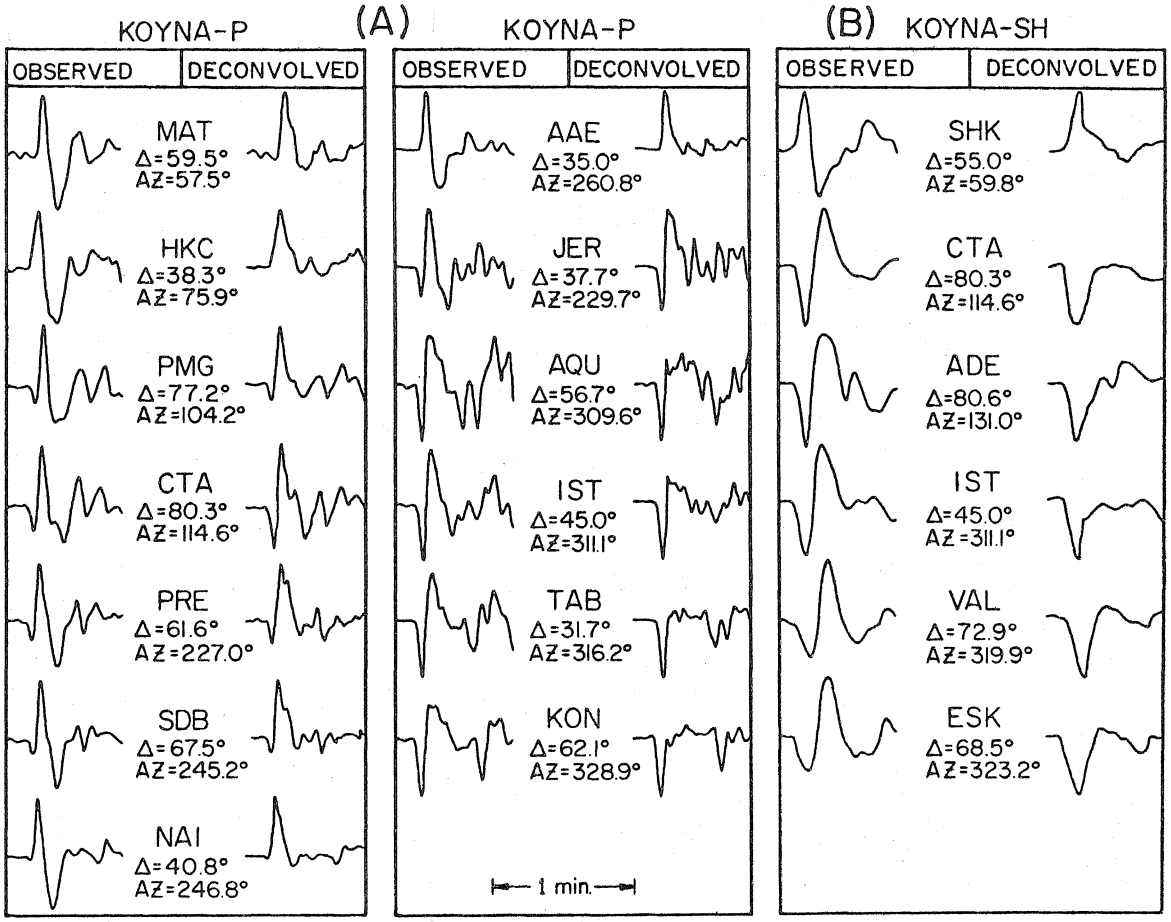

Figure 2.3. a. Long period WWSSN P waveforms used in this study with their respective instrument deconvolutions.
b. SH waveforms.

high positive P residuals claiming that the P first motions were missed. However, these stations proved to be of the highest quality on the basis of noise and amplitude and both short and long period first motions are clear. Long et al. (1973) report that the average P residual beneath these stations is about + 2.5 seconds and attributable to low velocities in the East African upper mantle.

Data Inversion

Since standard techniques for producing a focal mechanism for the Koyna earthquake have proved contradictory, making a starting model proved to be a complicated process. Using the deconvolutions of Figure 2.3 in conjunction with the figures in Chapter 1 trial hypotheses were made for the observed phases. For example, at station PMG (Figure 2.3) the first downswing can be considered to be the direct P wave, and the next prominent upswing, the phase pP or sP. Going to a set of tables for the potential amplitudes as a function of fault orientation, station distance, and azimuth a first order check was made on the interpretations. Figures 2.4a, b, and c show examples of the P, SV, and SH tables, respectively, for one orientation. These were calculated using equations (1.1). A plastic overlay was constructed with the stations put in their relative locations with respect to azimuth and distance. By shifting the overlay in azimuth and comparing the data to the calculated amplitudes and polarities a starting model consistent with the data

P-WAVE POTENTIAL AMPLITUDES UPPER HEMISPHERE

DIP= 67.0 RAKE=-29.2

RAY PARAMETER

AZIMUTH	0.110	0.100	0.090	0.080	0.075	0.068	0.060	0.056	0.050	0.041
0.00	-3.7E -3	-2.5E -3	-1.2E -3	3.4E -5	7.1E -4	1.6E -3	2.7E -3	3.3E -3	4.1E -3	5.4E -3
10.00	-5.2E -3	-3.5E -3	-1.8E -3	-1.9E -4	6.3E -4	1.7E -3	3.0E -3	3.6E -3	4.5E -3	5.8E -3
20.00	-6.3E -3	-4.1E -3	-2.1E -3	-1.2E -4	8.2E -4	2.1E -3	3.4E -3	4.1E -3	5.0E -3	6.4E -3
30.00	-6.7E -3	-4.1E -3	-1.8E -3	3.9E -4	1.4E -3	2.7E -3	4.2E -3	4.8E -3	5.8E -3	7.1E -3
40.00	-6.0E -3	-3.3E -3	-8.0E -4	1.4E -3	2.5E -3	3.8E -3	MAT -3	5.9E -3	6.8E -3	8.0E -3
50.00	-4.2E -3	-1.5E -3	9.7E -4	3.1E -3	4.1E -3	5.4E -3	6.7E -3	7.3E -3	8.1E -3	9.0E -3
60.00	-1.3E -3	1.2E -3	3.5E -3	5.4E -3	HKC -3	7.4E -3	8.5E -3	8.9E -3	9.5E -3	1.0E -2
70.00	2.6E -3	4.8E -3	6.7E -3	8.3E -3	8.9E -3	9.7E -3	1.0E -2	1.0E -2	1.1E -2	1.1E -2
80.00	7.3E -3	9.0E -3	1.0E -2	1.1E -2	1.1E -2	1.2E -2	1.2E -2	1.2E -2	1.3E -2	1.3E -2
90.00	1.2E -2	1.3E -2	1.4E -2	1.4E -2	1.4E -2	1.5E -2	1.4E -2	1.4E -2	PMG -2	1.4E -2
100.00	1.7E -2	1.7E -2	1.8E -2	1.7E -2	1.7E -2	1.7E -2	1.7E -2	1.6E -2	CTA -2	1.5E -2
110.00	2.2E -2	2.1E -2	2.1E -2	2.0E -2	2.0E -2	1.9E -2	1.8E -2	1.8E -2	1.7E -2	1.6E -2
120.00	2.5E -2	2.4E -2	2.4E -2	2.2E -2	2.2E -2	2.1E -2	2.0E -2	1.9E -2	1.8E -2	1.7E -2
130.00	2.8E -2	2.6E -2	2.5E -2	2.4E -2	2.3E -2	2.2E -2	2.1 MUN	2.0E -2	1.9E -2	1.7E -2
140.00	2.8E -2	2.7E -2	2.6E -2	2.4E -2	2.3E -2	2.2E -2	2.1E -2	2.0E -2	1.9E -2	1.7E -2
150.00	2.7E -2	2.6E -2	2.5E -2	2.4E -2	2.3E -2	2.2E -2	2.0E -2	2.0E -2	1.9E -2	1.7E -2
160.00	2.5E -2	2.4E -2	2.3E -2	2.2E -2	2.1E -2	2.0E -2	1.9E -2	1.9E -2	1.8E -2	1.7E -2
170.00	2.1E -2	2.1E -2	2.0E -2	2.0E -2	1.9E -2	1.9E -2	1.8E -2	1.7E -2	1.7E -2	1.6E -2
180.00	1.6E -2	1.7E -2	1.7E -2	1.7E -2	1.6E -2	1.6E -2	1.6E -2	1.6E -2	1.5E -2	1.4E -2
190.00	1.1E -2	1.2E -2	1.3E -2	1.3E -2	1.3E -2	1.3E -2	1.3E -2	1.3E -2	1.3E -2	1.3E -2
200.00	5.9E -3	7.6E -3	8.9E -3	1.0E -2	1.0E -2	1.1E -2	1.1E -2	1.1E -2	1.1E -2	1.2E -2
210.00	8.5E -4	3.0E -3	5.0E -3	6.6E -3	7.4E -3	8.3E -3	PRE -3	9.5E -3	1.0E -2	1.0E -2
220.00	-3.4E -3	-8.1E -4	1.5E -3	3.6E -3	4.5E -3	5.8E -3	7.0E -3	7.5E -3	8.3E -3	9.2E -3
230.00	-6.7E -3	-3.8E -3	-1.2E -3	1.1E -3	2.2E NAI	3.6E -3	5.1E - SDB	5.8E -3	6.7E -3	7.9E -3
240.00	-8.7E -3	-5.8E -3	-3.1E -3	-6.5E -4	AAE	2.0E -3	3.6E -3	4.4E -3	5.4E -3	6.8E -3
250.00	-9.5E -3	-6.7E -3	-4.2E -3	-1.7E -3	3.2E -4	9.1E -4	2.5E -3	3.3E -3	4.4E -3	5.9E -3
260.00	-9.1E -3	-6.7E -3	-4.4E -3	-2.2E -3	-1.1E -3	2.9E -4	1.8E -3	2.6E -3	3.7E -3	5.3E -3
270.00	-7.8E -3	-5.9E -3	-4.0E -3	-2.1E -3	-1.2E -3	1.0E -4	1.5E -3	2.2E -3	3.3E -3	4.8E -3
280.00	-6.0E -3	-4.6E -3	-3.2E -3	-1.6E -3	JER 9E -4	2.3E -4	1.5E -3	2.1E -3	3.1E -3	4.6E -3
290.00	-4.0E -3	-3.1E -3	-2.1E -3	-9.9E -4	5.6E - IST	5.6E - AQU	1.6E -3	2.2E -3	3.1E -3	4.4E -3
300.00	-2.1E -3	-1.7E -3	-1.1E -3	- TAB -4	2.2E -4	9.7E -4	1.9E -3	2.4E -3	3.2E -3	4.4E -3
310.00	-7.5E -4	-6.5E -4	-2.7E -4	3.3E -4	7.2E -4	1.3E -3	KON -3	2.6E -3	3.3E -3	4.4E -3
320.00	-3.0E -5	-5.7E -5	2.0E -4	7.2E -4	1.0E -3	1.6E -3	2.3E -3	2.8E -3	3.4E -3	4.5E -3
330.00	-6.2E -5	-2.7E -5	2.8E -4	8.3E -4	1.1E -3	1.7E -3	2.5E -3	2.9E -3	3.6E -3	4.7E -3
340.00	-8.1E -4	-5.3E -4	-2.0E -5	6.9E -4	1.1E -3	1.7E -3	2.6E -3	3.0E -3	3.7E -3	4.9E -3
350.00	-2.1E -3	-1.4E -3	-6.0E -4	3.8E -4	9.2E -4	1.7E -3	2.6E -3	3.1E -3	3.9E -3	5.1E -3

P-WAVE POTENTIAL AMPLITUDES LOWER HEMISPHERE

DIP= 67.0 RAKE=-29.2

RAY PARAMETER

AZIMUTH	0.110	0.100	0.090	0.080	0.075	0.068	0.060	0.056	0.050	0.041
0.00	1.6E -2	1.7E -2	1.7E -2	1.7E -2	1.6E -2	1.6E -2	1.6E -2	1.6E -2	1.5E -2	1.4E -2
10.00	1.1E -2	1.2E -2	1.3E -2	1.3E -2	1.3E -2	1.3E -2	1.3E -2	1.3E -2	1.3E -2	1.3E -2
20.00	5.9E -3	7.6E -3	8.9E -3	1.0E -2	1.0E -2	1.1E -2	1.1E -2	1.1E -2	1.1E -2	1.2E -2
30.00	8.5E -4	3.0E -3	5.0E -3	6.6E -3	7.4E -3	8.3E -3	9.2E -3	9.5E -3	1.0E -2	1.0E -2
40.00	-3.4E -3	-8.1E -4	1.5E -3	3.6E -3	4.5E -3	5.8E -3	MAT -3	7.5E -3	8.3E -3	9.2E -3
50.00	-6.7E -3	-3.8E -3	-1.2E -3	1.1E -3	2.2E -3	3.6E -3	5.1E -3	5.8E -3	6.7E -3	7.9E -3
60.00	-8.7E -3	-5.8E -3	-3.1E -3	-6.5E -4	HKC 1E -4	2.0E -3	3.6E -3	4.4E -3	5.4E -3	6.8E -3
70.00	-9.5E -3	-6.7E -3	-4.2E -3	-1.7E -3	-6.2E -4	9.1E -4	2.5E -3	3.3E -3	4.4E -3	5.9E -3
80.00	-9.1E -3	-6.7E -3	-4.4E -3	-2.2E -3	-1.1E -3	2.9E -4	1.8E -3	2.6E -3	3.7E -3	5.3E -3
90.00	-7.8E -3	-5.9E -3	-4.0E -3	-2.1E -3	-1.2E -3	1.0E -4	1.5E -3	2.2E -3	PMG -3	4.8E -3
100.00	-6.0E -3	-4.6E -3	-3.2E -3	-1.6E -3	-8.9E -4	2.3E -4	1.5E -3	2.1E -3	CTA -3	4.6E -3
110.00	-4.0E -3	-3.1E -3	-2.1E -3	-9.9E -4	-3.6E -4	5.6E -4	1.6E -3	2.2E -3	3.1E -3	4.4E -3
120.00	-2.1E -3	-1.7E -3	-1.1E -3	-2.6E -4	2.2E -4	9.7E -4	1.9E -3	2.4E -3	3.2E -3	4.4E -3
130.00	-7.5E -4	-6.5E -4	-2.7E -4	3.3E -4	7.2E -4	1.3E -3	2.1E MUN	2.6E -3	3.3E -3	4.4E -3
140.00	-3.0E -5	-5.7E -5	2.0E -4	7.2E -4	1.0E -3	1.6E -3	2.3E -3	2.8E -3	3.4E -3	4.5E -3
150.00	-6.2E -5	-2.7E -5	2.8E -4	8.3E -4	1.1E -3	1.7E -3	2.5E -3	2.9E -3	3.6E -3	4.7E -3
160.00	-8.1E -4	-5.3E -4	-2.0E -5	6.9E -4	1.1E -3	1.7E -3	2.6E -3	3.0E -3	3.7E -3	4.9E -3
170.00	-2.1E -3	-1.4E -3	-6.0E -4	3.8E -4	9.2E -4	1.7E -3	2.6E -3	3.1E -3	3.9E -3	5.1E -3
180.00	-3.7E -3	-2.5E -3	-1.2E -3	3.4E -5	7.1E -4	1.6E -3	2.7E -3	3.3E -3	4.1E -3	5.4E -3
190.00	-5.2E -3	-3.5E -3	-1.8E -3	-1.9E -4	6.3E -4	1.7E -3	3.0E -3	3.6E -3	4.5E -3	5.8E -3
200.00	-6.3E -3	-4.1E -3	-2.1E -3	-1.2E -4	8.2E -4	2.1E -3	3.4E -3	4.1E -3	5.0E -3	6.4E -3
210.00	-6.7E -3	-4.1E -3	-1.8E -3	3.9E -4	1.4E -3	2.7E -3	PRE -3	4.8E -3	5.8E -3	7.1E -3
220.00	-6.0E -3	-3.3E -3	-8.0E -4	1.4E -3	2.5E -3	3.8E -3	5.3E -3	5.9E -3	6.8E -3	8.0E -3
230.00	-4.2E -3	-1.5E -3	9.7E -4	3.1E -3	4.1E NAI	5.4E -3	6.7E - SDB	7.3E -3	8.1E -3	9.0E -3
240.00	-1.3E -3	1.2E -3	3.5E -3	5.4E - AAE	6.3E -3	7.4E -3	8.5E -3	8.9E -3	9.5E -3	1.0E -2
250.00	2.6E -3	4.8E -3	6.7E -3	8.3E -	8.9E -3	9.7E -3	1.0E -2	1.0E -2	1.1E -2	1.1E -2
260.00	7.3E -3	9.0E -3	1.0E -2	1.1E -2	1.1E -2	1.2E -2	1.2E -2	1.2E -2	1.3E -2	1.3E -2
270.00	1.2E -2	1.3E -2	1.4E -2	1.4E -2	1.4E -2	1.5E -2	1.4E -2	1.4E -2	1.4E -2	1.4E -2
280.00	1.7E -2	1.7E -2	1.8E -2	1.7E -2	JER 7E -2	1.7E -2	1.7E -2	1.6E -2	1.6E -2	1.5E -2
290.00	2.2E -2	2.1E -2	2.1E -2	2.0E -2	2.0E -2	1.9E -2	1.8E -2	1.8E -2	1.7E -2	1.6E -2
300.00	2.5E -2	2.4E -2	2.4E -2	TAB -2	2.2E - IST	2.1E - AQU	2.0E -2	1.9E -2	1.8E -2	1.7E -2
310.00	2.8E -2	2.6E -2	2.5E -2	2.4E -2	2.3E -2	2.2E -2	KON -2	2.0E -2	1.9E -2	1.7E -2
320.00	2.8E -2	2.7E -2	2.6E -2	2.4E -2	2.3E -2	2.2E -2	2.1E -2	2.0E -2	1.9E -2	1.7E -2
330.00	2.7E -2	2.6E -2	2.5E -2	2.4E -2	2.3E -2	2.2E -2	2.0E -2	2.0E -2	1.9E -2	1.7E -2
340.00	2.5E -2	2.4E -2	2.3E -2	2.2E -2	2.1E -2	2.0E -2	1.9E -2	1.9E -2	1.8E -2	1.7E -2
350.00	2.1E -2	2.1E -2	2.0E -2	2.0E -2	1.9E -2	1.9E -2	1.8E -2	1.7E -2	1.7E -2	1.6E -2

Figure 2.4. a. P-wave potential amplitude plotted as a function of ray parameter and azimuth.

SV-WAVE POTENTIAL AMPLITUDES UPPER HEMISPHERE

DIP= 67.0 RAKE=-29.2

RAY PARAMETER

AZIMUTH	0.110	0.100	0.090	0.080	0.075	0.068	0.060	0.056	0.050	0.041
0.00	2.9E -2	3.0E -2	3.0E -2	3.1E -2	3.1E -2	3.1E -2	3.1E -2	3.1E -2	3.1E -2	3.0E -2
10.00	3.4E -2	3.4E -2	3.3E -2	3.3E -2	3.2E -2	3.2E -2	3.1E -2	3.0E -2	3.0E -2	2.9E -2
20.00	3.8E -2	3.6E -2	3.5E -2	3.4E -2	3.3E -2	3.1E -2	3.0E -2	2.9E -2	2.8E -2	2.6E -2
30.00	4.0E -2	3.8E -2	3.5E -2	3.3E -2	3.2E -2	3.0E -2	2.8E -2	2.7E -2	2.5E -2	2.3E -2
40.00	3.9E -2	3.7E -2	3.4E -2	3.1E -2	2.9E -2	2.7E -2	MAT -2	2.3E -2	2.1E -2	1.8E -2
50.00	3.6E -2	3.3E -2	3.0E -2	2.6E -2	2.5E -2	2.2E -2	1.9E -2	1.8E -2	1.5E -2	1.2E -2
60.00	3.0E -2	2.7E -2	2.3E -2	2.0E -2	HKC 3E -2	1.5E -2	1.2E -2	1.1E -2	9.0E -3	5.5E -3
70.00	2.2E -2	1.9E -2	1.5E -2	1.1E -2	1.0E -2	7.6E -3	4.7E -3	3.2E -3	1.0E -3	-2.1E -3
80.00	1.2E -2	8.9E -3	5.6E -3	2.3E -3	6.5E -4	-1.6E -3	-4.2E -3	-5.5E -3	-7.4E -3	-1.0E -2
90.00	8.9E -4	-2.1E -3	-5.0E -3	-7.9E -3	-9.3E -3	-1.1E -2	-1.3E -2	-1.4E -2	PMG .6E -2	-1.8E -2
100.00	-1.0E -2	-1.3E -2	-1.5E -2	-1.7E -2	-1.9E -2	-2.0E -2	-2.2E -2	-2.3E -2	- CTA -2	-2.5E -2
110.00	-2.0E -2	-2.2E -2	-2.4E -2	-2.6E -2	-2.7E -2	-2.8E -2	-2.9E -2	-3.0E -2	-3.1E -2	-3.2E -2
120.00	-2.9E -2	-3.0E -2	-3.2E -2	-3.3E -2	-3.4E -2	-3.5E -2	-3.5E -2	-3.6E -2	-3.6E -	-3.7E -2
130.00	-3.4E -2	-3.5E -2	-3.7E -2	-3.8E -2	-3.8E -2	-3.9E -2	-3.9E MUN	-3.9E -2	-3.9E -2	-4.0E -2
140.00	-3.6E -2	-3.7E -2	-3.8E -2	-3.9E -2	-3.9E -2	-4.0E -2	-4.0E -2	-4.0E -2	-4.0E -2	-4.0E -2
150.00	-3.4E -2	-3.5E -2	-3.6E -2	-3.7E -2	-3.8E -2	-3.8E -2	-3.8E -2	-3.9E -2	-3.9E -2	-3.9E -2
160.00	-2.8E -2	-3.0E -2	-3.1E -2	-3.2E -2	-3.3E -2	-3.3E -2	-3.4E -2	-3.4E -2	-3.5E -2	-3.5E -2
170.00	-2.0E -2	-2.2E -2	-2.3E -2	-2.5E -2	-2.5E -2	-2.6E -2	-2.7E -2	-2.8E -2	-2.9E -2	-2.9E -2
180.00	-9.4E -3	-1.1E -2	-1.3E -2	-1.5E -2	-1.6E -2	-1.8E -2	-1.9E -2	-2.0E -2	-2.1E -2	-2.2E -2
190.00	2.5E -3	-4.4E -5	-2.5E -3	-5.1E -3	-6.3E -3	-8.0E -3	-9.9E -3	-1.0E -2	-1.2E -2	-1.4E -2
200.00	1.4E -2	1.1E -2	8.7E -3	5.8E -3	4.3E -3	2.3E -3	-2.1E -6	-1.1E -3	-2.9E -3	-5.4E -3
210.00	2.5E -2	2.2E -2	1.9E -2	1.6E -2	1.4E -2	1.2E -2	PRE -3	8.3E -3	6.3E -3	3.2E -3
220.00	3.4E -2	3.1E -2	2.8E -2	2.5E -2	2.3E -2	2.1E -2	1.8E -2	1.6E -2	1.4E -2	1.1E -2
230.00	4.1E -2	3.8E -2	3.5E -2	3.2E -2	3.0E NAI	2.8E -2	2.5E - SDB	2.4E -2	2.2E -2	1.8E -2
240.00	4.5E -2	4.2E -2	4.0E -2	3.7E -2	3.5E -2	3.3E -2	3.1E -2	2.9E -2	2.7E -2	2.4E -2
250.00	4.5E -2	4.3E -2	4.1E -2	3.9E - AAE	3.8E -2	3.6E -2	3.4E -2	3.3E -2	3.2E -2	2.9E -2
260.00	4.3E -2	4.2E -2	4.1E -2	4.0E -2	3.9E -2	3.8E -2	3.6E -2	3.5E -2	3.4E -2	3.2E -2
270.00	3.9E -2	3.9E -2	3.9E -2	3.8E -2	3.8E -2	3.7E -2	3.6E -2	3.6E -2	3.5E -2	3.4E -2
280.00	3.4E -2	3.5E -2	3.5E -2	3.6E -2	JER 3E -2	3.6E -2	3.6E -2	3.6E -2	3.5E -2	3.5E -2
290.00	2.9E -2	3.0E -2	3.1E -2	3.3E -2	3.3E -2	3.4E -2	3.4E -2	3.5E -2	3.5E -2	3.5E -2
300.00	2.4E -2	2.6E -2	2.8E -2	TAB -2	3.0E -2	IST 3.2E -2	AQU 3.3E -2	3.3E -2	3.4E -2	3.5E -2
310.00	2.0E -2	2.3E -2	2.5E -2	2.7E -2	2.8E -2	3.0E -2	KON -2	3.2E -2	3.3E -2	3.4E -2
320.00	1.8E -2	2.1E -2	2.4E -2	2.6E -2	2.7E -2	2.9E -2	3.0E -2	3.1E -2	3.2E -2	3.4E -2
330.00	1.9E -2	2.1E -2	2.4E -2	2.6E -2	2.7E -2	2.8E -2	3.0E -2	3.0E -2	3.2E -2	3.3E -2
340.00	2.1E -2	2.3E -2	2.5E -2	2.7E -2	2.8E -2	2.9E -2	3.0E -2	3.0E -2	3.1E -2	3.2E -2
350.00	2.5E -2	2.6E -2	2.7E -2	2.9E -2	2.9E -2	3.0E -2	3.0E -2	3.1E -2	3.1E -2	3.1E -2

SV-WAVE POTENTIAL AMPLITUDES LOWER HEMISPHERE

DIP= 67.0 RAKE=-29.2

RAY PARAMETER

AZIMUTH	0.110	0.100	0.090	0.080	0.075	0.068	0.060	0.056	0.050	0.041
0.00	9.4E -3	1.1E -2	1.3E -2	1.5E -2	1.6E -2	1.8E -2	1.9E -2	2.0E -2	2.1E -2	2.2E -2
10.00	-2.5E -3	4.3E -5	2.5E -3	5.1E -3	6.3E -3	8.0E -3	9.9E -3	1.0E -2	1.2E -2	1.4E -2
20.00	-1.4E -2	-1.1E -2	-8.7E -3	-5.8E -3	-4.3E -3	-2.3E -3	2.1E -6	1.1E -3	2.9E -3	5.4E -3
30.00	-2.5E -2	-2.2E -2	-1.9E -2	-1.6E -2	-1.4E -2	-1.2E -2	-9.6E -3	-8.3E -3	-6.3E -3	-3.2E -3
40.00	-3.4E -2	-3.1E -2	-2.8E -2	-2.5E -2	-2.3E -2	-2.1E -2	MAT E -2	-1.6E -2	-1.4E -2	-1.1E -2
50.00	-4.1E -2	-3.8E -2	-3.5E -2	-3.2E -2	-3.0E -2	-2.8E -2	-2.5E -2	-2.4E -2	-2.2E -2	-1.8E -2
60.00	-4.5E -2	-4.2E -2	-4.0E -2	-3.7E -2	HKC 3E -2	-3.3E -2	-3.1E -2	-2.9E -2	-2.7E -2	-2.4E -2
70.00	-4.5E -2	-4.3E -2	-4.1E -2	-3.9E -2	-3.8E -2	-3.6E -2	-3.4E -2	-3.3E -2	-3.2E -2	-2.9E -2
80.00	-4.3E -2	-4.2E -2	-4.1E -2	-4.0E -2	-3.9E -2	-3.8E -2	-3.6E -2	-3.5E -2	-3.4E -2	-3.2E -2
90.00	-3.9E -2	-3.9E -2	-3.9E -2	-3.8E -2	-3.8E -2	-3.7E -2	-3.6E -2	-3.6E -2	PMG .5E -2	-3.4E -2
100.00	-3.4E -2	-3.5E -2	-3.5E -2	-3.6E -2	-3.6E -2	-3.6E -2	-3.6E -2	-3.6E -2	- CTA -2	-3.5E -2
110.00	-2.9E -2	-3.0E -2	-3.1E -2	-3.3E -2	-3.3E -2	-3.4E -2	-3.4E -2	-3.5E -2	-3.5E -2	-3.5E -2
120.00	-2.4E -2	-2.6E -2	-2.8E -2	-3.0E -2	-3.0E -2	-3.2E -2	-3.3E -2	-3.3E -2	-3.4E -	-3.5E -2
130.00	-2.0E -2	-2.3E -2	-2.5E -2	-2.7E -2	-2.8E -2	-3.0E -2	-3.1E MUN	-3.2E -2	-3.3E -2	-3.4E -2
140.00	-1.8E -2	-2.1E -2	-2.4E -2	-2.6E -2	-2.7E -2	-2.9E -2	-3.0E -2	-3.1E -2	-3.2E -2	-3.4E -2
150.00	-1.9E -2	-2.1E -2	-2.4E -2	-2.6E -2	-2.7E -2	-2.8E -2	-3.0E -2	-3.0E -2	-3.2E -2	-3.3E -2
160.00	-2.1E -2	-2.3E -2	-2.5E -2	-2.7E -2	-2.8E -2	-2.9E -2	-3.0E -2	-3.0E -2	-3.1E -2	-3.2E -2
170.00	-2.5E -2	-2.6E -2	-2.7E -2	-2.9E -2	-2.9E -2	-3.0E -2	-3.0E -2	-3.1E -2	-3.1E -2	-3.1E -2
180.00	-2.9E -2	-3.0E -2	-3.0E -2	-3.1E -2	-3.1E -2	-3.1E -2	-3.1E -2	-3.1E -2	-3.1E -2	-3.0E -2
190.00	-3.4E -2	-3.4E -2	-3.3E -2	-3.3E -2	-3.2E -2	-3.2E -2	-3.1E -2	-3.0E -2	-3.0E -2	-2.9E -2
200.00	-3.8E -2	-3.6E -2	-3.5E -2	-3.4E -2	-3.3E -2	-3.1E -2	-3.0E -2	-2.9E -2	-2.8E -2	-2.6E -2
210.00	-4.0E -2	-3.8E -2	-3.5E -2	-3.3E -2	-3.2E -2	-3.0E -2	- PRE -2	-2.7E -2	-2.5E -2	-2.3E -2
220.00	-3.9E -2	-3.7E -2	-3.4E -2	-3.1E -2	-2.9E -2	-2.7E -2	-2.4E -2	-2.3E -2	-2.1E -2	-1.8E -2
230.00	-3.6E -2	-3.3E -2	-3.0E -2	-2.6E -2	-2.5E NAI	-2.2E -2	-1.9E -2 SDB	1.8E -2	-1.5E -2	-1.2E -2
240.00	-3.0E -2	-2.7E -2	-2.3E -2	-2.0E -2	-1.8E -2	-1.5E -2	-1.2E -2	-1.1E -2	-9.0E -3	-5.5E -3
250.00	-2.2E -2	-1.9E -2	-1.5E -2	-1.1E - AAE	1.0E -2	-7.6E -3	-4.7E -3	-3.2E -3	-1.0E -3	2.1E -3
260.00	-1.2E -2	-8.9E -3	-5.6E -3	-2.3E -3	-6.5E -4	1.6E -3	4.2E -3	5.5E -3	7.4E -3	1.0E -2
270.00	-8.9E -4	2.1E -3	5.0E -3	7.9E -3	9.3E -3	1.1E -2	1.3E -2	1.4E -2	1.6E -2	1.8E -2
280.00	1.0E -2	1.3E -2	1.5E -2	1.7E -2	JER E -2	2.0E -2	2.2E -2	2.3E -2	2.4E -2	2.5E -2
290.00	2.0E -2	2.2E -2	2.4E -2	2.6E -2	2.7E -2	2.8E -2	2.9E -2	3.0E -2	3.1E -2	3.2E -2
300.00	2.9E -2	3.0E -2	3.2E -2	TAB -2	3.4E -2	IST 3.5E -2	AQU 3.5E -2	3.6E -2	3.6E -2	3.7E -2
310.00	3.4E -2	3.5E -2	3.7E -2	3.8E -2	3.8E -2	3.9E -2	KON -2	3.9E -2	3.9E -2	4.0E -2
320.00	3.6E -2	3.7E -2	3.8E -2	3.9E -2	3.9E -2	4.0E -2	4.0E -2	4.0E -2	4.0E -2	4.0E -2
330.00	3.4E -2	3.5E -2	3.6E -2	3.7E -2	3.8E -2	3.8E -2	3.8E -2	3.9E -2	3.9E -2	3.9E -2
340.00	2.8E -2	3.0E -2	3.1E -2	3.2E -2	3.3E -2	3.3E -2	3.4E -2	3.4E -2	3.5E -2	3.5E -2
350.00	2.0E -2	2.2E -2	2.3E -2	2.5E -2	2.5E -2	2.6E -2	2.7E -2	2.8E -2	2.9E -2	2.9E -2

Figure 2.4. b. SV amplitude. Same scheme as (a).

SH-WAVE POTENTIAL AMPLITUDES UPPER HEMISPHERE

DIP= 67.0 RAKE=-29.2

RAY PARAMETER

AZIMUTH	0.255	0.228	0.158	0.138	0.130	0.118	0.108	0.097	0.087	0.071
0.00	5.1E -2	4.4E -2	2.3E -2	1.5E -2	1.1E -2	4.5E -3	-2.1E -3	-1.1E -2	-2.0E -2	-4.2E -2
10.00	5.0E -2	4.2E -2	1.8E -2	8.3E -3	3.7E -3	-4.2E -3	-1.2E -2	-2.2E -2	-3.3E -2	-5.8E -2
20.00	4.1E -2	3.2E -2	5.9E -3	-4.9E -3	-1.0E -2	-1.8E -2	-2.7E -2	-3.8E -2	-5.1E -2	-7.8E -2
30.00	2.6E -2	1.6E -2	-1.1E -2	-2.3E -2	-2.8E -2	-3.8E -2	-4.7E -2	-5.9E -2	-7.3E -2	-1.0E -1
40.00	5.7E -3	-4.0E -3	-3.3E -2	-4.5E -2	-5.1E -2	-6.0E -2	-7.0E -2	-8.2E -2	-9.6E -2	-1.2E -1
50.00	-1.7E -2	-2.6E -2	-5.6E -2	-6.8E -2	-7.3E -2	-8.3E -2	-9.3E -2	-1.0E -1	-1.1E -1	-1.4E -1
60.00	-3.9E -2	-4.9E -2	-7.7E -2	-8.9E -2	-9.4E -2	-1.0E -1	-1.1E -1	-1.2E -1	-1.3E -1	-1.6E -1
70.00	-5.9E -2	-6.7E -2	-9.4E -2	-1.0E -1	-1.1E -1	-1.1E -1	-1.2E -1	-1.3E -1	-1.5E -1	-1.7E -1
80.00	-7.3E -2	-8.1E -2	-1.0E -1	-1.1E -1	-1.1E -1	-1.2E -1	-1.3E -1	-1.4E -1	-1.5E -1	-1.7E -1
90.00	-7.9E -2	-8.6E -2	-1.0E -1	-1.1E -1	-1.2E -1	-1.2E -1	-1.3E -1	-1.4E -1	-1.5E -1	-1.7E -1
100.00	-7.7E -2	-8.3E -2	-1.0E -1	-1.0E -1	-1.1E -1	-1.1E -1	-1.2E -1	-1.2E -1	-1.4E -1	-1.5E -1
110.00	-6.7E -2	-7.2E -2	-8.4E -2	-8.9E -2	-9.2E -2	-9.6E -2	-1.0E -1	-1.0E -1	-1.1E -1	-1.2E -1
120.00	-5.0E -2	-5.2E -2	-6.0E -2	-6.3E -2	-6.5E -2	-6.7E -2	-7.0E -2	-7.3E -2	-7.7E -2	-8.5E -2
130.00	-2.7E -2	-2.8E -2	-3.0E -2	-3.1E -2	-3.2E -2	-3.3E -2	-3.4E -2	-3.5E -2	-3.6E -2	-3.9E -2
140.00	-1.0E -3	-2.2E -4	2.2E -3	3.2E -3	3.7E -3	4.5E -3	5.3E -3	6.4E -3	7.5E -3	1.0E -2
150.00	2.5E -2	2.7E -2	3.5E -2	3.8E -2	4.0E -2	4.2E -2	4.4E -2	4.8E -2	5.1E -2	5.9E -2
160.00	4.9E -2	5.3E -2	6.5E -2	7.0E -2	7.3E -2	7.7E -2	8.1E -2	8.6E -2	9.2E -2	1.0E -1
170.00	6.8E -2	7.3E -2	9.0E -2	9.7E -2	1.0E -1	1.0E -1	1.1E -1	1.1E -1	1.2E -1	1.4E -1
180.00	7.9E -2	8.6E -2	1.0E -1	1.1E -1	1.1E -1	1.2E -1	1.3E -1	1.4E -1	1.5E -1	1.7E -1
190.00	8.2E -2	9.0E -2	1.1E -1	1.2E -1	1.2E -1	1.3E -1	1.4E -1	1.5E -1	1.6E -1	1.9E -1
200.00	7.7E -2	8.6E -2	1.1E -1	1.2E -1	1.2E -1	1.3E -1	1.4E -1	1.5E -1	1.7E -1	1.9E -1
210.00	6.4E -2	7.3E -2	1.0E -1	1.1E -1	1.1E -1	1.2E -1	1.3E -1	1.5E -1	1.6E -1	1.9E -1
220.00	4.5E -2	5.5E -2	8.4E -2	9.6E -2	1.0E -1	1.1E -1	1.2E -1	1.3E -1	1.4E -1	1.7E -1
230.00	2.2E -2	3.2E -2	6.1E -2	7.3E -2	7.9E -2	8.8E -2	9.8E -2	1.1E -1	1.2E -1	1.5E -1
240.00	-1.2E -3	8.2E -3	3.6E -2	4.8E -2	5.3E -2	6.3E -2	7.2E -2	8.4E -2	9.8E -2	1.2E -1
250.00	-2.3E -2	-1.4E -2	1.2E -2	2.3E -2	2.8E -2	3.7E -2	4.6E -2	5.7E -2	7.0E -2	9.7E -2
260.00	-4.0E -2	-3.2E -2	-8.1E -3	1.6E -3	6.3E -3	1.4E -2	2.2E -2	3.2E -2	4.4E -2	6.8E -2
270.00	-5.1E -2	-4.4E -2	-2.3E -2	-1.5E -2	-1.1E -2	-4.1E -3	2.6E -3	1.1E -2	2.1E -2	4.2E -2
280.00	-5.5E -2	-4.9E -2	-3.2E -2	-2.5E -2	-2.2E -2	-1.6E -2	-1.1E -2	-3.8E -3	4.2E -3	2.1E -2
290.00	-5.1E -2	-4.6E -2	-3.4E -2	-2.9E -2	-2.6E -2	-2.2E -2	-1.8E -2	-1.3E -2	-7.2E -3	5.6E -3
300.00	-4.0E -2	-3.7E -2	-2.9E -2	-2.6E -2	-2.5E -2	-2.2E -2	-2.0E -2	-1.6E -2	-1.3E -2	-5.1E -3
310.00	-2.3E -2	-2.2E -2	-2.0E -2	-1.9E -2	-1.8E -2	-1.7E -2	-1.6E -2	-1.4E -2	-1.4E -2	-1.1E -2
320.00	-4.3E -3	-5.2E -3	-7.6E -3	-8.6E -3	-9.1E -3	-9.9E -3	-1.0E -2	-1.1E -2	-1.3E -2	-1.5E -2
330.00	1.5E -2	1.2E -2	5.2E -3	2.1E -3	7.4E -4	-1.7E -3	-4.1E -3	-7.4E -3	-1.1E -2	-1.8E -2
340.00	3.2E -2	2.8E -2	1.6E -2	1.1E -2	8.7E -3	4.7E -3	6.9E -4	-4.6E -3	-1.0E -2	-2.3E -2
350.00	4.5E -2	3.9E -2	2.2E -2	1.6E -2	1.2E -2	7.3E -3	1.8E -3	-5.3E -3	-1.3E -2	-3.0E -2

SH-WAVE POTENTIAL AMPLITUDES LOWER HEMISPHERE

DIP= 67.0 RAKE=-29.2

RAY PARAMETER

AZIMUTH	0.255	0.228	0.158	0.138	0.130	0.118	0.108	0.097	0.087	0.071
0.00	7.9E -2	8.6E -2	1.0E -1	1.1E -1	1.1E -1	1.2E -1	1.3E -1	1.4E -1	1.5E -1	1.7E -1
10.00	8.2E -2	9.0E -2	1.1E -1	1.2E -1	1.2E -1	1.3E -1	1.4E -1	1.5E -1	1.6E -1	1.9E -1
20.00	7.7E -2	8.6E -2	1.1E -1	1.2E -1	1.2E -1	1.3E -1	1.4E -1	1.5E -1	1.7E -1	1.9E -1
30.00	6.4E -2	7.3E -2	1.0E -1	1.1E -1	1.1E -1	1.2E -1	1.3E -1	1.5E -1	1.6E -1	1.9E -1
40.00	4.5E -2	5.5E -2	8.4E -2	9.6E -2	1.0E -1	1.1E -1	1.2E -1	1.3E -1	1.4E -1	1.7E -1
50.00	2.2E -2	3.2E -2	6.1E -2	7.3E -2	7.9E -2	8.8E -2	9.8E -2	1.1E -1	1.2E -1	1.5E -1
60.00	-1.2E -3	8.2E -3	3.6E -2	4.8E -2	5.3E -2	6.3E -2	7.2E -2	8.4E -2	9.8E -2	1.2E -1
70.00	-2.3E -2	-1.4E -2	1.2E -2	2.3E -2	2.8E -2	3.7E -2	4.6E -2	5.7E -2	7.0E -2	9.7E -2
80.00	-4.0E -2	-3.2E -2	-8.1E -3	1.6E -3	6.3E -3	1.4E -2	2.2E -2	3.2E -2	4.4E -2	6.8E -2
90.00	-5.1E -2	-4.4E -2	-2.3E -2	-1.5E -2	-1.1E -2	-4.1E -3	2.6E -3	1.1E -2	2.1E -2	4.2E -2
100.00	-5.5E -2	-4.9E -2	-3.2E -2	-2.5E -2	-2.2E -2	-1.6E -2	-1.1E -2	-3.8E -3	4.2E -3	2.1E -2
110.00	-5.1E -2	-4.6E -2	-3.4E -2	-2.9E -2	-2.6E -2	-2.2E -2	-1.8E -2	-1.3E -2	-7.2E -3	5.6E -3
120.00	-4.0E -2	-3.7E -2	-2.9E -2	-2.6E -2	-2.5E -2	-2.2E -2	-2.0E -2	-1.6E -2	-1.3E -2	-5.1E -3
130.00	-2.3E -2	-2.2E -2	-2.0E -2	-1.9E -2	-1.8E -2	-1.7E -2	-1.6E -2	-1.5E -2	-1.4E -2	-1.1E -2
140.00	-4.3E -3	-5.2E -3	-7.6E -3	-8.6E -3	-9.1E -3	-9.9E -3	-1.0E -2	-1.1E -2	-1.3E -2	-1.5E -2
150.00	1.5E -2	1.2E -2	5.2E -3	2.1E -3	7.4E -4	-1.7E -3	-4.1E -3	-7.4E -3	-1.1E -2	-1.8E -2
160.00	3.2E -2	2.8E -2	1.6E -2	1.1E -2	8.7E -3	4.7E -3	6.9E -4	-4.6E -3	-1.0E -2	-2.3E -2
170.00	4.5E -2	3.9E -2	2.2E -2	1.6E -2	1.2E -2	7.3E -3	1.8E -3	-5.3E -3	-1.3E -2	-3.0E -2
180.00	5.1E -2	4.4E -2	2.3E -2	1.5E -2	1.1E -2	4.5E -3	-2.1E -3	-1.1E -2	-2.0E -2	-4.2E -2
190.00	5.0E -2	4.2E -2	1.8E -2	8.3E -3	3.7E -3	-4.2E -3	-1.2E -2	-2.2E -2	-3.3E -2	-5.8E -2
200.00	4.1E -2	3.2E -2	5.9E -3	-4.9E -3	-1.0E -2	-1.8E -2	-2.7E -2	-3.8E -2	-5.1E -2	-7.8E -2
210.00	2.6E -2	1.6E -2	-1.1E -2	-2.3E -2	-2.8E -2	-3.8E -2	-4.7E -2	-5.9E -2	-7.3E -2	-1.0E -1
220.00	5.7E -3	-4.0E -3	-3.3E -2	-4.5E -2	-5.1E -2	-6.0E -2	-7.0E -2	-8.2E -2	-9.6E -2	-1.2E -1
230.00	-1.7E -2	-2.6E -2	-5.6E -2	-6.8E -2	-7.3E -2	-8.3E -2	-9.3E -2	-1.0E -1	-1.1E -1	-1.4E -1
240.00	-3.9E -2	-4.9E -2	-7.7E -2	-8.9E -2	-9.4E -2	-1.0E -1	-1.1E -1	-1.2E -1	-1.3E -1	-1.6E -1
250.00	-5.9E -2	-6.7E -2	-9.4E -2	-1.0E -1	-1.1E -1	-1.1E -1	-1.2E -1	-1.3E -1	-1.5E -1	-1.7E -1
260.00	-7.3E -2	-8.1E -2	-1.0E -1	-1.1E -1	-1.1E -1	-1.2E -1	-1.3E -1	-1.4E -1	-1.5E -1	-1.8E -1
270.00	-7.9E -2	-8.6E -2	-1.0E -1	-1.1E -1	-1.2E -1	-1.2E -1	-1.3E -1	-1.4E -1	-1.5E -1	-1.7E -1
280.00	-7.7E -2	-8.3E -2	-1.0E -1	-1.0E -1	-1.1E -1	-1.1E -1	-1.2E -1	-1.2E -1	-1.3E -1	-1.5E -1
290.00	-6.7E -2	-7.2E -2	-8.4E -2	-8.9E -2	-9.2E -2	-9.6E -2	-1.0E -1	-1.0E -1	-1.1E -1	-1.2E -1
300.00	-5.0E -2	-5.2E -2	-6.0E -2	-6.3E -2	-6.5E -2	-6.7E -2	-7.0E -2	-7.3E -2	-7.7E -2	-8.5E -2
310.00	-2.7E -2	-2.8E -2	-3.0E -2	-3.1E -2	-3.2E -2	-3.3E -2	-3.4E -2	-3.5E -2	-3.6E -2	-3.9E -2
320.00	-1.0E -3	-2.2E -4	2.2E -3	3.2E -3	3.7E -3	4.5E -3	5.3E -3	6.4E -3	7.5E -3	1.0E -2
330.00	2.5E -2	2.7E -2	3.5E -2	3.8E -2	4.0E -2	4.2E -2	4.4E -2	4.8E -2	5.1E -2	5.9E -2
340.00	4.9E -2	5.3E -2	6.5E -2	7.0E -2	7.3E -2	7.7E -2	8.1E -2	8.6E -2	9.2E -2	1.0E -1
350.00	6.8E -2	7.3E -2	9.0E -2	9.7E -2	1.0E -1	1.0E -1	1.1E -1	1.1E -1	1.2E -1	1.4E -1

Figure 2.4. c. SH amplitude. Same scheme as (a).

interpretations was obtained. This process is equivalent to first-motion studies except that the surface reflections are considered also. This is also somewhat similar to some of the methods described by Keilis-Borok (1957) which incorporate standard forms of wave polarizations, to which the data is compared. Once a trial model is deduced it is further tested by computing synthetic seismograms and comparing them with the originals.

Table 2.2 contains the various crustal structures considered in this study. Crust no. 1, obtained from Narain (1973), was used in the starting model calculations and inversions. This model is based on earthquake travel times and surface wave studies so the nature of the boundaries is essentially unknown. This point will be investigated later in the Chapter.

The starting model determined from these trial-and-error techniques is a simple one point-source model with the parameters displayed in Table 2.3. The time function was chosen to be simple triangular pulse characterized by a rise-time, δt_1, and fall-off, δt_2. This was determined mostly by the general shape of the observed phases. A treatment of the errors involved in these assumptions will follow the results.

In the calculations of the starting model and in the inversion, the receiver structure is taken to be a homogeneous halfspace. For P waves impinging under the receiver crust the most important ray in the receiver response is the free surface-to-Moho-to-free surface reflection. Its relative travel time, to the direct arrival, is about

TABLE 2.2

CRUSTAL MODELS

	α(km/sec)	β(km/sec)	ρ(gm/cm^3)	Th(km)
1)	5.7	3.5	2.6	20.0
	6.5	4.0	2.8	20.0
	8.2	4.7	3.2	
2)	5.7	3.5	2.6	15.0
	6.3	3.6	2.7	5.0
	6.8	3.9	2.8	15.0
	7.4	4.3	3.0	5.0
	8.2	4.7	3.2	
3)	6.0	3.5	2.6	20.0
	6.8	3.9	2.8	20.0
	8.2	4.7	3.2	

TABLE 2.3

SOURCE MODELS

	STARTING	FINAL CRUST #1	FINAL CRUST #3
δ	70.0°	67.0	72.0
λ	-30.0°	-29.0	-26.0
θ	30.0°	16.0	20.0
HS	10.0 km	4.4	4.6
δt_1	2.5 sec	2.5	2.5
δt_2	2.5 sec	3.9	4.0

ten seconds for typical crustal models, and its amplitude about ten percent of the direct ray. For SH the first 'bounce' is slightly larger but occurs farther back in the record. At the beginning of the study an attempt was made to estimate receiver crustal structures but was effectively thwarted by the lack of good crustal models beneath the WWSSN stations. Because these arrivals are small they are ignored and can be considered a source of noise in the inversion.

The actual inversion was performed in a step-wise manner. Since it was difficult to find a starting model which would simultaneously fit the SH and P data together only P waves were used first in hopes of bringing the model closer to compatibility. The average fit for the P waves started at .9455, the value of the correlation function, and after two iterations increased to about .9600. The SH waves were then added and it was found that the new starting model was sufficient for the program to continue. After about three more iterations the step-size became negligible and the inversion was terminated. The final model reached an average fit of .9731. Only the first ten to twelve seconds of each record was used because of crustal structure uncertainties which will be discussed in the error analysis. However, nearly all of the important information is contained within this time period. The phases P, pP, sP, S, and sS all arrive within this time because of the shallow source depth.

Table 2.3 gives the results of the inversion. Figure 2.2b gives the focal plot representation. As can be seen, not too much changed except for the depth and strike. Even so, this was significant for the quality of fit, significant in the respect of just fitting the observed first motions and general waveshape behavior. Figure 2.5 shows the data and synthetics for the final model for the time length used. The T/Q parameters used here for P and SH are 1.0 and 4.0, respectively. Figure 2.6 shows the first 60 seconds of the observed P waves and the full synthetic calculation using 24 rays in crust no. 1, Table 2.3, with arrival times up to 26 seconds after the direct P arrivals. The overall fit is striking, although some details are lacking in the synthetics. Generally, the model predicts all stations to have dilatational direct P arrivals except for HKC. The only possible discrepancy may be MAT but the long and short period first motion signal is in the noise so it is certainly acceptable. The synthetic direct P wave for AAE is too large but the first motion on the long and short period records is clearly dilatational. On all stations in the azimuth range between 57° and 300° the prominent upswing after the P wave is most certainly the surface reflections pP or sP. It is interesting to note that this upswing is not the same phase at all stations. In southeastern azimuths it is mostly pP and in southwestern azimuths, sP. The group of stations, AQU, IST, TAB, and KON demonstate a remarkable interference phenomenon which is predicted by the model. Note the deconvolutions of these stations

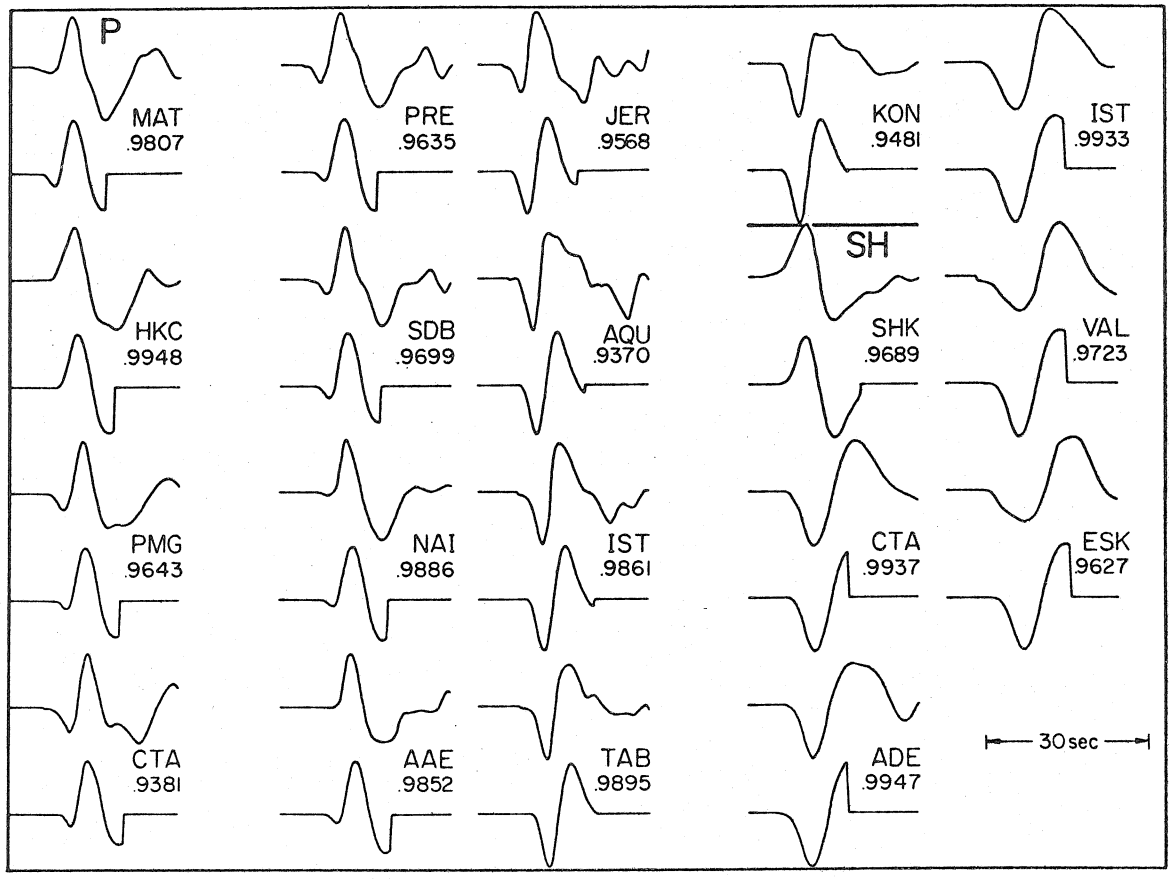

Figure 2.5. Final fit for the combined inversion of the P and SH wave data showing the quality of fit at each station and amount of record used. At each station the observed is on top and the calculated directly below.

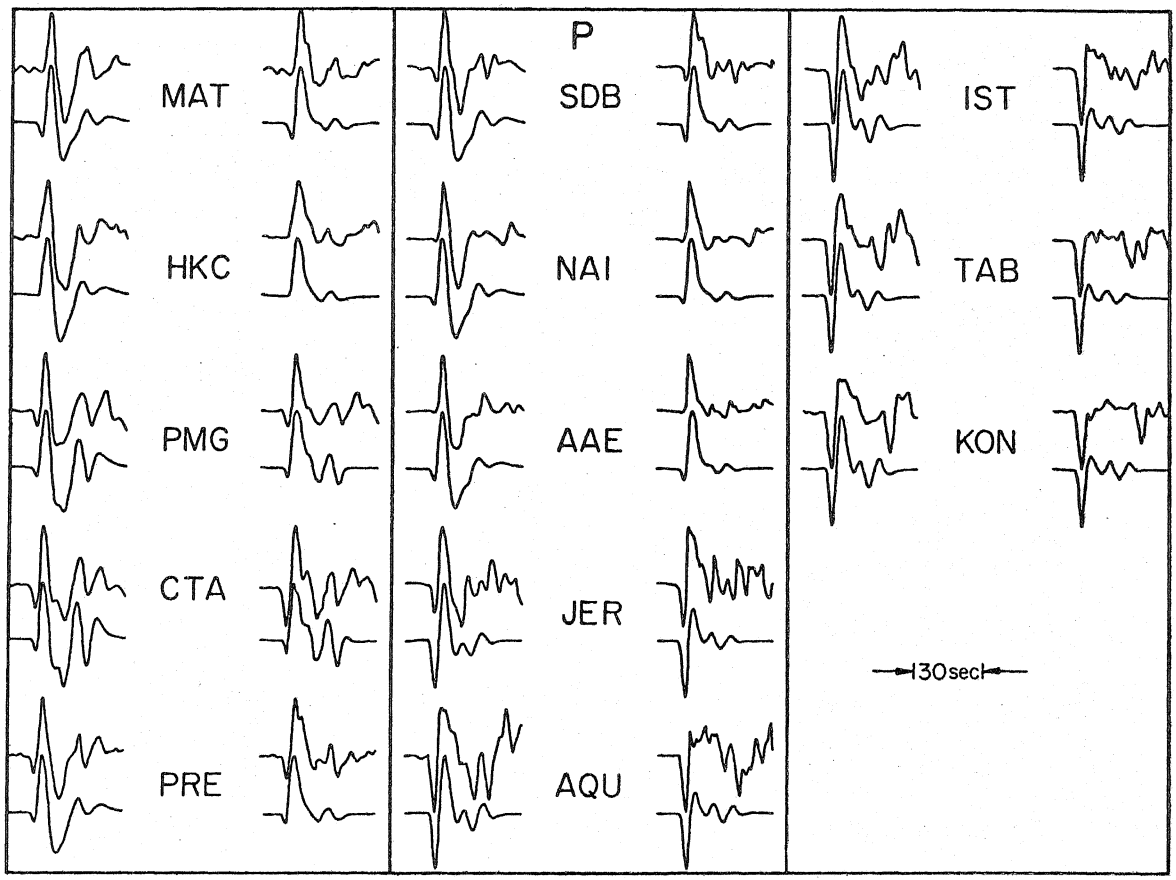

Figure 2.6. Comparison of the observed and calculated P waves for approximately the first 30 seconds of record. At each station the observed is on top with the synthetic directly below. To the left of the station letters are the observed and calculated with the instrument response, and to the right, without the instrument response.

in Figure 2.6. The P wave seems to behave as one sharp dilatational pulse with some smaller oscillations occurring behind it. The model, however, predicts a positive sP phase which is comparable in amplitude to the negative direct P. Because of the extremely shallow source depth and length of the time function, sP is almost totally annihilated by the direct P. It is precisely this interference which controls the depth determination.

Figures 2.4a and 2.4b show where the various stations plot on the focal sphere defined by the computed fault orientation. The amplitudes read off these diagrams can serve as a guide in interpreting the phases in the synthetics. A rough rule of thumb for computing the surface reflections is to multiply -0.8 times the observed amplitude in the upper P hemisphere for pP, and about - 0.4 for sP in the upper SV hemisphere. This will give approximately the correct amplitude ratios for most P, pP, and sP determinations.

In addition to the major crustal phases caused by the free surface there are significant arrivals in the P wave which are caused by internal boundaries such as the Moho and the Conrad discontinuities. These later arrivals usually correspond to rays which suffer not more than one S to P conversion and are mostly in the P mode in the source crust. The major contributors are those which bounce off the Moho, back to the free surface, and then down again. As might be expected these arrivals are not completely coherent over all stations although there are many good correlations between data and synthetic. These

rays will be sensitive to the precise nature of the boundaries and total travel time through the crust. It is speculated that the major reason these arrivals aren't as well behaved as predicted is because of the real earth's deviation from plane isotropic layers or inadequacies in the crustal models. However, the fact that these phases even exist where they do certainly places ambiguity on just what can be attributed to source effects.

Of all the stations used, PMG and CTA undergo the most extreme crustal distortions of the source. Because of strong up-going and down-going SV radiation relative to the P radiation at these distances and azimuths, fairly large S to P conversions occur at the Conrad, Moho, and free surface of crust no. 1, Table 2.2. Since sharp boundaries like these probably do not occur in real crusts a model calculation was done to see what effect changing the nature of these boundaries had on the fits. Figure 2.7 shows the results of such a calculation. The Australian P wave station ADE is included here. It was not included in the formal inversion because of very low amplitude even though there is very little noise. The digitization of this station is somewhat poor because of record-line thickness problems, but is sufficient for semi-quantitative comparisons of relative amplitudes and arrivals. The synthetics made from crust no. 1 in Figure 2.7 show two deficiencies. The calculated direct P wave is too small, in general, and the later arrivals of the S-P phases are too large. The predicted

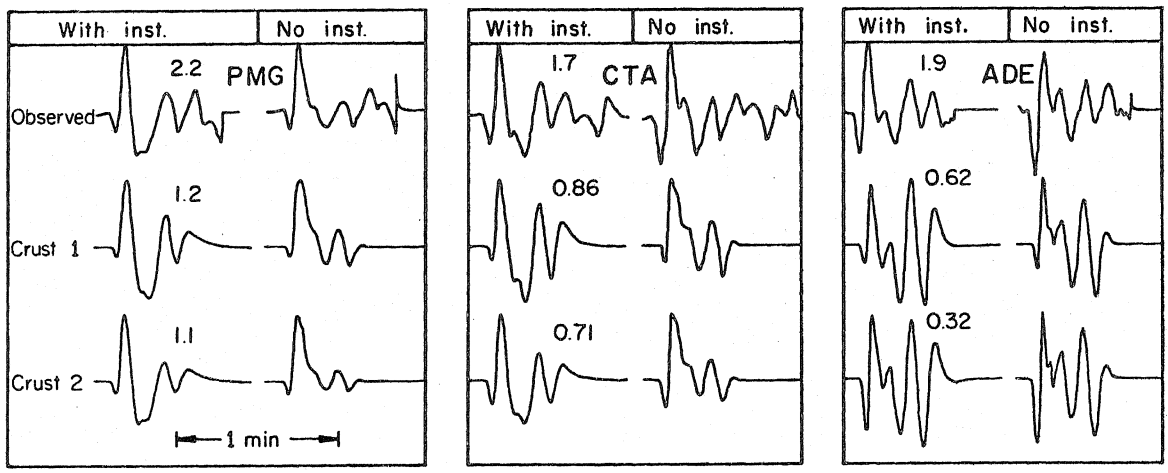

Figure 2.7. Model calculation using two crustal structures involving the three stations which show the greatest structural interference.

for ADE is pathological. However, when small transition layers are put into the crustal structure, crust no. 2, Table 2.2, the synthetics improve their relative amplitude behavior for both the direct P and the later arrivals. The later arrivals at ADE are still too big but the direction of improvement is obvious.

Other crustal effects can also enter in. For example, the effect of a near surface layer can significantly affect the reflection coefficients at the free surface. A layer representing the Deccan traps was not included principally because so little is known of the Koyna crustal structure. Velocity measurements indicate fairly high compressional velocities on the order of 5 to 6 km/sec, Kailasam et al. (1969). This can be used as justification of the crustal model. However, these arguments point out what seems to be the major difficulty with this method: unless the crustal structure is precisely known, exacting source interpretations are very hard to make.

Figure 2.8 shows the observations and synthetics for the SH waves. They behave in a much less complicated fashion than the P waves. Primarily, they contain only the phases S and sS with other crustal multiple playing a minor role. The second major pulse at ADE is probably ScS. The relative J-B arrival time is correct for this range. The stations VAL and ESK show some unpredicted effects. Although the pulse widths as shown by the deconvolutions are comparable, their rise times certainly are not. The data, especially

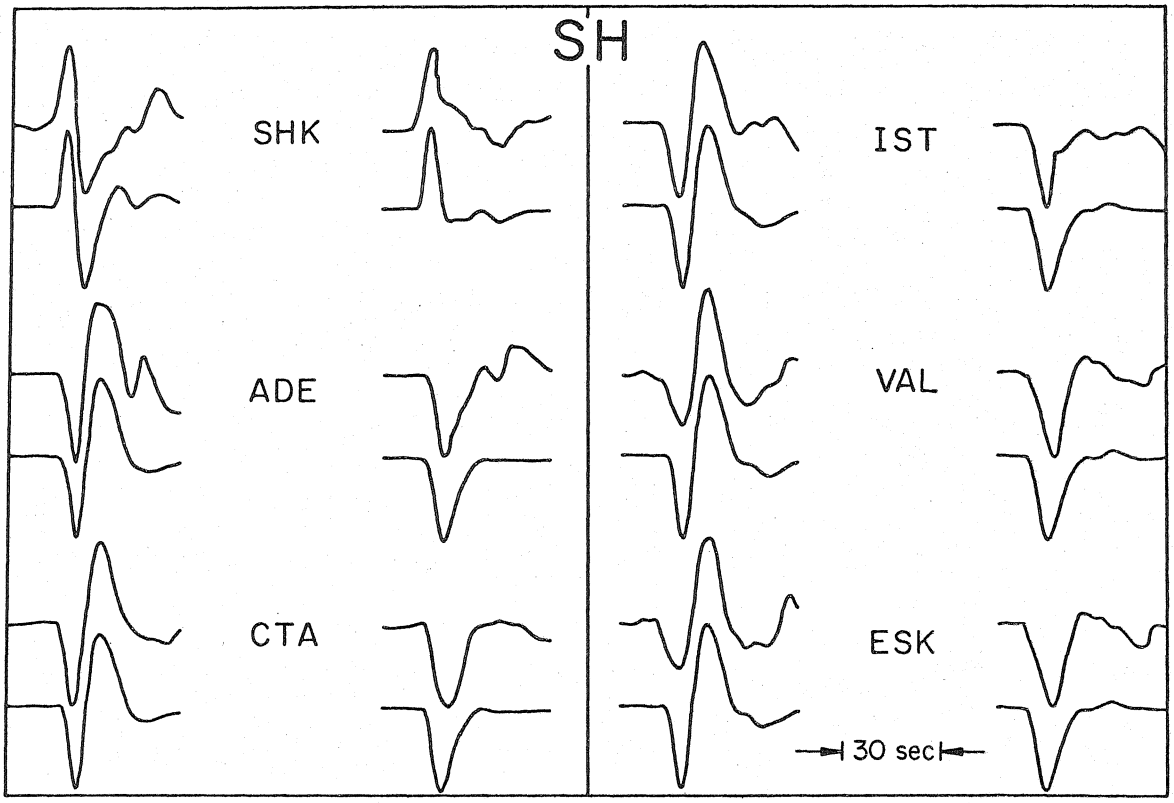

Figure 2.8. Comparison of the observed and calculated SH waveforms. Same scheme as Figure 2.6.

at ESK, have an exceptional slow rise. Several explanations are possible, of course, among them being source directivity and Q effects. Because the data set is so limited, however, no attempt will be made to explain these particular problems.

A comparison of synthetic to data was also done for the high noise and rotated stations for both P and S, and in virtually all cases the qualitative fit was good. Table 2.1 contains these stations. Note, for example, the well defined SH node predicted by the model at an azimuth of about 340°. Figure 2.9 shows the qualitative fit of rotated SH waves near this azimuth with the predicted model.

In addition to the parameters of Table 2.3 the absolute scaling of the synthetics to the data yields a moment determination. Table 2.4 contains the results for the stations used. The P waves exhibit more scatter than the SH waves possibly because they are controlled by the local crustal structure to a larger extent. The average moment for P and SH combined is $3.2 \pm 1.4 \times 10^{25}$ dyne cm.

To determine the relative importance of any particular station to the inversion a useful technique is to examine the eigenvectors of the observations through the use of the data "resolution" matrix, Wiggins (1972), defined by

$$Ru = U\,U^T \qquad (2.2)$$

$(Ru)_{ii}$ contains the least-squares solution for the importance of the ith datum. The closer $(Ru)_{ii}$ is to unity means that the ith datum was

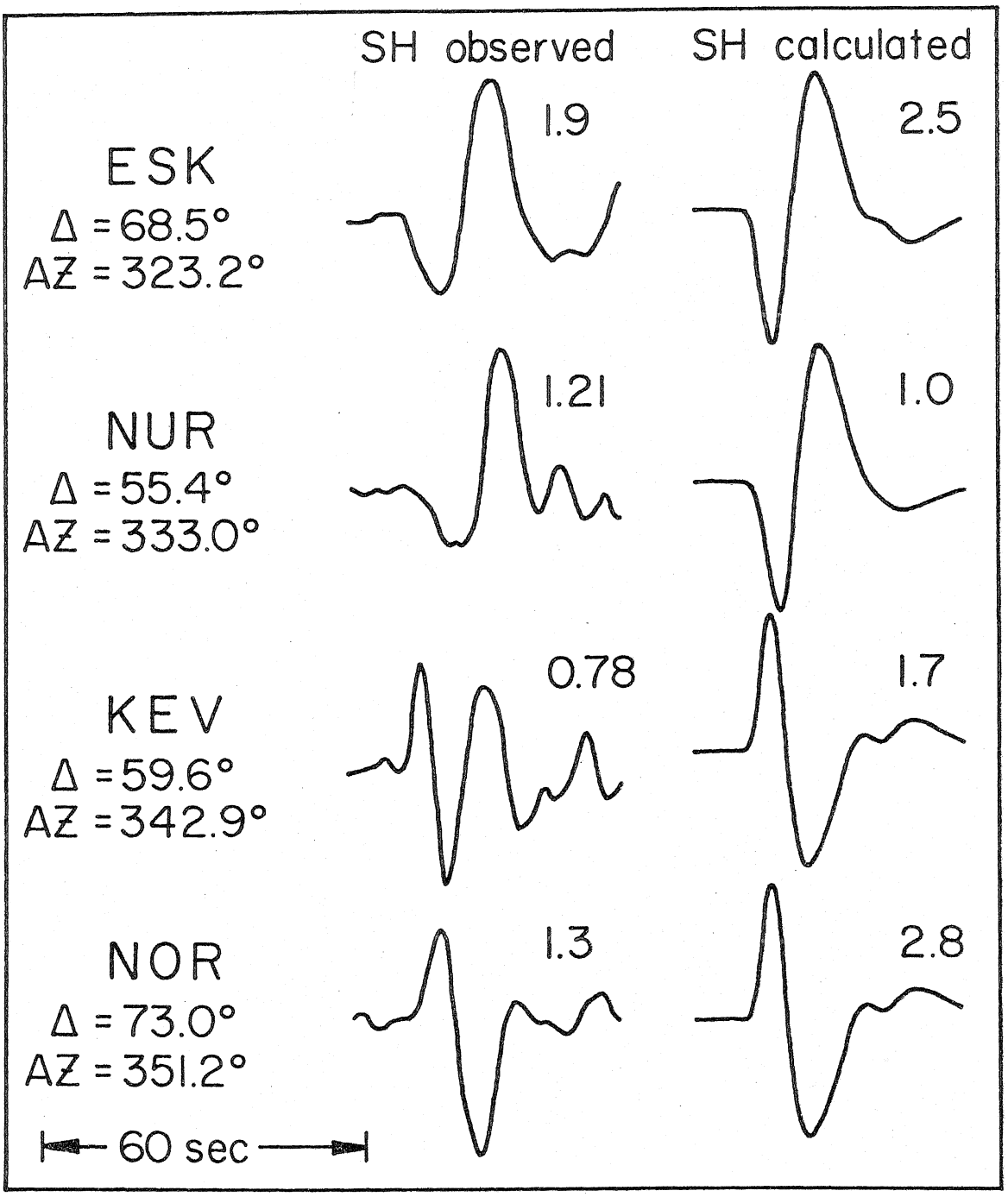

Figure 2.9. Qualitative fit for rotated SH waves near an SH node. The right side contains the predicted waveforms and the left the observed.

TABLE 2.4

MOMENT CALCULATION

STATION (P)	MOMENT (X 10^{26} dyne-cm)	STATION (SH)	MOMENT (X 10^{26} dyne-cm)
AAE	0.40	ADE	0.50
AQU	0.10	CTA	0.42
CTA	0.60	ESK	0.29
HKC	0.21	IST	0.31
IST	0.14	SHK	0.30
JER	0.24	VAL	0.37
KON	0.14		
MAT	0.25		
NAI	0.3		
PMG	0.6		
PRE	0.39		
SDB	0.3		
TAB	0.16		
average	0.29		0.37
$\bar{\sigma}$	0.16		0.08

more important in determining the solution of the inverse problem as opposed to values of $(Ru)_{ii}$ which are closer to zero. Figure 2.10 is a polar diagram of the stations used in the inversion plotted as a function of their azimuth and relative importance defined by equation (2.2). Total importance, or in this case Tr Ru = 6, has been normalized to unit amplitude and the relative importance of each station taken as a percentage. The distribution observed in Figure 2.10 is a product of several factors. Assuming that statistical noise is equal for each station, the higher values of importance partially means that the station produced large partial derivatives because parameters were changing quickly in the model space. Thus, these stations were very important in the real sense of producing a better model. However, since a true parameterization of the seismic event which can explain every datum perfectly is most likely impossible, a high importance can also reflect model deficiencies. If Figures 2.5 and 2.10 are compared it seems that the latter reason is the predominant one. Good fits have low importances and bad fits have high importances, in general, implying that the model is deficient in its assumptions on this level.

Since this is an overdetermined problem, standard techniques can be used to study the errors induced by the observations onto the model space.

Examining the "error" matrix of the system (for example, see Minster et al., 1974, and Alewine, 1974) and finding the 95% confidence

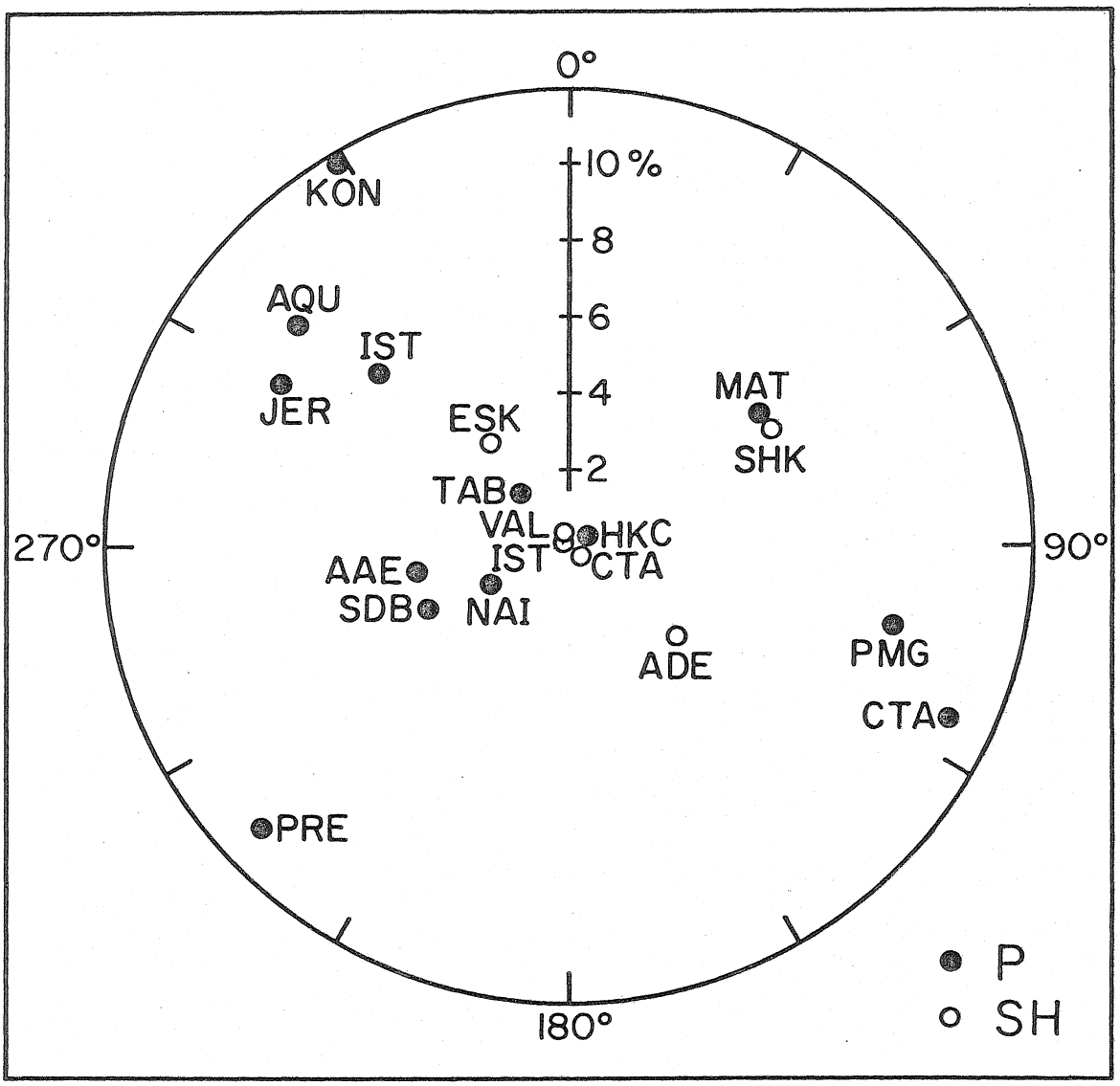

Figure 2.10. Data importance plotted as a function of azimuth on a polar diagram.

ellipses for pairs of parameters using a standard error which implies that the best fit cannot exceed .99 (Mellman and Burdick personal communication, 1975) gives the expected result of very small errors. Assuming the maximum excursions of the 2-D error ellipses to be some indication of error, the depth is precise to 200 meters, dip 1°, strike and rake 2°, δt_1 0.3 sec, and δt_2 0.4 sec. Needless to say these errors are only apparent and not a true indication of the deficiency of the model. The two dimensional error ellipsoids represent cuts through the 6-D surface and may not be an indication of maximum attainable excursions. If the principal axes of the error ellipsoid are examined, however, the same story is repeated with the exception of δt_2, which attains a maximum excursion of 0.8 sec.

To get some idea of the real deficiencies in the model another inversion was run with a different crustal model, crust no. 3 of Table 2.2. The last entry of Table 2.3 shows the results. Changing the P-velocity of the source layer primarily changed the take-off angles and is reflected in the changes in fault orientation. This model gave virtually the same overall fit. In detail, however, some stations such as PMG and CTA, were substantially degraded, e.g., first motions reversed, although others were improved. This model cannot be ruled out even though it is not preferred. It will be used, however, as an estimate for the variation in orientation angles, which taken in conjunction with the error ellipses, give extremal values

for the errors in θ, δ, and λ as about $\pm 6°$.

The comparison of short period observations with long period observations at the same station proved interesting for estimating the uncertainties in the source time function. Figure 2.11 shows the representative long period-short period comparison of the P wave data set. One of the most striking effects observed is the discrepancy in apparent travel times between the long and short period records. Consistently, at those stations which have low noise characteristics, the short period first arrival is about one second before the apparent long period arrival. This is certainly compelling evidence for a small foreshock before the main event. Gupta et al. (1971) make a case for such an effect from interpretations of short period teleseismic and local observations. They interpret a small arrival before the main burst of energy as the foreshock. In detail, however, the story is much more complicated. Assuming this foreshock occurred in the same general area and is of similar orientation as the main shock it will be subject to the same earth response as the main shock. That is, the amplitude and travel time of the major phases will be subject to the source orientation and depth. The bottom half of Figure 2.11 illustrates the results of a modelling experiment which attempted to reproduce the major effects of the short period records. The time function used was that of Figure 2.12 which contains a small triangular precursor and minor modifications of the simple triangular pulse, which were needed to enhance the high frequency nature of the short period

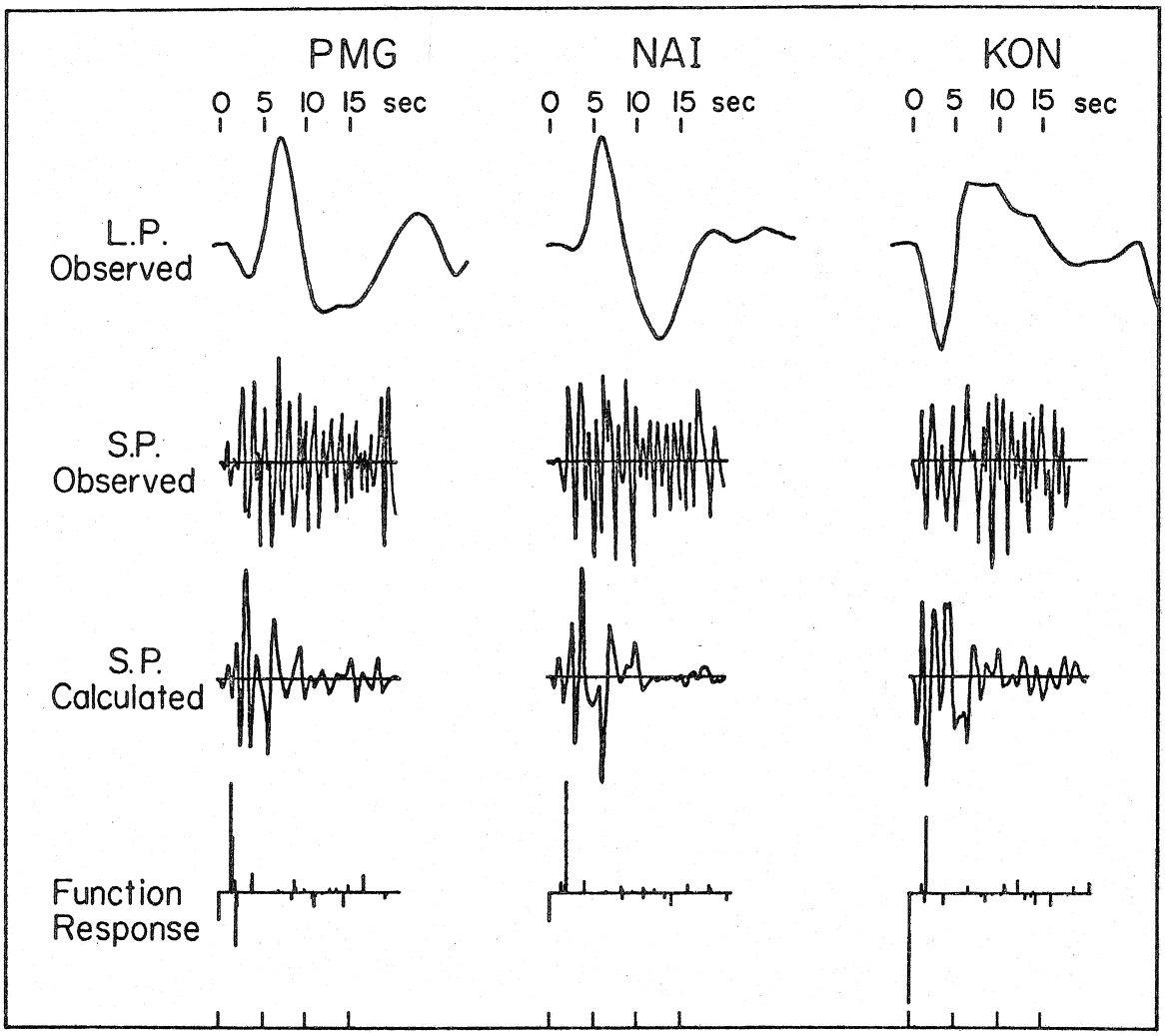

Figure 2.11. Comparison of representative long period and short period records at three stations. Shown below are synthetic short period records and the crustal delta function response used. Each record is aligned with respect to zero time.

records. The convolution of the short period instrument, convolved with the Q filter, with this pulse is a complicated looking time series due to the sensitivity of the short period instrument to slope changes. Convolving this with the earth response, as shown in the bottom half of Figure 2.11, produces synthetics which resemble the observations. At PMG and NAI there is a small amplitude arrival about two seconds before a larger arrival. At KON the P wave is more impulsive in behavior without the two second precursor. The significant aspect of this exercise is that the precursor arrival is not just the foreshock but also contains the main shock. The larger second arrival is composed of the reflected phases from the free surface. Because the short period instrument is sensitive to very short time scale effects there is an apparent lag in travel time as the long period instrument reacts to the major long period nature of the displacement pulse. As shown in Figure 2.12 this gives rise to slow build-ups to the P arrival. In fact, this is a very common characteristics of the Koyna observations.

Figure 2.11 also demonstrates the extreme interaction between the direct wave and surface reflections through the comparison of the delta function responses and long period waveforms. Assuming that the phase interpretaions made for the short period records are correct, the estimated error in depth for the hypocenter is about ± 1.5 km, still very small but larger than that estimated by the error ellipsoids.

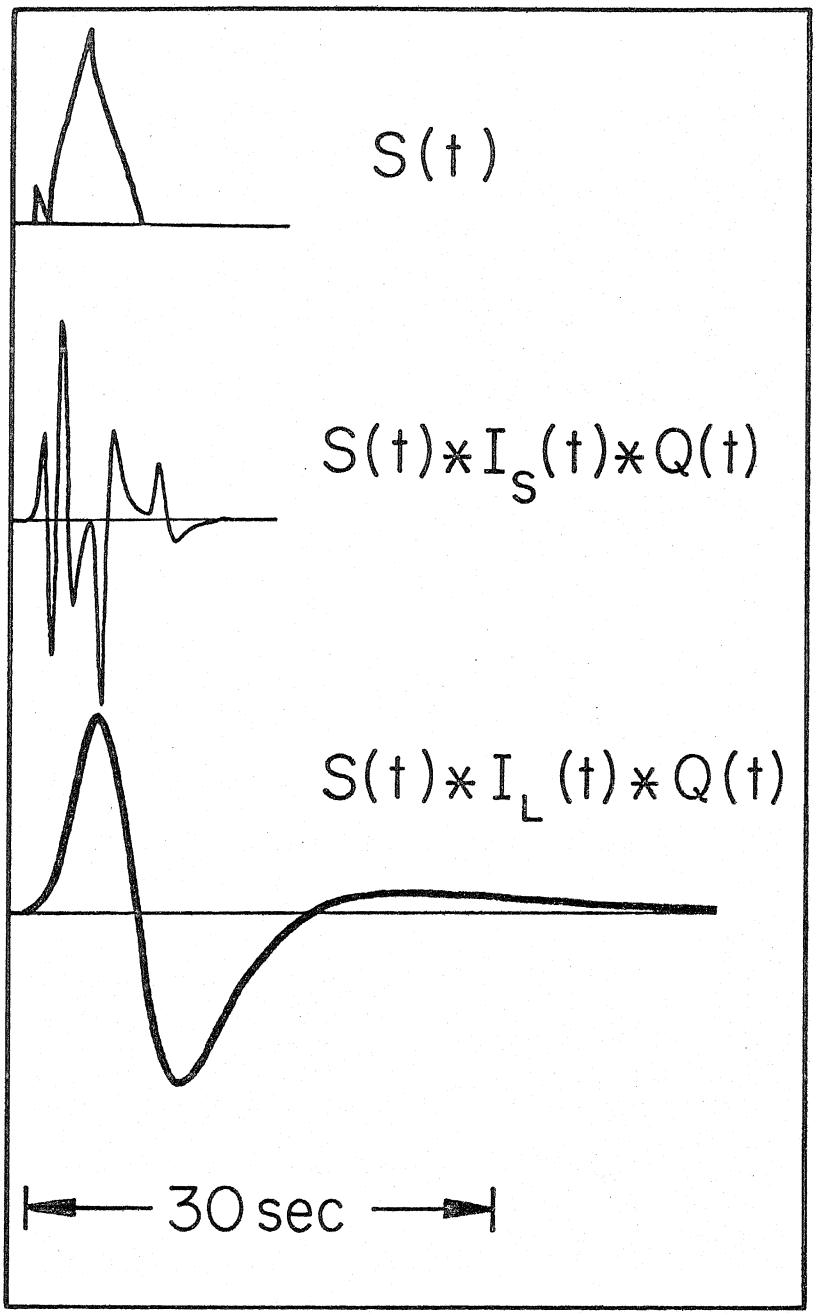

Figure 2.12. Final inferred time function with the comparison of the short and long period instrument responses.

This agreement between the short and long period depth determinations also brings up an important but subtle point. The model is a simple point dislocation with no finiteness. Since no finiteness effects are apparently resolvable although they may be possible the depth agreements imply that, at least teleseismically, the Koyna source radiation behaved as if coming largely from one localized spot. The simple dislocation model seems justified on this basis.

The major inadequacy in the short period modelling is the lack of signal duration after the initial arrivals. Reasons for this are bountiful such as fine source crustal structure, complicated receiver structure, and more source time function effects. The preferred speculation is that earth structure, both at a source and receiver, is responsible. Using the Koyna Dam accelerograms one can estimate a maximum limit for source duration, assuming that these recordings represent all the major source processes. Figure 2.13 shows the three components which were situated at about 10 to 20 km distance from any of the epicenters obtained. Interpreting the low amplitude first arrival as the P wave, which triggered the instrument, and the larger second arrival as the S wave, a maximum source duration of about 8 seconds is obtained using the length of the S wavetrain. This is maximum because any structural effect such as reflections and refractions will tend to lengthen the record. This P and S interpretation is based primarily on the short period WWSSN records.

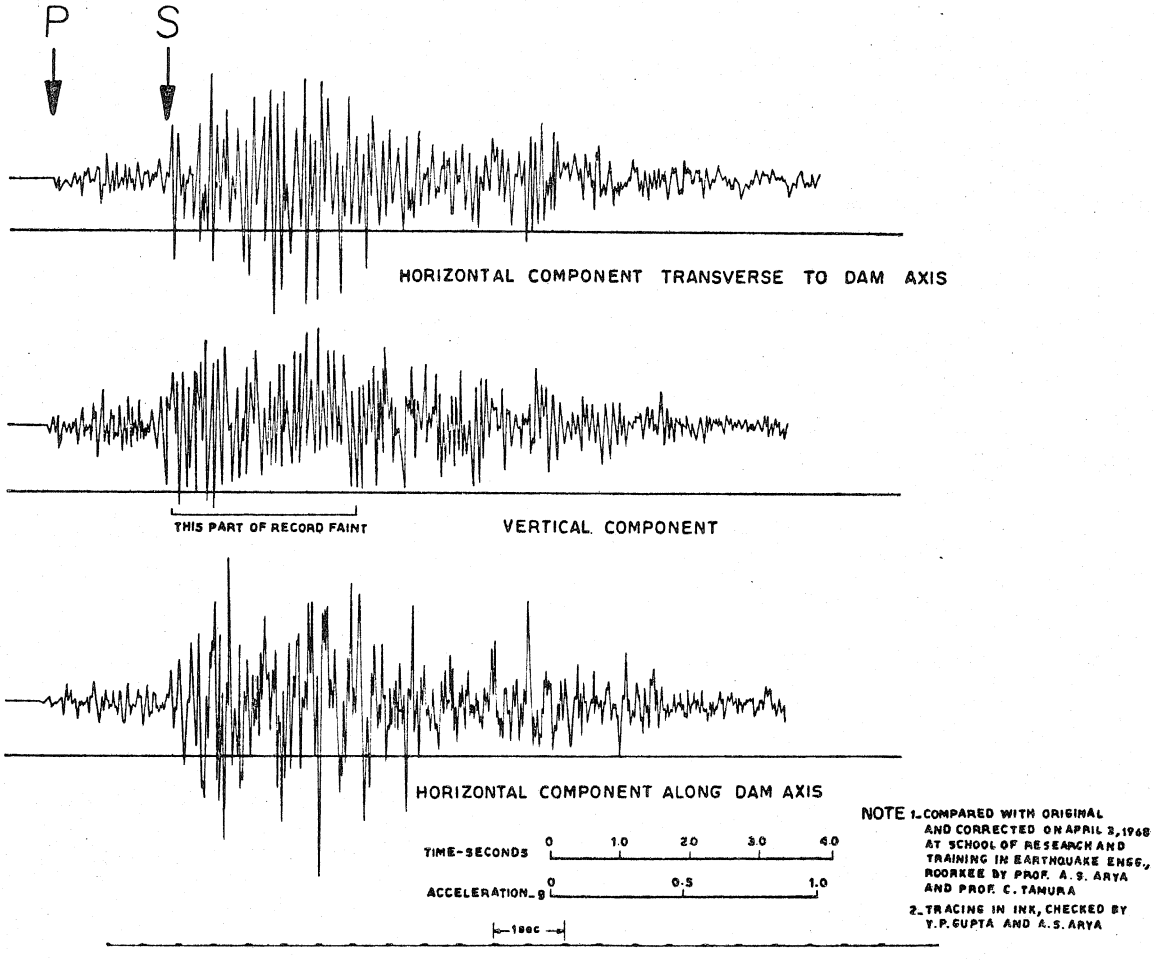

Figure 2.13. Koyna accelerograms (after Krishna et al., 1969).

If indeed the foreshock and main shock have similar short period characteristics then they should not be as distinct as Gupta et al. (1971) suggest in their multiple source interpretation of these accelerograms. These authors assume the first arrival to be entirely a foreshock and the phase here picked as S, the main shock. Their interpretation is also based on the teleseismic short period observations, however, they picked the phases,as interpreted here, P and pP as seen from their Figure 3. At any rate, if all direct source effects are over within eight seconds then all other arrivals after eight seconds must come from scattering, either from coherent structural effects or random scattering. This maximum time duration of eight seconds agrees very well with the estimate made from the inversion of about 6.5 sec.

There may be some basis for more high frequency source complications in the first eight seconds of the short period records. A prominent third arrival, modelled here as a sharp peak on the triangular time function (Figures 2.11 and 2.12) occurs in many short period records. However, there is not enough consistency between the records to accurately pick an arrival time in order to do a relative location study. The phases aren't coherent and often first arrivals are emergent rendering any interpretations suggestive at best.

Recently, Singh et al. (1975) have examined the Rayleigh wave excitation from the Koyna earthquake and coupled with S-polarization angles determined that the source mechanism is close to that of Sykes (1970), Figure 2.2a. They obtained a strike of N 10° E,

dip 78° W, and rake of 175° for a 10 km deep source. Since the source is very shallow, polarization angles cannot strictly be used unless the effects of the source crust, e.g., sS, are adequately compensated for. To determine if their Rayleigh wave data are consistent with the focal mechanism obtained here, a search through the model space based on the amplitude data at T = 50 sec, their Table 5, was made. A least-squares procedure was set up to test all orientations between 60° sectors in the angles with a 4° increment. The radiation pattern was taken from Harkrider (1970) for a 10 km source depth. This procedure yielded the result that the focal mechanism presented here was a better fit to the 50 sec period Rayleigh wave data than the mechanism presented by Singh et al. (1975). However, the region of the model space examined contained two minimums which were qualitatively close to both orientations. Considering the scatter and inconsistencies in this spectral data any solution should be considered highly ambiguous.

Discussion

The probable reasons for the major inconsistencies in the various source mechanisms obtained for the Koyna earthquake are multiple. First, the earthquake was relatively small in moment and combined with the small precursor produced emergent arrivals. Add the usual low amplitude noise, first arrivals become obscure, if not impossible to read. Many of the direct wave polarities deduced in this study are plainly contradictory to other studies. For example, the stations

which control the direction of fault dip, assuming the strike is correct, PMG, CTA, ADE, and MUN are dilatation here but were picked compression by Gupta et al. (1971). The particular fault orientation and depth also helped in this process. At many stations the orientation produced large surface reflections with very small direct arrivals making it difficult to interpret just what the first arrival represented. The strength of the method outlined here is that it minimizes these difficulties by using the wealth of relative time and amplitude information contained in the whole waveform. If the source is relatively simple, both the P and S radiation fields are used to constrain the solution, incorporating those observations which have the highest quality rather than using a large quantity of less reliable first motion data.

The question of just what fault caused the Koyna earthquake and where it is located seems to be unresolved. One school of thought (Gorbunova et al., 1970; Tsai and Aki, 1971), infers that the Koyna fault is very deep, 55-80 km, yet extends to the surface to produce the high intensities observed. The duration, size, and crustal phase content of the body wave pulses clearly rejects this hypothesis and is consistent with the other school of having a shallow source (Gupta et al., 1969, 1970; Dutta, 1969). The orientation question has been addressed and implies there is a major left-lateral strike-slip fault with some dip-slip component near the Koyna Dam. The most logical place to put this fault would be at the area of maximum intensity and observed ground breakage.

Several lines of evidence suggest this interpretation. First, the orientation of the focal mechanism agrees very favorably with the strike and left-lateral en echelon character of observed fissures in the meizoseismal area. If the average S-P time from the Koyna accelerograms is taken with the depth determination, values of 10 to 14 km are obtained for the epicentral distance assuming various plausible crustal models. This puts the epicenter, Figure 14, slightly to the east of the trace of the fissures, assuming that the IMD epicenter indicates the general direction away from the dam. This eastward shift also supports the direction of dip obtained if indeed the surface fissures are the direct manifestation of a buried fault. The intensity data (Guha et al., 1970), are also consistent with this model where the contours in Figure 2.14 have been drawn with respect to Guha's Figure 21. Some independent evidence for a major fault along this trend comes from anomalies in the correlation of erosion surfaces (Snow, personal communication, 1975), although some gravity work done near the fissures south of the Koyna River show no significant gravity anomalies (Kailasam and Murthy, 1969).

On a more general level the inversion of this shallow earthquake has some far-reaching implications for currently used procedures. The radical structural interaction caused by the various boundaries in the crust coupled with the radiation pattern of the source absolutely precludes the use of simple wholespace models for interpretations involving shallow sources unless the depth and time function are sufficient to keep these effects well separated

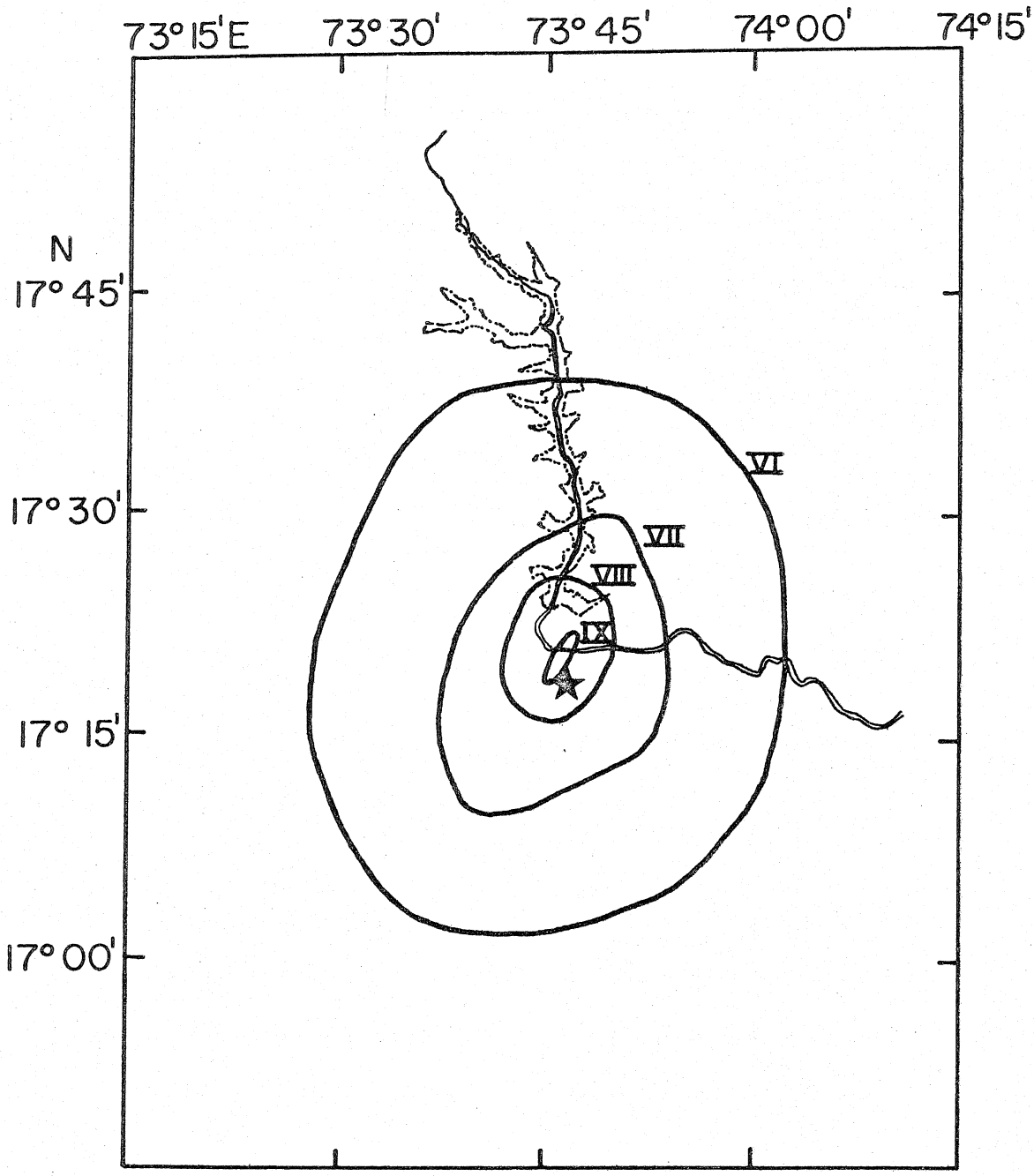

Figure 2.14. Isoseismals based after Guha et al. (1970), Figure 21, showing the inferred location of the Koyna epicenter as a star.

from the actual direct arrivals. Using the whole body waveform instead of being limited by a sometimes ambiguous first motion pick is far superior in constraining a focal mechanism since it incorporates much more information by using both the P and S radiation patterns. Although first motion studies are obviously still useful and easy to do they can be supplemented by waveform interpretations when a shock has poor station coverage. An added advantage is that an independent depth determination can be made when the surface reflections are identified.

Conclusions

The use of point dislocations in a layered halfspace coupled to a formal generalized inverse proved to be a very useful tool in determining the focal parameters of the Koyna earthquake. The parameters obtained using 13 P and 6 SH waveforms were: dip 67° to the east, strike N 16° E, rake -29° plunging northeast, all angles ± 6°; depth 4.4 ± 1.5 km; δt_1, 2.5 ± 0.5 sec, δt_2 3.9 ± 1.0 sec for a triangular time pulse; and moment 3.2 ± 1.4 x 10^{25} dyne cm.

Approximately the first 25 seconds of the long period P and SH waveforms could be explained, within the uncertainties of the crustal model, by a simple point dislocation in a two layered crust. The P wave signature is almost entirely controlled by local crustal reflections and phase conversions although the SH waves are visibly affected much less by the structure. The radical interference effects

caused by the coupling of source radiation and crustal boundaries severely encroaches on the applicability of interpretive methods which assume a homogeneous wholespace.

The short period P waves could only be modelled approximately but indicate that crustal structure can explain the relative times and amplitudes of the first major arrivals. Probable short period source effects include a small precursor event which occurred approximately one second before the main shock. Possible later arrivals up to a maximum of eight seconds after the first arrival may be other source effects but there is ambiguity in this type of interpretation caused by uncertainty in the source crustal structure.

Interpreting arrivals on the Koyna accelerograms as P and S waves an estimate of eight seconds is made for maximum source duration. This agrees very well with the estimate of 6.5 seconds made from the body wave inversion. The shallow depth determination, isoseismal evidence, and body wave fits preclude the interpretation that the Koyna source was deep seated and demonstrate that it was indeed a very shallow earthquake. An argument can be made using the accelerogram S-P time, depth, and location of isoseismals that the epicenter lay a few kilometers southeast of the fissuring and the fissures in the meizoseismal area are the surface expression of the Koyna fault.

The methods outlined here should prove useful in other focal mechanism problems involving small complications in the body waves which obscure first motions yet leave the major portion of source information preserved in the general waveshapes.

Chapter 3

THE APRIL 29, 1965, PUGET SOUND EARTHQUAKE AND THE CRUSTAL AND UPPER MANTLE STRUCTURE OF WESTERN WASHINGTON AND OREGON

Introduction

The previous chapter dealt with the problem of trying to deduce source parameters from an extremely shallow earthquake. The interference of the direct waves and surface reflections was very severe due to the depth of the Koyna hypocenter. Some speculations were made to the origin of some of the reverberations after the reflections but these were hampered by both ignorance of the Koyna crustal structure and the interference with the major phases. If, however, an earthquake is deep enough so that the surface reflections and the direct wave are well separated, perhaps layer interfaces between the hypocenter and free surface can be resolved by intermediate reflected arrivals. It is exactly this supposition which will be used to explain the shape of long period P waves from the Puget Sound earthquake. A crust model for southern Puget Sound will be deduced by identifying arrivals between P and pP as underside reflections from crustal layers. A major compressional and shear wave low velocity zone (LVZ) in the uppermost mantle will be proposed by modelling the time, amplitude, and polarity of these reflected arrivals.

Simultaneously, care will be taken to model the source parameters as well.

The first half of this chapter will deal with modelling the Puget Sound earthquake and explaining some of the resultant anomalies observed in the data. The basic ray and matrix techniques of Chapter 1 will be used although no generalized inverse will be employed. The reasons for this are numerous. Once structure is recognized as being part of the inversion problem the model space expands hopelessly even though some definite conclusions can be made concerning some particular effects of earth structure. It is certainly possible to fold in structure parameters to the inversion formulation of Chapter 1, but the cost and trouble this entails would render any such attempt unfeasible at present. One of the biggest unknowns in this first attempt is the question of how well do the assumptions of plane layering and no lateral variations hold? On the basis of this earthquake study and some geological considerations it will be concluded that this assumption is not completely justifiable. Therefore, the modelling will be limited to hypothesis testing using the well-worn seismological method, trial-and-error.

The last half of the chapter will concentrate on making the inferred Puget Sound crustal model more feasible by investigating the earth structure under a WWSSN station at Corvallis, Oregon. By looking at PS and SP conversions and P reverberations using deep teleseismic earthquake sources, a similar distinct LVZ is again inferred.

The agreement between these two independent sets of data makes a strong case for the existence of this unusual structure. A few of the regional geophysical anomalies will be discussed in this light.

Geologic and Tectonic Setting

Puget Sound is located in northwestern Washington and is part of a major north-south geologic and physiographic province, the Puget-Willamette depression (Figure 1)(Snavely and Wagner, 1963). This province is bounded on the west by the Oregon-Washington Coast Ranges and is most pronounced next to the transverse, northwest trending Olympic Mountains. To the east are the volcanic Cascades which extend from the Canadian border into Northern California. To the north are the Straits of Georgia forming the boundary of the Canadian Insular and Coast Crystalline Belts (Roddick, 1966; Brown, 1966) and are a physiographic extension of the Puget lowlands. Bounding the province in the south are the Paleozoic and Mesozoic Klamath Mountains which extend into Northern California.

The geologic development of this area has been controlled by Tertiary sedimentation and volcanism in a north-south trending eugeosyncline shown in Figure 3.1 (Snavely and Wagner, 1963; Snavely et al., 1968). Throughout the Tertiary, the area has been characterized by a north-south linear belt of basaltic volcanic islands with concomitant clastic and pyroclastic marine and non-marine deposition. A net eastward migration of this chain occurred during the Tertiary. Synchronously, to the east, andesitic

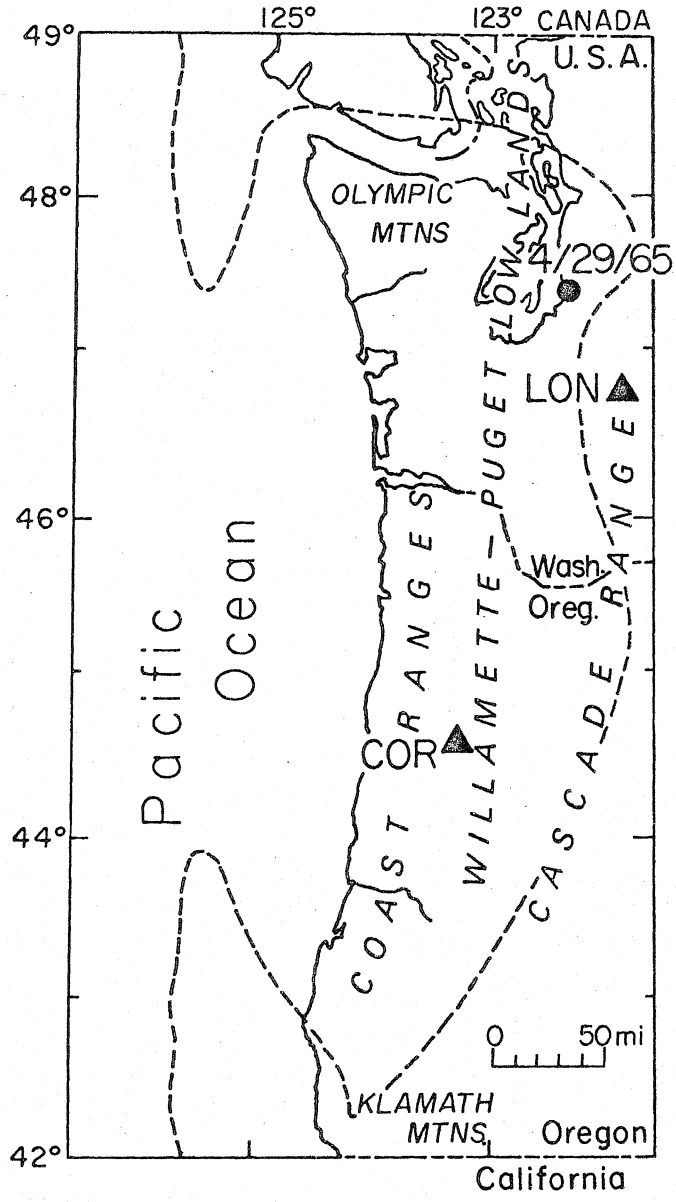

Figure 3.1. Index map of western Washington and Oregon showing the epicenter of the 1965 Puget Sound event and WWSSN stations used in the receiver structure determination. The dashed line is the approximate extent of the Tertiary eugeosyncline, after Snavely and Wagner (1963).

vulcanism at the locus of the present-day Cascades was taking place.

The major structural features of the area started to form during late Miocene with uplift of the Coast Ranges and Olympic Mountains. These ranges probably attained their maximum height in late Pliocene time. Puget Sound remained a low area with marine deposition. Subsequent glacial stages during the Pleistocene have modified the topography and mantled most of the Puget Sound lowlands with extensive sheets of glacial till limiting surface geologic mapping of this area (Huntting et al., 1961).

The principal deformational style in the Coast Ranges consists of wide, open folds trending mostly north to northeast with minor faulting (Wells and Peck,1961). The Olympics, however, consist of a broad anticlinorum of competent, thickly bedded Eocene volcanics surrounding a highly deformed and partially metamorphosed core of probable pre-Tertiary sediments (Cady and Tabor, 1964). A broad north-south trending crustal downwarp filled with extensive alkalic volcanics and pyroclastics comprises the Cascade Range in Northern Oregon (Peck et al., 1964). The Puget-Willamette depression may be fault controlled with major faults occurring on the eastern margin of Puget Sound and the western side of the Willamette Valley (Algermissen and Harding, 1965; Bromery and Snavely, 1964).

The continental shelf off southern Oregon and northernmost California is roughly 50 km wide and characterized by several wide

plateaus with narrow slopes between (Silver, 1971a). Deformation increases westward away from the coast, from broad gently folded basins to highly deformed piercement structures bounded by high angle dip-slip faults. The continental shelf off the Washington coast is similar in style although it is about 80 km wider (Silver, 1972).

Seismic refraction studies have been confined mostly to offshore areas. Shor et al. (1968) and Dehlinger et al. (1968) describe crust and upper mantle models derived from refraction and gravity interpretations for the area including the Gorda-Juan de Fuca rises and Gorda and Cascadia basins to the east. They infer anomalously low upper mantle velocities under the Gorda and Juan de Fuca ridges with normal oceanic velocities and crustal thicknesses in the basins. Of the profiles which have been made on land, perhaps the most significant is the one by Berg et al. (1966). They obtain a very thin (16 km) crust and a Pn velocity of 8.0 km/sec for the Coast Ranges of Oregon and southern Washington. Because of the conspicuous lack of pre-Tertiary granitic basement within the margins of the Tertiary eugeosyncline (Figure 3.1) and from the velocity and thickness values obtained in this refraction profile some authors have suggested that the area is a large embayment of oceanic crust in the North American continent (Hamilton and Myers, 1966; Dickinson, 1970). Tatal and Tuve (1955), who did some of the first crustal refraction studies in the Pacific northwest, reached a similar conclusion for

the southern Puget Sound area. They obtained a crustal thickness of about 19 km and Pn velocities of 8.0 km/sec. However, further north at Vancouver Island, White and Savage (1965) obtained crustal thicknesses approaching 50 km with no well developed Pn phase observed. Other less well controlled refraction lines have extended into the area (Johnson and Couch, 1970) but are of little use because of their uncertainties. Dehlinger et al. (1965) constructed travel-time curves from local earthquakes for the Washington-Oregon area and concluded that Pn velocities were significantly lower, 7.8 compared to 8.0 km/sec, west of the Cascades than to the east. McCollom and Crosson (1975) reached a similar conclusion by estimating Pn velocities using the Puget Sound and Hanford seismic arrays.

Gravity and magnetic measurements and interpretations have been more extensive than seismic studies. In particular, Thiruvathukal et al. (1970) studied the regional gravity of Oregon concluding that crustal thicknesses near the coast are relatively thin, on the order of 20 km, compared to a 45 km thickness near the center of the state. Bromerly and Snavely (1964) did reconnaissance surveys of gravity and magnetics for northwestern Oregon and have correlated positive gravity anomalies and high gradient magnetic anomalies with extensive outcrops of Eocene volcanics. Further to the north in the Puget Sound-Olympic region a similar conclusion was reached by Stuart (1961) where he modelled the gravity field induced by the massive Eocene Crescent volcanics ringing the Olympic mountains. The work of

Daneš et al. (1965) is of direct importance to this chapter. Through detailed gravity and magnetic modelling these authors deduced some of the major structures of southern Puget Sound. Their principal results include the discovery of a large northwest trending igneous horst structure with flanking deep sedimentary basins. They infer sediment thicknesses of 4 km and 10 km for the southern Tacoma basin and northern Seattle basin, respectively. The large observed gravity gradients suggest major faults bounding this horst with inferred throws on the order of several kilometers. It may be significant that the April 1965 event occurred under the eastern edge of this structure. Daneš (1969) has also suggested that Puget Sound is a great isostatic depression with an isostatic anomaly greater than -100 mgal.

Heat flow measurements (Blackwell, 1974) although few, indicate relatively low heat flow (~0.8 HFU) near the coast of western Washington with higher values in the volcanic plateaus to the east.

The theory of plate tectonics forms the basis for current thinking on the tectonic framework of the Pacific Northwest. Interpretation of the magnetic anomalies of Raff and Mason (1961) by Vine and Wilson (1965), Wilson (1965), and Vine (1966) and other subsequent work by Tobin and Sykes (1968), Atwater (1970), Dickenson (1970), Silver (1971a, 1971b, 1972), Crosson (1972), and Chandra (1974), among others, have led to a hypothesis relating the geophysical and geologic data into one plate tectonic scheme. The model states that subduction of

oceanic crust and upper mantle is taking place north of Cape Mendocino to Vancouver Island. A small offshore ridge system, the Gorda-Juan de Fuca rise, is still producing oceanic lithosphere which is the remnant of the previously more extensive Farallon plate (Atwater, 1970). Spreading at a half-rate of about 2.5 cm/year, this small plate may still be underthrusting the continent as the association of andesitic vulcanism in the Cascades seems to require (Dickenson, 1970) and as inferred from offshore geologic evidence (Silver, 1971a,1972). Against the normal assumptions of plate tectonics, this small plate does not appear to be rigid, but seems to be experiencing internal deformation (Silver,1971b; Crosson, 1972).

Perhaps the most serious problem with this scheme is the conspicuous absence of a seismic Benioff zone. The general seismicity level of the area is low other than at the offshore fracture zones (Tobin and Sykes, 1968; Chandra, 1974). Puget Sound has a moderate background of diffuse seismicity, however, and a few events have occurred at depths of up to 70 km (Crosson, 1972). The magnitude 6.5 Puget Sound earthquake of April 1965 was located at 60 km depth, see Figure 3.1 (Algermissen and Harding, 1965), and the somewhat larger April 1949 event, at 70 km (Nuttli, 1952). Although these events are not extremely deep for other island and continental arcs, they are very unusual compared to all other continental U. S. earthquakes. Because of this, they have been cited as evidence for

a remnant of a subducting plate, or perhaps, a very slowly subducting plate under Washington (Isacks and Molnar, 1971; Crosson, 1972). Other geophysical evidence supporting this plate model comes from travel time anomalies determined from P residuals for the 1965 event (McKenzie and Julian, 1971) and from an array processing study using teleseismic P arrivals at Puget Sound (Lin, 1974). Both of these studies reach the similar conclusion that a high wave velocity plate dips to the east with an angle of about 50 degrees.

The unusual depth of the April 1965 event and the interesting geologic and geophysical problems this area presents motivates the detailed waveform study that this chapter reports. The original purpose of this study was to find a detailed source model for the earthquake, but as it turned out, much more interesting information could be found by modelling the local source structure as well.

The Puget Sound Earthquake

On April 29, 1965, at 15:28:44 GMT a magnitude 6.5 earthquake shook the environs of southern Puget Sound causing moderate damage in Seattle and Tacoma (see Figure 3.1). The location of the epicenter was midway between these two cities and the hypocentral depth and estimated to be at 60 km (Algermissen and Harding, 1965). Consistent focal mechanisms for the event done by several authors show predominantly normal dip-slip movement on a 70° eastward dipping plane striking approximately 15° west of north

(Algermissen and Harding, 1965; Isacks and Molnar, 1971; Chandra, 1974). The auxiliary plane is only poorly constrained because of sparse local station coverage, a common occurrence for this type of orientation. Because of excellent teleseismic coverage, however, the first nodal plane is extremely well determined and serves as a very useful constraint in the waveform modelling.

Data and Data Processing

The gathering and processing of long period P and SH waveforms were done as described in Chapter 2. A small change in procedure which lightened this preliminary work considerably was in the digitizing. Rather than averaging four digitized traces only two were used. The reduction in accuracy is insignificant for most uses and was far outweighed by the savings in time and trouble. Table 3.1 lists the WWSSN stations utilized for this study. Unfortunately, there was only one station in which the horizontal components were naturally rotated with respect to the ray direction. As a result, only a few SH waveforms could be salvaged for waveshape analysis and even these may be contaminated by the rotation process.

Most of the stations in Table 3.1 were equipped with the longer period 30-100 instrument instead of the 15-100 instrument used in the Koyna study. A few stations, ANT, QUI, SJG, and BEC had just been changed to the standard 15-100 instrument, however, so these

Table 3.1

Station Information

Station	Δ(0)	AZ(0)	BAZ(0)	Components
AFI	75.3	229.7	32.3	P, p(d)
AKU	53.2	30.1	304.7	p(b)
ANP	87.8	305.5	37.6	P
ANT	84.8	133.6	327.5	P, p(d)
ARE	78.2	130.5	327.5	s
ATL	31.8	102.2	307.4	P, p(a)
ATU	89.8	26.2	337.7	P, p(d)
BEC	45.7	87.6	306.7	P, p(b)
CAR	59.2	109.5	319.4	P, p(b), s
COP	70.5	25.3	329.2	P, S
ESK	65.6	33.3	319.3	p(c)
GDH	39.4	31.6	272.9	P, p(a), S
GEO	33.7	87.8	299.5	P, p(a)
GIE	55.5	140.0	334.1	p(b)
GUA	82.0	281.2	43.3	P
HNR	88.7	254.7	41.6	P, p(d)
IST	88.3	21.3	340.9	P, p(d)
KEV	61.0	11.7	336.6	P, p(c)
KON	66.3	24.4	326.5	P
KTG	49.5	25.9	298.4	P, p(b), S
LPB	80.0	127.8	326.0	P, p(d), s

Table 3.1 (continued)

Station	$\Delta^{(0)}$	$AZ^{(0)}$	$BAZ^{(0)}$	Components
MAL	79.5	46.2	322.4	P
NNA	71.7	132.7	329.3	P, S
NOR	45.7	11.4	293.8	s
NUR	69.2	16.8	336.6	P, p(c), s
OGD	34.3	82.8	297.0	p(a)
PDA	67.4	58.6	313.0	P
PTO	74.1	46.0	319.7	P, p(c), S
QUI	60.8	127.5	327.4	P
SCP	32.2	85.2	296.9	P
SHA	31.0	110.2	312.3	P
SJG	54.1	102.8	315.8	P
STU	75.4	30.8	328.3	P, p(d)
TOL	77.2	44.0	322.1	P, s
TRN	62.6	104.7	318.1	P, p(c)
UME	65.3	17.3	332.9	p(c), s
VAL	65.3	39.2	316.1	p(c), S
WES	35.9	78.8	295.9	P, p(a)

P: long period vertical P waveform or first motion

p(a): short period vertical P waveform. Letter in parenthesis designates stacking group.

S: long period tangential S waveform

s: short period horizontal S waveforms used in stacking

were equalized to be consistent with the rest of the data set. An operator was constructed and convolved with these data to effectively make them 30-100 observations. The 30-100 instrument response was calculated using Hagiwara's (1958) formulation.

Data Inversion and Interpretation

As a starting point, it would be most convenient to present the final inferred earth and source models and P waveform fits. The complex interactions of the earth and source models will then be examined point by point and the reasoning behind each effect presented in a coherent manner.

Figure 3.2 displays the results of trial and error waveform modelling to find a source and earth model most consistent with the long period data. A standard first motion plot (bottom hemisphere) is given in the center of the diagram with the P nodal planes inferred from this study. In this determination, pP as well as P first motions were incorporated. Lines are drawn from each observed-synthetic waveform pair to the appropriate spot on the focal sphere which represents the downgoing P ray at that station. For each seismogram pair the observed is plotted above the synthetic. The source orientation parameters are given in the corner of Figure 3.2. In this model the source is assumed to be a single point dislocation

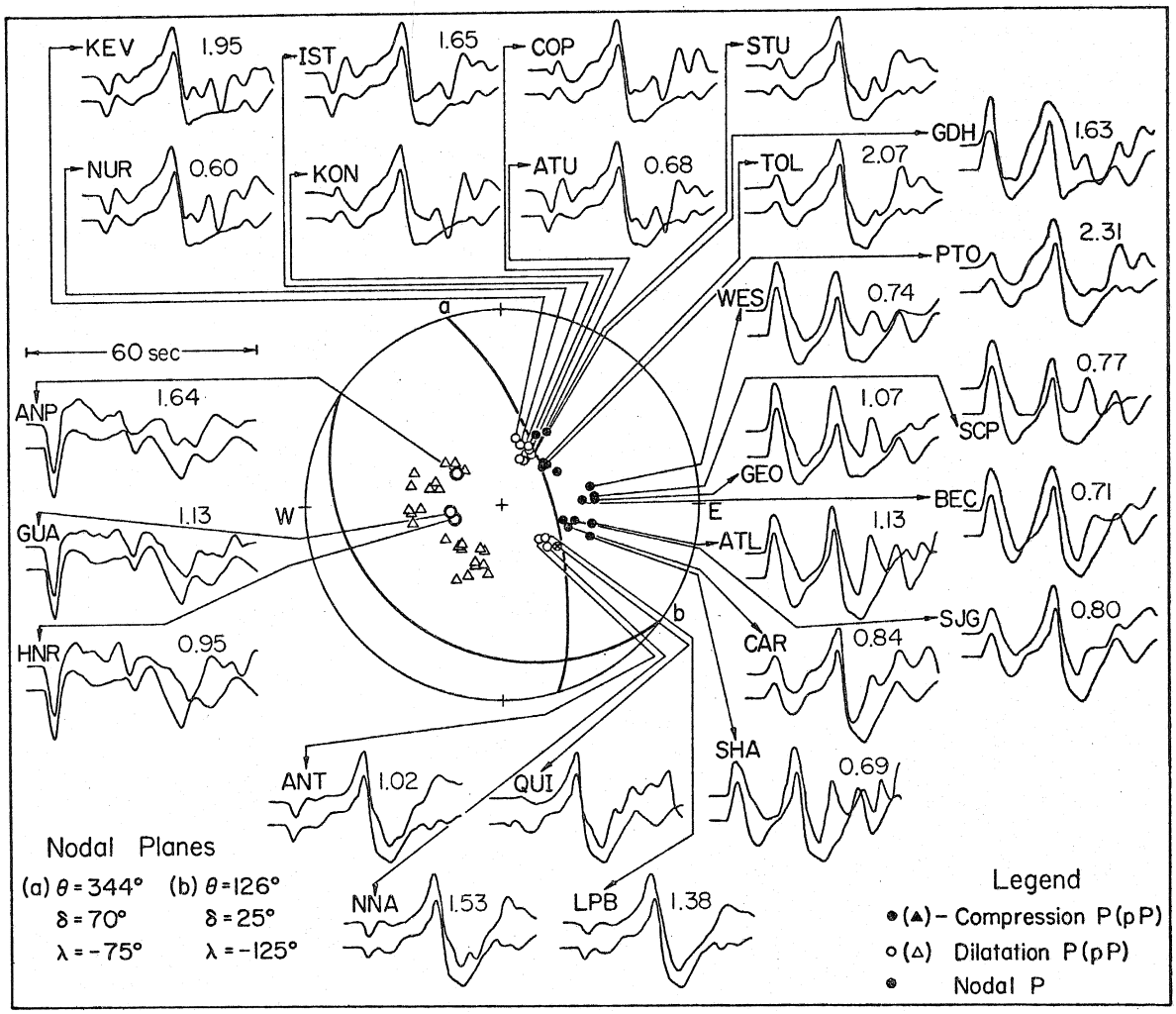

Figure 3.2. Comparison of synthetic and observed P waveforms for the final source and earth structure models. The observed is displayed directly above the synthetic at each station with the calculated moment indicated next to the traces (x 10^{26} dyne-cm). The focal plot is for the bottom hemisphere.

with a triangular time function characterized by a rise and fall-off time δt_1 and δt_2 equal to 0.5 and 2.5 sec, respectively. The final plane-layered earth model is presented in Figure 3.3 and is under the heading of 'PS-9' in Table 3.2. The source is situated at a depth of 63 km for this model.

Two striking features are apparent in Figures 3.2 and 3.3. The first is the quality of the waveform fits over the entire azimuth range. The observed waveforms have a tremendous variation in shape as a function of azimuth and take-off angle which the model approximates quite nicely for nearly all stations. Secondly, the earth model presented in Figure 3.3 is quite unusual. The major features of PS-9 include a very distinct and large low-velocity zone between 41 and 56 km depth. This structure is sandwiched between what appears to be mantle velocity material. The crustal section at the top is very thin, less than 15 km, and has very low velocity materials near the free surface. This model was inferred entirely from the long period P waves and will be discussed by closely examining which characteristics of the P waves control its various details.

Let us first look at what effects a simple earth model, a layer over a halfspace, gives for the long period P response. Figure 3.4 compares the simple one layer model (Table 3.2) with PS-9 for representative P waveforms. The major phases P, pP, and sP are quickly apparent in these waveform comparisons although there are significant differences in the interval between the direct P wave

Table 3.2

Structure Models

	Layer #	V_p	V_s	ρ	Th
1) PS-1	1	3.0	1.2	1.8	2.0
	2	4.0	2.0	2.0	2.0
	3	5.0	2.5	2.2	1.0
	4	6.0	3.0	2.3	1.0
	5	7.0	3.5	2.4	1.0
	6	7.8	4.0	3.2	28.0
	7	6.5	3.0	2.7	10.0
	8	5.5	2.7	2.6	10.0
	9	8.0	4.3	3.2	-
2) PS-9	1	2.0	1.0	2.5	1.2
	2	3.0	1.5	2.5	1.2
	3	4.5	2.3	2.5	2.5
	4	6.8	3.9	2.9	4.0
	5	7.4	4.2	3.0	4.5
	6	7.8	4.3	3.2	27.3
	7	6.5	3.1	2.9	7.0
	8	5.5	2.9	2.7	8.0
	9	8.0	4.6	3.2	-
3) Layer Over Halfspace	1	6.0	3.5	2.7	10.0
	2	8.0	4.6	3.2	-

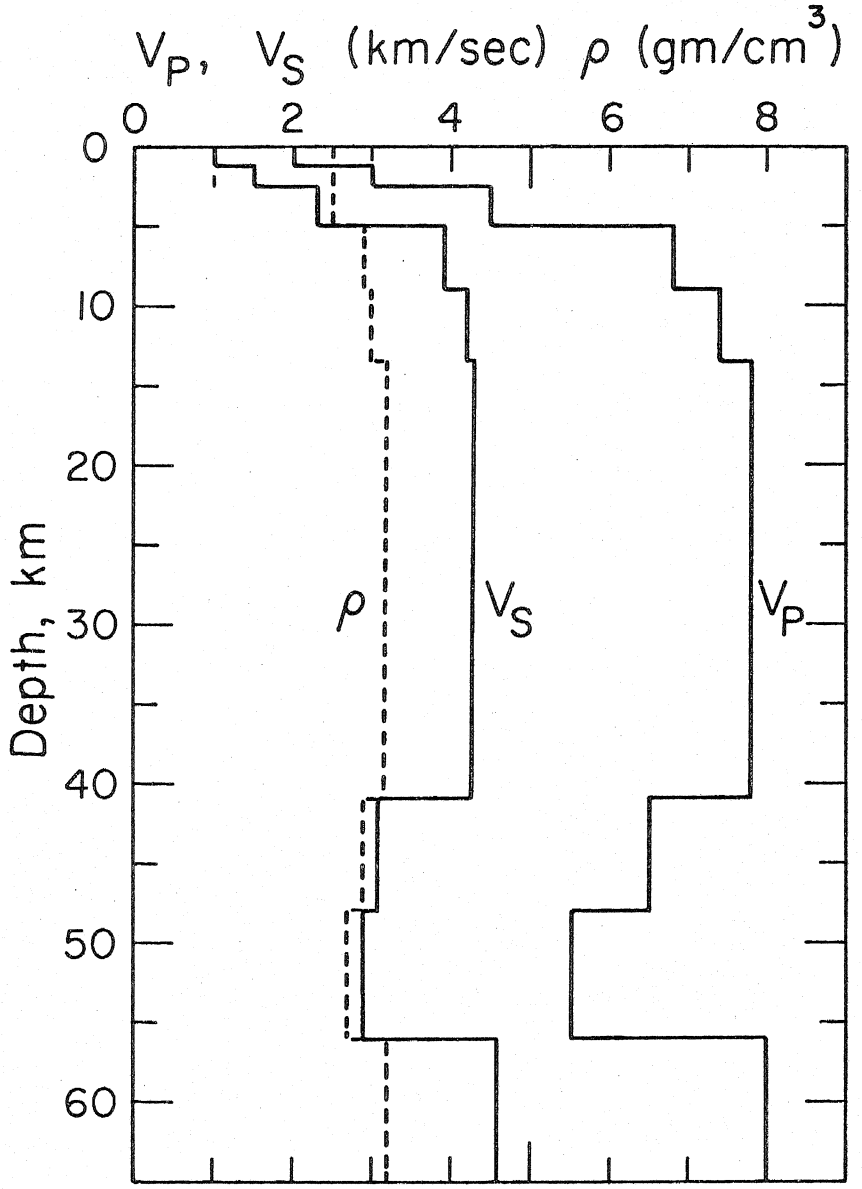

Figure 3.3. PS-9 earth model for Puget Sound.

and pP. The small arrival several seconds before pP in the one layer model is the P reflection from the bottom of the layer except at GUA where it is an S-P conversion at reflection. The first 18 sec of the P-wave for the simple model is just the convolution of the source time function with the Q operator (equation 1.15) and the instrument response since there are no distortions due to near source structure.

For COP and stations like it in the northeast (see Figure 3.2) the first 18 sec of the observed P wave show at least two arrivals after the dilatational direct P. First there is an equal sized compression, arrival A (Figure 3.4) approximately two seconds after P with another dilatational arrival, arrival B, 2 seconds after that. Examination of the one layer model of COP demonstrates that the overswing of the instrument response is not a factor here. At PTO the direct wave and arrival A have the same sign and add constructively because of the change in the P radiation pattern. This shows up as an increase in the P amplitude, relative to pP, at PTO and at other similar stations. Arrival B is plainly the same polarity as at COP. The interpretation of these arrivals is based on the assumption that they represent underside reflections from discontinuities above the source and not from source complications. It is entirely reasonable to assume that there are major discontinuities between a 60 km deep

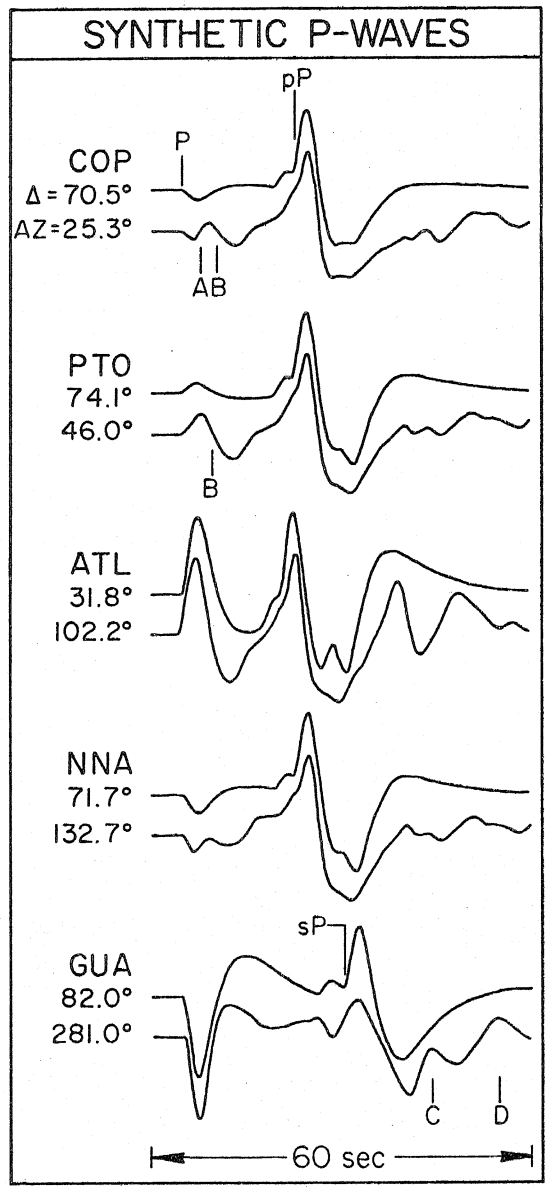

Figure 3.4. Comparison of P wave synthetic seismograms at five representative stations for the one layer model1 (top) and PS-9 (bottom). The phase identifications are referred to in the text.

source and the free surface,but it is obviously extremely hard to prove,unequivocally,that small arrivals are from such reflections and not source effects. The seismograms of Figure 3.2 suggest that these arrivals are associated with pP rather than the direct P wave by the observation that when direct P changes polarity the A and B arrivals remain constant.

Assuming that these arrivals came from reflectors above the source, what can be said about their properties? Since the strength of up-going P determines the amplitude of the reflection as well as the material contrasts, an approximate determination of the velocity contrast can immediately be made. At the northeastern P nodal stations upgoing SV radiation is at minimum because of fault orientation so that only P interactions can be considered. A cursory examination of the waveforms give a minimum amplitude estimate for reflection A of about 0.15. This is clearly an underestimate since interference with the direct wave knocks it down considerably. There must be interference since the width of the first swing changes as a function of P amplitude and azimuth. Compare STU and TOL, Figure 3.2, for example. The type of contrast can immediately be deduced because of the known polarity of pP. Since upgoing P is dilatational and the reflection is compressional, the reflection coefficient must be negative, which implies a higher to lower velocity contrast. Simultaneously modelling the time function, relative timing, and relative amplitudes of direct P and phase A for

the northeastern and southeastern stations yields the high contrast of 8.0 to 5.5 km/sec for the lowermost boundary of PS-9, Figure 3.3.

Continuing this line of reasoning one step further to phase B gives some remarkable results. Using the same process for finding the sign of the reflection coefficient, the polarity of B suggests that it comes from a lower to higher velocity contrast. Phase B, therefore, delimits the top of a low velocity zone. Figure 3.5 demonstrates this explicitly for the station KEV. Ray number one is normalized to unity and all other ray amplitudes referenced to it. The top of the LVZ was modelled with two interfaces in order to increase the width of the reflected pulse. This particular model explains the azimuthal variation of wave shapes for the first eighteen seconds remarkably well (Figure 3.2).

The uncertainty in orientation (see Figure 3.2) is not a major factor in the modelling. The P first motion data constrain the north-south nodal plane to within a degree. Since all of the stations are near the center of the plot and most are close to the nodal plane, relatively large variations in the rake (-90 ±20°) do little to affect the relative amplitudes of P and pP. Upgoing SV is more sensitive so there is some basis for assigning the particular value used, although it is a small effect and will be discussed later. The velocity assigned to the source layer is a value typically found for these depths in upper mantle studies. Variations in this velocity, of up to ± 0.5 km/sec, don't significantly affect the results since

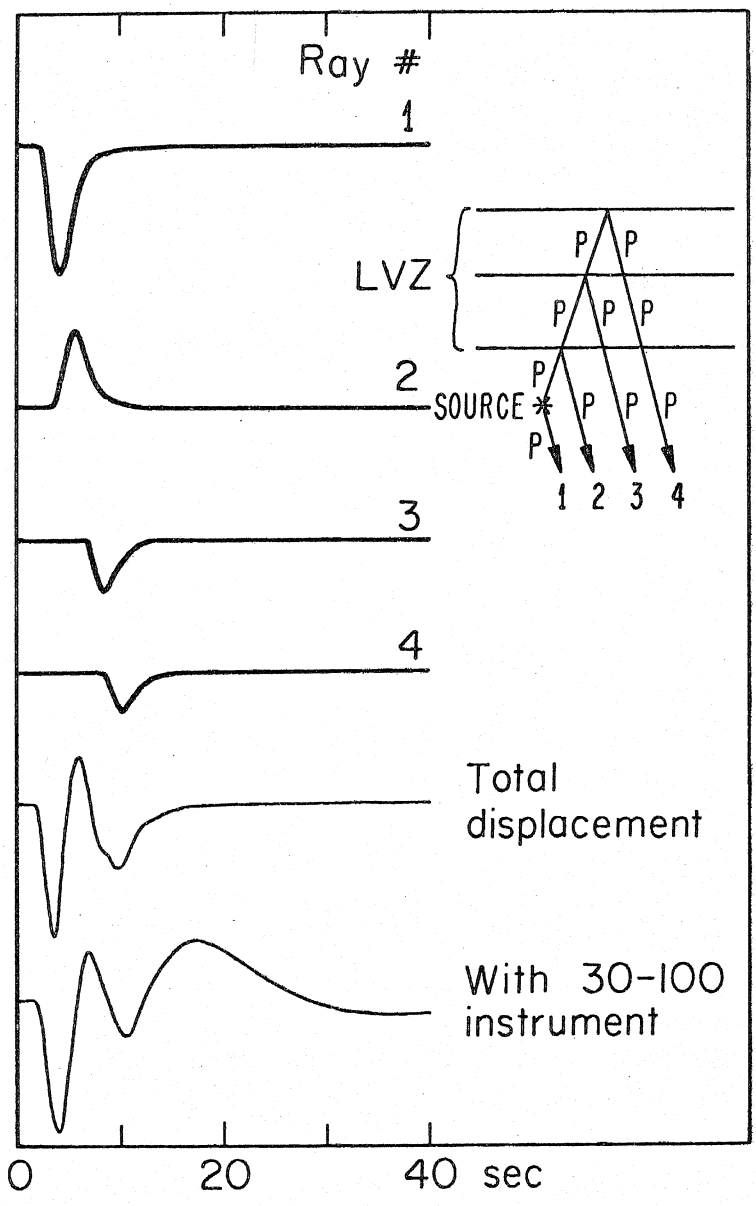

Figure 3.5. KEV ray summation showing the effects caused by reflections from interfaces bounding the inferred LVZ.

we are looking at relative amplitudes and velocity constraints only. This does point out that the absolute values of velocity for any part of the inferred model are somewhat ambiguous.

The phase pP and sP control and constrain the top of model PS-9. For the source function inferred from the direct P wave, it is evident that pP in a simple one-layer model (Figure 3.4) starts too sharply. The small arrival before pP suggests that a number of small reflections in the upper crust could give the desired effect of producing a smooth ramp before the main pP peak. Further evidence for this type of model occurs in the western stations HNR, GUA, and ANP. The predicted sP phase for the one layer model is much too large and is not affected by small changes in the radiation pattern. The easiest way to cut down this amplitude is to lower the reflection coefficient by using low velocities near the top of the model. This implies many contrasts also, since there must be some kind of transition from mantle to sediment velocities. This is the basis for modelling the upper crust in model PS-9. It is interesting to note that the crustal section had to be kept thin since thicker crusts caused spurious arrivals from the Moho before the arrival time of pP. The velocities for the top are not too well constrained. These values were determined by using the local refraction results of Berg et al. (1966) and Tatel and Tuve (1955). The

lowest velocities are appropriate for Tertiary clastic rocks as reported in Press (1966). The mantle velocity above the LVZ of 7.8 km/sec was based on the data of Dehlinger et al. (1965) and McCollum and Crosson (1975).

The S wave velocity is one of the least constrained parameters in the model. The average S time is only constrained by sP, a phase which is distorted and reduced in size by the model. However, there is some evidence that large S wave contrasts exist in the LVZ. At the western azimuth stations S-P reflections were needed to reduce the backswing of the direct P (see GUA, Figure 3.4, for a comparison) and theoretical arrivals after sP were only obtained after increasing the shear velocity contrast at the boundaries of the LVZ. These arrivals are shown as 'C' and 'D' in Figure 3.4 and are crustal multiples with substantial S to P conversions. Figure 3.2 shows that these multiples can help explain the arrivals after sP at these stations.

These multiples bring up interesting questions concerning the arrivals after pP at the northeastern and eastern stations. PS-9 predicts a few crustal multiples after pP but nothing like those in some of the observations. Figure 3.6 shows the long period P wave from the station KEV with a synthetic produced from the PS-9 model above and one made from a preliminary model, PS-1 (Table 3.2), below. The PS-1 model did not predict the LVZ interference effects very well nor the shape of pP for most observations. Because of the

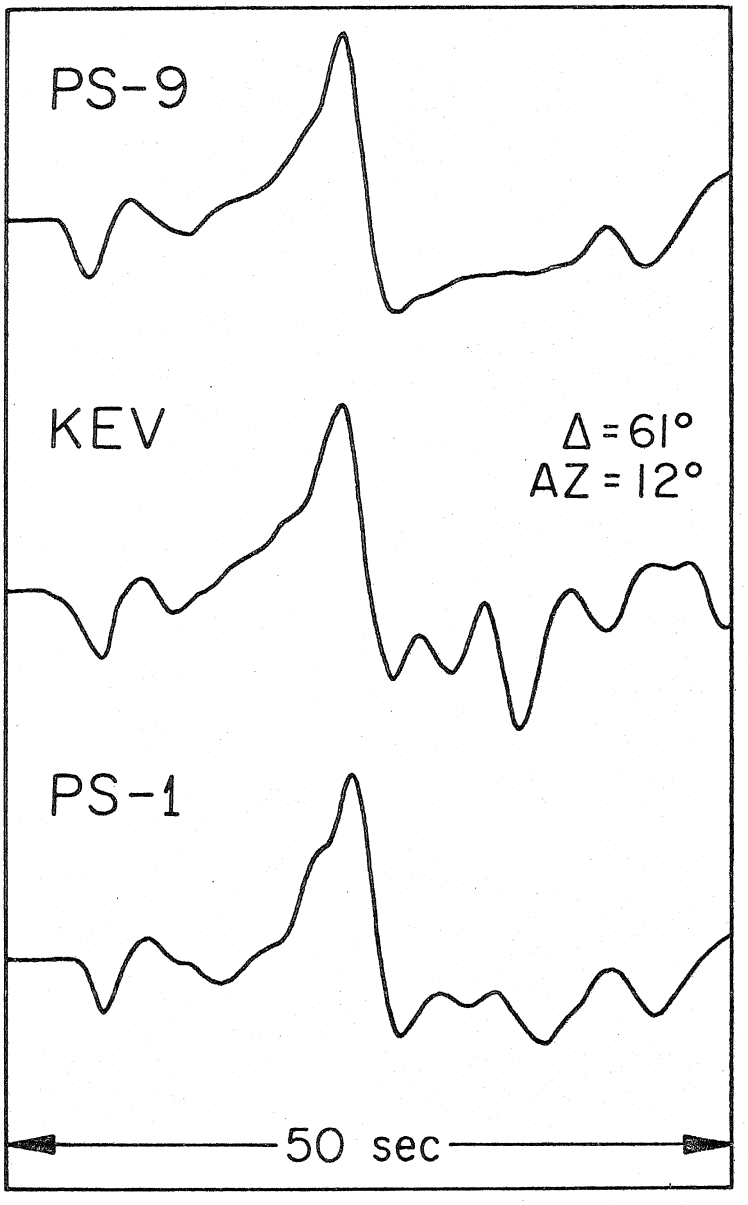

Figure 3.6. Comparison of P wave synthetic seismograms computed using the PS-1 and PS-9 earth models (Table 3.2) with the observation at KEV (middle).

low shear velocities and higher contrasts this model has, compared to PS-9, crustal reverberations after pP are quite pronounced and fit the observations quite nicely for this azimuth. However, since it did not fit the front part of the record very well, in general, it was not used. This exercise demonstrates that the arrivals after pP could conceivably be explained by large velocity contrasts although lateral inhomogeneity would probably be needed to match them. These crustal and mantle reverberations sample larger portions of the model and at distances further away from the epicenter as relative arrival times increase. Lateral changes over a scale length of 50 km, not inconceivable for the region coupled with the substantial depth of the source could be responsible for such effects. It must be mentioned that an added ambiguity inherent in this modelling is the lack of receiver characteristics. For the same reasons cited in the Koyna study, Chapter 2, no receiver responses were evaluated. Presumably, the effect for the vertical P wave is small but could be on the same order as the small arrivals behind pP. As such, these unknowns have to be considered a source of error in the study.

The evidence for constraining the rake angle of the north-south nodal plane comes from the relative amplitude of the reflection from the bottom of the LVZ. The observations of Figure 3.2 suggest that the reflection is more pronounced for the northern stations

(KEV, NUR, etc.) compared to the southern stations (QUI, NNA, LPB, ANT). Rather than invoke extreme lateral heterogeneity for this interface, a simple explanation can be made for the effect using fault orientation. If the fault was pure dip-slip ($\lambda = -90°$) the northern and southern stations should be identical since the radiation pattern would be symmetric about a line perpendicular to the fault plane. Varying the rake angle strongly affects only the upgoing SV radiation since it is near a node for eastern azimuths and this type of orientation. It was found that the interference of S-P conversions with the P reflections decreased the amplitude of the LVZ phases where upgoing SV was comparatively large. Using this effect the rake angle was deduced to be approximately -75° rather than pure dip-slip.

Modelling the rotated SH waves revealed little about the source or structure. Figure 3.7 shows the six observed SH waves with corresponding synthetic seismograms computed by ray techniques using the PS-9 model. Basically, the observed SH waves are very simple showing only the direct S. Most of the "glichiness" of these waves is due to digital noise in the rotation process. Since upgoing S is relatively small for these stations none of the major discontinuities of PS-9 are directly observable except for the free surface. The phase sS is not readily apparent in the observations although it is theoretically small. Several possibilities can be presented. First, the S-velocity structure of PS-9 may be completely wrong so that sS time is significantly different. However, examination of the

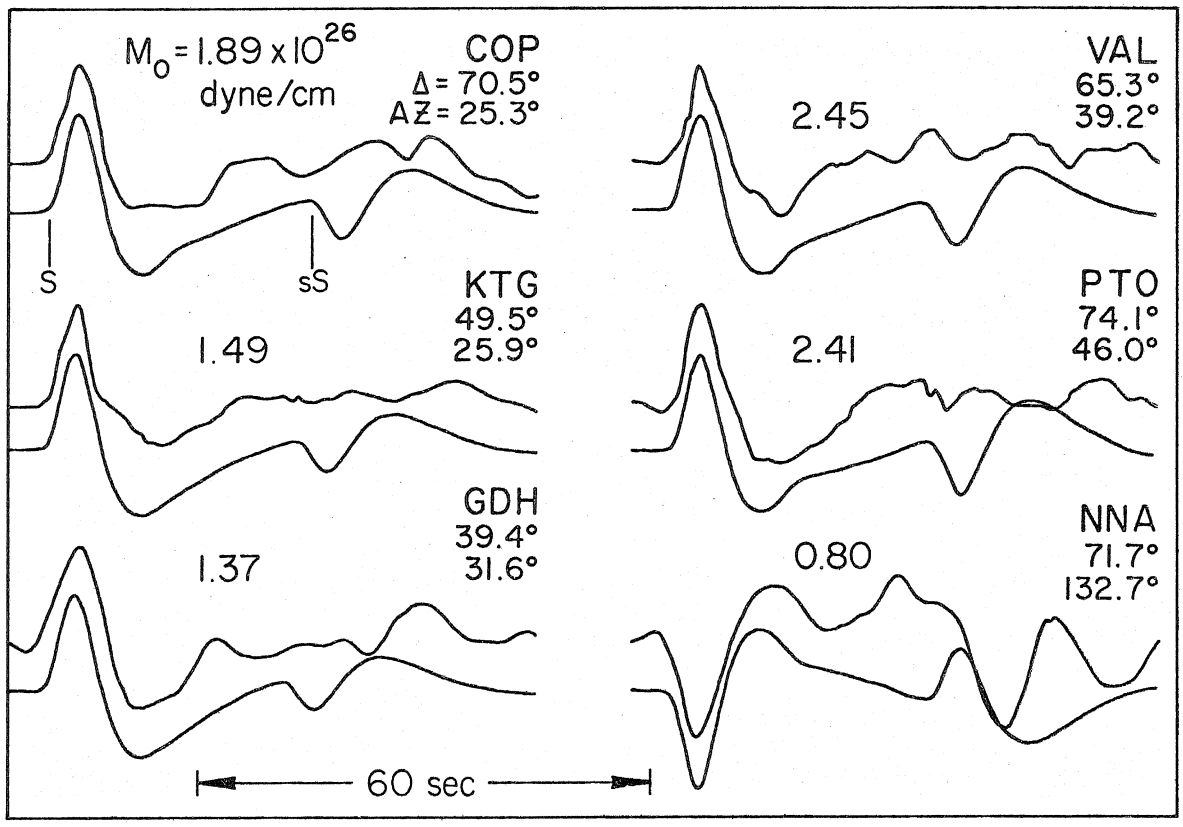

Figure 3.7. Comparison of the observed and final synthetic SH waves. Same scheme as in Figure 3.2.

SH observations yields no consistent arrival at any other time. A second possibility is that local receiver crustal effects such as S-coupled PL waves may contaminate the tangential component. S-waves are notorious for this and the position of sS relative to S makes this possibility very probable (Helmberger and Engen, 1974). A third and very likely possibility is that the earth model near the source is deficient. It could be that anelastic attenuation plays an important role. Some short period results will be presented below which support this speculation.

Scaling the synthetic direct P and SH waves to the long period data yields a moment determination for the Puget Sound event. A value of $1.3 \pm 0.6 \times 10^{26}$ dyne-cm is obtained from 21 P waves (see Figure 3.2). The uncertainty given is the standard error. The six SH waves, Figure 3.7, yield an average value of $1.7 \pm 0.6 \times 10^{26}$ dyne-cm, slightly higher than the P waves but well within the uncertainties of the geometrical spreading correction and assumptions on attenuation. The average moment including both P and S waves, is $1.4 \pm 0.6 \times 10^{26}$ dyne-cm. The scatter in amplitudes, yet not in waveshape, can be considerable even for nearby stations. For example, compare IST and ATU, Figure 3.2. Superimposed on this scatter is an apparent azimuthal variation. For eastern azimuths the average moment is about 0.8×10^{26} dyne-cm and less. Examining these stations

more closely suggests that observed pulse widths are wider than on the corresponding synthetics. Directivity could be a possibility but it would have to be of the form where the time functions for up- and downgoing rays were roughly the same shape and amplitude. The relative amplitudes of P and pP are quite satisfactory with the simple point dislocation assumed in Figure 3.2. The variation in time function shape for a simple circular fault model (Savage, 1966) is not very great, and for the difference in takeoff angles considered here, could not decrease the amplitude by a factor of two or lengthen pulses significantly. Another possibility could be an increase in attenuation for the region to the east of Puget Sound. An argument could be made that a partial melt zone under the Cascades is the source for this attenuation and for the andesitic vulcanism there. Dipping plate effects could also play a role. In a recent paper, Ward and Aki (1975) demonstrated that waveshapes can widen and decrease in amplitude in the amounts seen here by oblique transmission through a dipping slab model. Although there is no reason to believe that the details of their calculation hold for the Puget Sound area the general effect is quite interesting. Since there has been evidence presented for the slab hypothesis (see above) this effect cannot be completely discounted. It must be mentioned, however, that the Q and slab effects predict drastic reductions in the high frequency content of the signal. Examination of the short period components at

some of these stations showed them to be similar in frequency content to other 'normal' stations and does not support these particular explanations. At any rate, since the potential for speculation is so enormous for this problem any modelling attempt would be fruitless and hopelessly non-unique. It must therefore be taken as a shortcoming of the model or the method.

An attempt was made to utilize the many short period observations from this event to determine timing and amplitude information to help pin down the inferred structural discontinuities. Although the attempt eventually fell short of its original goals some interesting effects between the direct and reflected phases were observed.

In one sense a short period seismogram holds much more information than a corresponding long period observation by the simple fact that it has a broader frequency band. This is also the reason why it is so hard to use. A short period record will represent the sampling of every source detail and source and receiver microstructure to form a nearby incomprehensible morass. The tack taken here for their interpretation is to average or stack a number of seismograms in the hope of removing this 'noise' and to accentuate the coherency between them. We will borrow a few techniques from electromagnetic signal analysis to do this averaging procedure.

An easy way to change a short period record into a form suitable for stacking is to compute an envelope of the signal. Once the envelope is found for several records a suitable amplitude normalization is performed and the traces averaged with all seismograms lined up with respect to their first arrivals. A convenient way to compute the type of envelope needed here is to take the instantaneous amplitude of the analytic signal (Farnbach, 1975). The analytic signal is defined by (Bracewell, 1965)

$$\begin{aligned} \hat{S}(t) &= f(t) - iF_{Hi}(t) \\ &= |\hat{S}(t)|\, e^{i\alpha(t)} \end{aligned} \tag{3.1}$$

where,

$f(t)$ = observed time series

$\hat{S}(t)$ = analytic signal

$F_{Hi}(t)$ = Hilbert transform of $f(t)$

$\alpha(t)$ = time varying phase

$|\hat{S}(t)|$ = instantaneous amplitude.

The Hilbert Transform in equation (3.1) can simply be thought of as a convolution of $-1/\pi t$ with $f(t)$. Figure 3.8 shows an example of taking the instantaneous amplitude, $|\hat{S}(t)|$, of a short period vertical P wave recorded at AFI. This method preserves the times and relative amplitudes of the arrivals and even makes the record a little easier

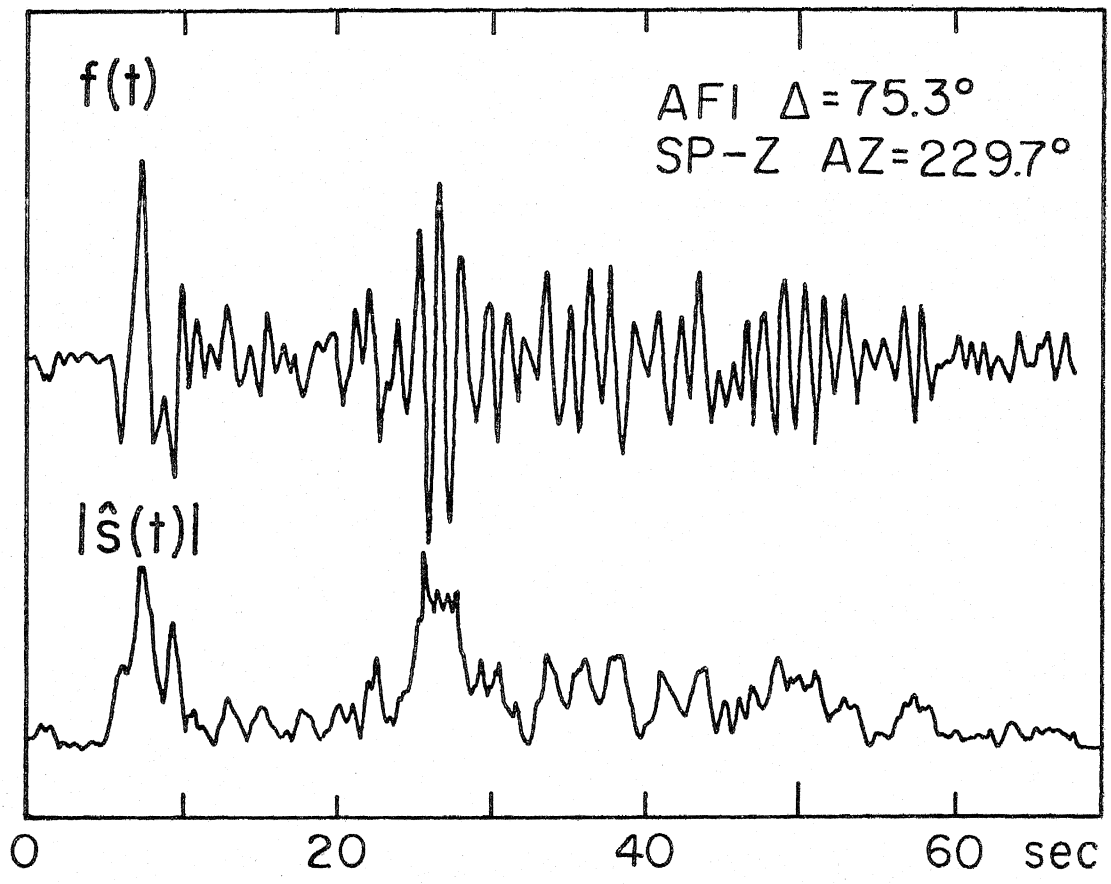

Figure 3.8. Example of finding the envelope of a short period record using the instantaneous amplitude of the analytic signal.

to visually interpret. By no means does it purport to add any information; it simply makes the sesimograms easier to work with. The normalization was done by setting the area of the first 10 seconds of the envelope to unity. This tended to boost the relative amplitude of sharp arrivals to that of emergent arrivals.

Figure 3.9 shows the results obtained from a stacking experiment. The traces labelled 'P' are stacked envelopes of short period vertical P waves grouped as a function of range. The range interval is indicated under each group name and the number in parentheses represents the number of seismograms used per group. Table 3.1 indicates the particular stations used in this grouping. The P wave stacked traces show several interesting effects. In the first 10 sec two prominent arrivals are usually evident and are designated P and p_mP in the diagram. The first arrival is interpreted to be the direct P wave with p_mP being the reflection from the bottom of the LVZ. The timing agrees with the long period result. This is not too useful except to show that the reflection has approximately the same frequency content as the direct wave. This implies that the contrast at this boundary must be sharp, probably less than 2 km in transition. The most striking effect these traces demonstrate, however, is the very conspicuous absence of pP, especially at the smaller epicentral distances. A simple glance at the long period waveforms in Figure 3.2 reveals that, except for the western stations, pP

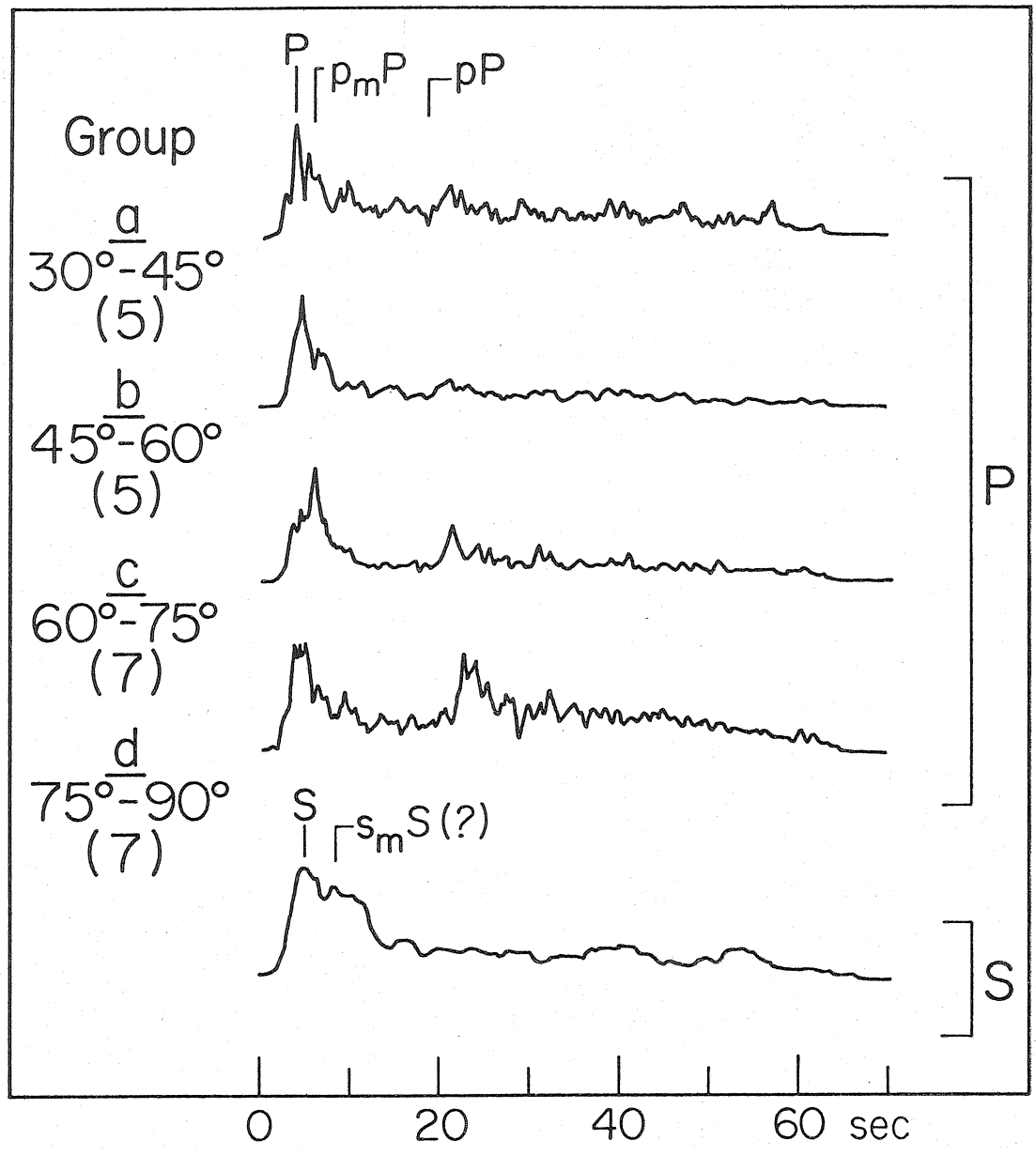

Figure 3.9. Stacked envelopes of short period P and S waves. The arrows point directly to the phase being identified except for the pP arrow, which designates the theoretical arrival time.

is at least as big as direct P and usually two or three times bigger. The relative amplitude of pP in groups a, b, and c of Figure 3.9 is at least half that of direct P. Not until stations with ranges greater than 75° are considered does pP start becoming apparent. This effect can be inferred to come from earth structure by using the information gleaned from $p_m P$. Because the frequency content of upgoing rays is similar to that of the downgoing rays a source effect, such as directivity, can automatically be eliminated. All reflections should be apparent unless structure or attenuation effects cancel the arrivals.

An explanation for this observation can be found in the geologic and structural framework of Puget Sound. Figure 3.10 is a map of southern Puget Sound with the epicenter plotted near the center (after Algermissen and Harding, 1965). The concentric circles are contours of the position pP hits the surface for a particular station distance. These were computed from ray theory for model PS-9 using the expression

$$x_r = \sum_{j=1}^{n} \frac{p}{\eta_{\alpha_j}} Th_j \qquad (3.2)$$

where

x_r = radius from epicenter

p = ray parameter considered

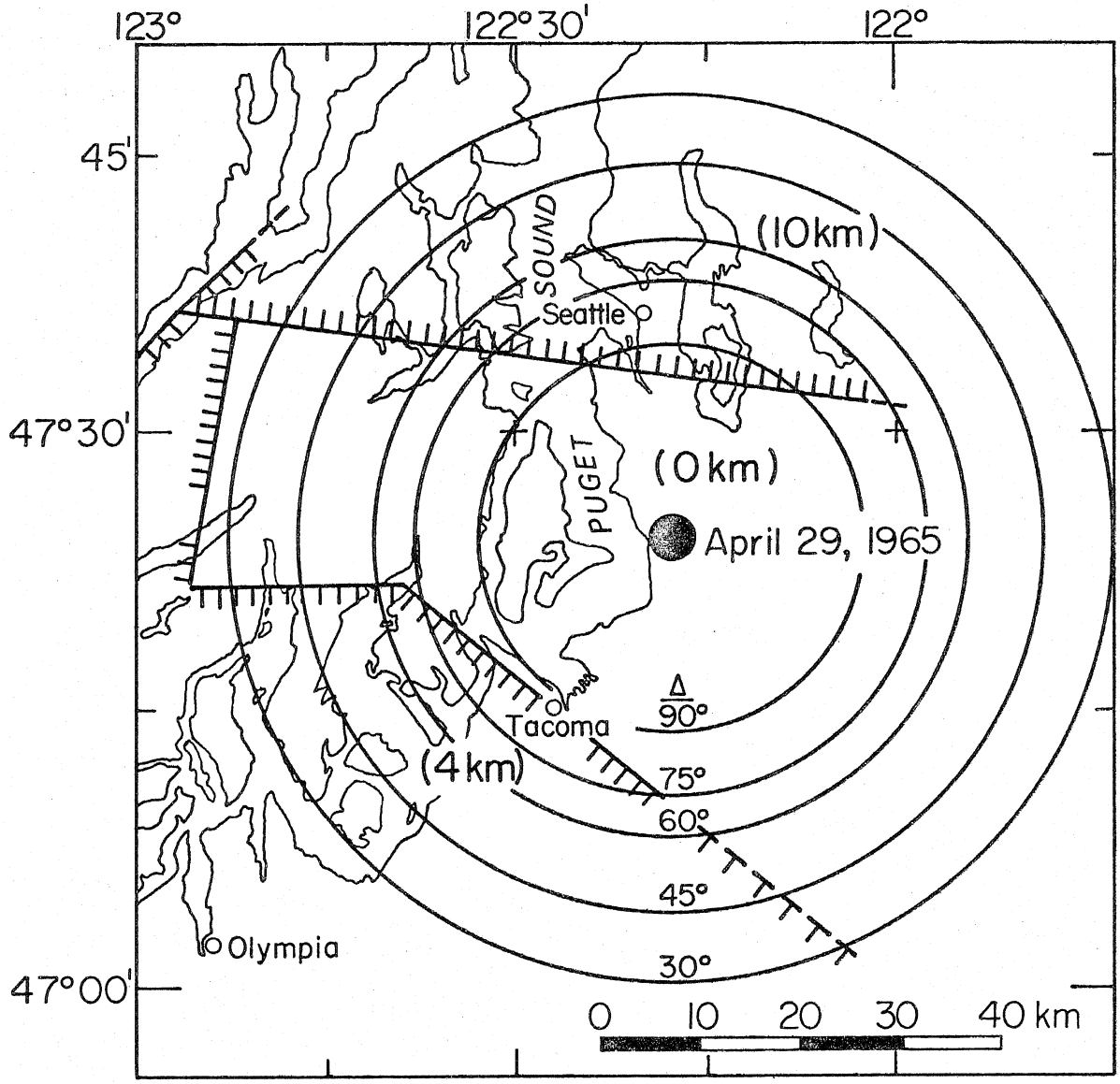

Figure 3.10. Map of the southern Puget Sound area showing the epicenter for the 1965 event (after Algermissen and Harding, 1965). The concentric circles are contours of pP reflection points as a function of epicentral distance. The hachured lines are faults inferred by gravity and magnetics from Daneš et al. (1965) with the tick marks on the downthrown side. The numbers in parenthesis are depth to basement in km.

$$\eta_{\alpha_j} = \left(\frac{1}{\alpha_j^2} - p^2 \right)^{1/2}$$

Th_j = thickness of the j^{th} layer

The summation is for all layers between the hypocenter and the free surface. The hachured lines across Figure 3.10 represent a simplified version of structural discontinuities from the gravity and magnetic interpretation of Daneš et al. (1965). They are dashed where questionable. The tick marks are on the down-thrown side of the inferred fault. The large numbers in parentheses are inferred depths to crystalline basement from the surface. This map readily demonstrates the great structural relief and complexity in the near-surface geology. The contours of pP are only approximate when considered from this approach since they were calculated using a plane layered model, an assumption which clearly breaks down for the near surface layers. Nevertheless, they should be useful to first order. Comparing the distance ranges and the structure gives a possible explanation for the amplitude behavior of short period pP. For all stations at distances less than 75° pP bounces at points which have thick sections of sediment. For stations with ranges greater than that, pP bounces within the boundaries of the large horst or near its edge where sediment thicknesses are presumably smaller. This observation seems to correlate with the effects seen in the traces of Figure 3.9. Possibly, then, the attenuation of pP

relative to P comes from either structurally disturbed sediments causing wave scattering or perhaps from anelastic attenuation. Either mechanism is feasible. An effective 'Q' can be computed from these observations by using equation (1.15). A conservative estimate of the amplitude attenuation factor, a, is about 1/3 for a .75 sec short period sinusoid, and with a total travel time, T, of 17 sec gives

$$Q_{eff} = \frac{-\omega T}{2 \ln a} \qquad (3.3)$$

$$= 65$$

This amounts to convolving pP with another Q operator on top of the first (T/Q = 1.0) with a travel-time to Q ratio of 0.3. This particular Q operator would have negligible effect on a long period waveform.

The realization that Puget Sound is structurally heterogeneous can explain why the shape details of pP are not fit by PS-9 for all azimuths (see Figure 3.2). In fact, it is surprising that the model works at all. Perhaps the pathological case of GDH, Figure 3.2, can have an explanation in this light.

Returning to Figure 3.9, one last point can be made using the short period stacking procedure. The bottom trace, labeled 'S', is the average of both horizontal short period S wave components at seven stations (Table 3.1). The result of the averaging revealed

two arrivals roughly 3 sec apart. The first is interpreted to be direct S. Comparisons with each corresponding long period component revealed that the short period S started after any long period S-P precursors and correlated with where the long period arrival increased fastest and was sharpest. The second arrival, because of its timing, is interpreted to be the reflection from the bottom of the LVZ. This arrival did not occur at all stations and there were significant waveform variations between stations to make this a tentative conclusion. It does give weak evidence against multiple source complications through the agreement in travel times for the inferred reflected S phase.

Discussion of the earthquake results

The source model presented here is an exceedingly simple one. The orientation agrees with previous studies and the time function is short and uncomplicated. It is certainly quite possible that there are other source complications but an earth model has been presented which, if anything, demonstrates the problems one has to deal with in order to discern these effects.

The earth model, on the other hand, is relatively complicated. In some respects it is heartening to see how some parts of the model agree with the geology and previous geophysics. For example, the inferred crustal thickness is less than 15 km. The refraction results are consistent with this including a recent study using

local mine blasts recorded by the Puget Sound seismic array. This particular study also obtained a shallow depth to Moho of 10 to 15 km (H. Zuercher, personal communication, 1976). The low velocity layers at the top of the model, needed to widen pP and attenuate sP, correlate very nicely with the thick sections of presumably Tertiary sediments under the blanket of glacial till. On the other hand, discovery of the massive LVZ in the uppermost mantle presents many problems in uniqueness, although the model produces a good fit to all the P waves. Clearly, a check on this conclusion is desirable. One way to do this would be to examine another earthquake to see if the same structure effects are observable. The 1949 event would be the logical choice since it occurred nearby and at a depth of 70 km. The records, however, are not easily available and the orientation of the event, relative to the station coverage, might not be appropriate for observing these effects. Because the inferred structural boundaries of the LVZ are so distinct they should be directly observable from upcoming phase conversions and reverberations using teleseismic sources for stations situated over the structure. Fortunately, there are several long period WWSS and Canadian network stations nearby to test the model in this manner.

Corvallis, Oregon, Receiver Structure from Teleseismic P and S Waves

Although several long period stations are near Puget Sound, the WWSSN station, COR, at Corvallis, Oregon, will be chosen to test the inferred Puget Sound structure (see Figure 3.1). There are several reasons for doing so. Primarily, COR lies in the same physiographic province, the Puget-Willamette depression, and therefore has the best geologic chance of having a similar structure. Secondly, the data set for COR is more complete in terms of high quality, low noise seismograms from teleseismic sources than other regional stations and is, most importantly, easier to interpret. Finally, it is out of the scope of this thesis to do an extensive regional study of crustal structure although this is certainly an interesting and important problem. We will therefore be concerned with inferring the crustal and upper mantle structure at COR to find supporting evidence for the LVZ and to form a basis for further similar studies at other nearby stations.

Method

The procedure for deducing crustal and upper mantle structure using one three-component long period station is basically very straightforward. Long period P and S wave observations from deep and intermediate teleseismic ($\Delta > 30°$) events will be modelled in the time domain for directly observable structure phases such

as Ps and Sp. The computational techniques will be simplified versions of the ray and layer matrix methods presented in Chapter 1. We will assume that the earth can be represented by a series of plane homogeneous elastic layers and that waves impinging below the structure are sufficiently far from their source so they can be considered plane waves. These plane P and S waves will be described by one ray parameter appropriate for the source distance and depth.

Ray theory will be relied upon to furnish direct interpretations concerning the relative arrival times and amplitudes of particular phases. The mechanics of this are exactly as described in Chapter 1. Ray paths are specified through a particular model and the usual transmission and reflection coefficients are used to find the amplitude. Travel time is also determined by the same methods (equation 1.13).

To find the total response for a relatively complicated model the ray approach becomes unwieldy for exactly the same reasons stated in Chapter 1. Layer matrix techniques again become convenient since they can solve the entire problem without recourse to complicated and lengthy ray descriptions. The solution for displacements at the free surface for impinging P and S plane waves in a halfspace below a stack of layers (Figure 1.9) is well known (Haskell, 1960, 1962) and is given by

P waves

$$U_p = \frac{2c}{\alpha_n} \frac{(J_{42} - J_{32})}{D}$$

$$W_p = \frac{2c}{\alpha_n} \frac{(J_{41} - J_{31})}{D} \qquad (3.4)$$

SV waves

$$U_s = \frac{c}{\beta_n} \frac{(J_{12} - J_{22})}{D}$$

$$W_s = \frac{c}{\beta_n} \frac{(J_{21} - J_{11})}{D} \qquad (3.5)$$

SH waves

$$V = \frac{2\mu_n r\beta_n}{\mu_n r\beta_n A_{L_{11}} + A_{L_{21}}} \qquad (3.6)$$

where

$$D = (J_{11} - J_{21})(J_{32} - J_{42}) - (J_{12} - J_{22})(J_{31} - J_{41})$$

and the rest of the parameters defined as in Chapter 1. The displacements U,W, and V are the radial, vertical, and tangential components, respectively. These expressions are evaluated in the frequency domain, and convolved with a suitable source time function, instrument, and attenuation operator. This total response is then inverted into the time domain via the Fast Fourier Transform.

Many investigators have approached this type of modelling problem by making extensive use of spectral amplitude ratios (Hannon, 1964; Phinney, 1964; Fernandez, 1967; Leblanc, 1967; Fernandez and Coreaga, 1968; Bonjer et al., 1970; Kurita, 1973a, 1973b; Leong, 1975). In this technique the spectral ratio of the radial to vertical P wave components is found using an arbitrary teleseismic earthquake source. This essentially deconvolves the source function from the observations since it should be common to each component, assuming they have matched instrument responses. The observed amplitude ratios are then compared to theoretical ratios, computed from equation (3.4), for several types of crustal models. Although this method removes the source function it has the drawbacks of all spectral interpretations. It is exceedingly hard to study the timing and amplitude of individual phases in the frequency domain and to directly interpret the spectral ratio. The added uncertainties of truncation errors and digital noise adds to the confusion since taking a spectral ratio is equivalent to a deconvolution which is a very unstable process. We will therefore take the approach of directly modelling the observations, both P and S waves, in the time domain by using estimates of the incident source function. All assumptions are clearly presented, in this manner, and are directly observable in the synthetic seismogram. The radial and vertical P components and vertical SV components will be used extensively in the interpretations to follow.

Recently, Jordan and Frazier (1975) investigated SP precursors using this time domain approach although they made no use of the P waves.

To illustrate what types of structure effects distort incident P and S waves let us examine a simple one layer model over a halfspace. Figure 3.11 displays responses for several earth models, whose parameters are listed in Table 3.3.

All the seismograms of Figure 3.11 were computed using the layer matrix formulation (equations 3.4, 3.5, 3.6), have a 15-100 instrument response and have a simple triangular time function ($\delta t_1 = \delta t_2 = 1.0$ sec) included. The attenuation parameters (T/Q) assumed for P and S waves were 1.0 and 4.0, respectively. Values of .06 and .1 sec/km were used for the P and S ray parameters, respectively, and are appropriate for a source range of 60 degrees. Examining the horizontal and vertical P waves of the one layer model immediately indicates the relative complexity between these components and where most of the structure information lies. Since the incident angle for teleseismic P waves is relatively steep, P-S conversions should be predominant on the radial component rather than the vertical. This is very apparent in the ray descriptions. The notation used in describing ray paths for the one layer model is adopted from Båth and Stefánsson (1966). The first capital letter, P or S, designates the incident wave. Small case letters refer to upgoing waves in the layer and subsequent capitals refer to the

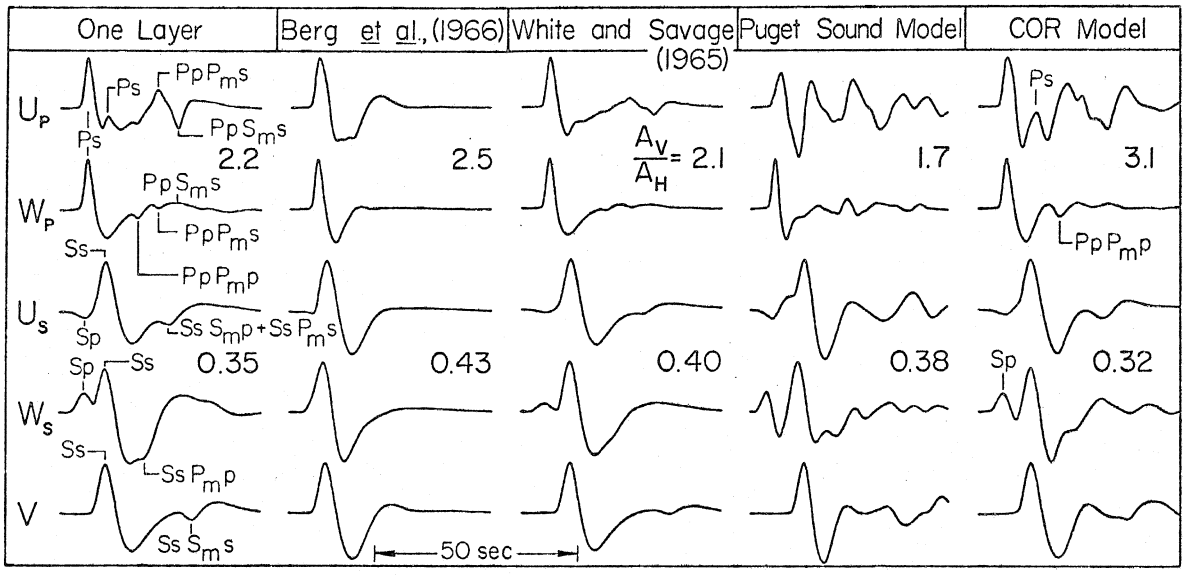

Figure 3.11. Synthetic seismogram calculations for all P and S wave components for the earth models of Table 3.3.

Table 3.3

Earth Models

		Layer #	V_p (km/sec)	V_s (km/sec)	ρ (gm/cc)	Th (km)
1)	One layer over halfspace	1	6.0	3.5	2.6	40.0
		2	8.1	4.7	3.2	-
2)	Oregon Coast Range (Berg et al, 1966)	1	4.4	2.5*	2.5*	2.2
		2	5.5	3.0	2.6	7.7
		3	6.6	3.8	2.8	3.8
		4	7.4	4.2	3.0	2.1
		5	8.0	4.6	3.2	10.0
3)	Vancouver Island (White and Savage, 1965)	1	6.0	3.5*	2.7*	6.2
		2	6.73	3.9	2.8	45.0
		3	7.74	4.5	3.1	-
4)	Puget Sound Model	1	2.0	1.0	2.5	1.2
		2	3.0	1.5	2.5	1.2
		3	4.5	2.3	2.5	2.5
		4	6.8	3.9	2.9	4.0
		5	7.4	4.2	3.0	4.5
		6	7.8	4.3	3.2	27.3
		7	6.5	3.1	2.9	7.0
		8	5.5	2.9	2.7	8.0
		7	8.0	4.6	3.2	-

Table 3.3 (continued)

	Layer #	V_p (km/sec)	V_s (km/sec)	ρ (gm/cc)	Th (km)
5) Corvallis Model	1	5.5	3.0	2.6	10.0
	2	6.7	3.9	2.8	6.0
	3	8.0	4.6	3.2	5.0
	4	7.9	4.5	3.15	1.5
	5	7.8	4.2	3.1	2.0
	6	7.7	3.7	3.0	1.5
	7	7.5	3.5	2.95	1.5
	8	7.2	3.3	2.9	2.0
	9	6.9	3.3	2.85	2.5
	10	6.6	3.3	2.85	12.9
	11	8.0	4.6	3.2	-

* - assigned S velocities for this study.

downgoing wave. The subscript 'm' refers to a reflection at the 'Moho', or the 8.1 - 6.0 km/sec boundary. The major phases occurring on the horizontal P component are the Ps conversion at the Moho and subsequent P reverberations with the final ray legs spent in the S mode. The vertical P wave is relatively undistorted with the first P reverberation producing the largest later arrival. The most important phase in the SV components, other than the direct wave, is the Sp precursor. Since Sp is largest on the vertical SV component, this component should be used for its interpretation, as pointed out by Jordan and Frazier (1975). SH waves are relatively uninteresting with the only major crustal effect occurring far back in the record. Since the effect is small and this part of the S record usually noisy, the SH waves will not be utilized in the structure inversions.

Because we will be doing direct interpretations of the data by comparison with time domain synthetic seismograms the source function of the incident wave will have to be estimated. In general, however, it is hardly ever known. To minimize this problem, only deep and intermediate depth earthquakes will be used so that free surface and other near source complications are avoided. Furthermore, a group of several events rather than a single event will be studied to make sure that interpreted structure effects are consistent

over the entire data set. The earthquake data set is chosen on the basis of favorable signal-to-noise ratio and simplicity of the waveform. Earthquakes which have vertical P waveforms containing two or more obvious pulses are avoided. The vertical P wave is used for this decision on the basis of the one layer theoretical study of Figure 3.11. The vertical P wave is also used to find an estimate for the effective source time function by examination of the instrumental deconvolution (see equation 2.1) and through trial and error waveform fitting.

Data and Data Interpretation

A search of the WWSSN data for COR along the above guidelines yielded the earthquakes listed in Table 3.4. Not every wave type or component was used from each earthquake depending on its range and signal to noise ratio. For example, the 9/9/67 event was clear on the vertical P component, but the horizontal P wave was in the noise because of the earthquake's large range. The data waveforms were digitized according to the methods of the previous chapters. Because the station was not naturally rotated, with respect to the ray directions, the horizontal P waves were rotated into the theoretical back azimuths to get the radial component. This process was successful in all cases judging by the close agreement between the amplitude levels of the 'tangential' P wave and the noise before

Table 3.4

Epicenter Parameters (ISC)

Date	Time	Lat.(0)	Long.(0)	M_b	h	Δ(0)	BAZ(0)	Location
11/3/65	01:39:03.2	9.10S	71.40W	6.2	583	71.0	124.7	Peru-Brazil
2/15/67	16:11:11.8	9.05S	71.34W	6.1	598	71.0	124.7	Peru-Brazil
9/9/67	10:06:44.5	27.62S	63.15W	5.9	577	90.41	129.7	Argentina
12/27/67	9:17:50.3	21.29S	68.20W	6.3	91	82.6	129.5	Chile
1/19/69	7:02:07.9	44.89N	143.21E	6.3	238	62.5	306.9	Japan
1/29/71	21:58:03.2	51.69N	150.97E	6.0	515	54.5	310.3	Sea of Okhotsk

the signal. This implies that non-planar structure is not a large effect.

The data and corresponding synthetics for the final model are presented in Figures 3.12, 3.13, and 3.14. For each waveform pair the observed is on top and the synthetic displayed directly below. To the left of these traces is the effective time function used in computing the synthetics. The final Corvallis earth model is presented in Figure 3.15 and listed in Table 3.3. Again, as in the Puget Sound study, both the waveform fits and the earth model have several striking characteristics. The wave fits are generally excellent and reproduce the main observed effects. The earth model is again very unusual in that it has an extensive LVZ in the uppermost mantle with a high contrast lower boundary.

The modelling process which produced this final earth structure can most easily be explained by returning to Figure 3.11 which displays the comparison of several synthetic models. The model of Berg et al. (1966) should be most appropriate since they used the station COR in their study. However, this model does not predict any of the phase conversions or reverberations seen in the data. Compare the P waves of the 12/27/67 event in Figure 3.12 with this model, for example. Although these phases are produced by the layer

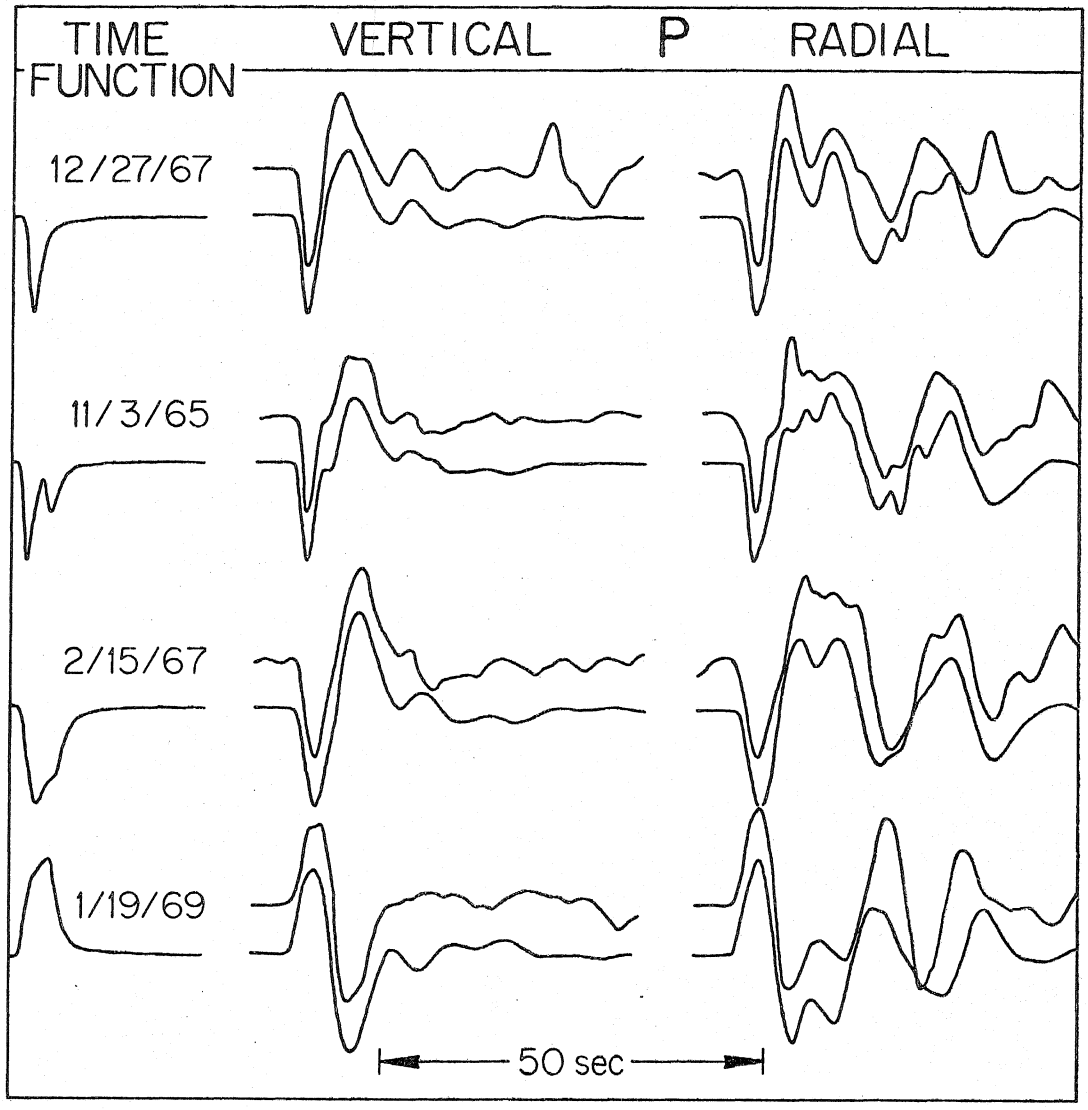

Figure 3.12. Comparison of observed and final synthetic waveforms for the horizontal and vertical P wave components. The observed is on top for each component. To the left of each vertical-horizontal set is the effective time function that was used in the synthetic calculation.

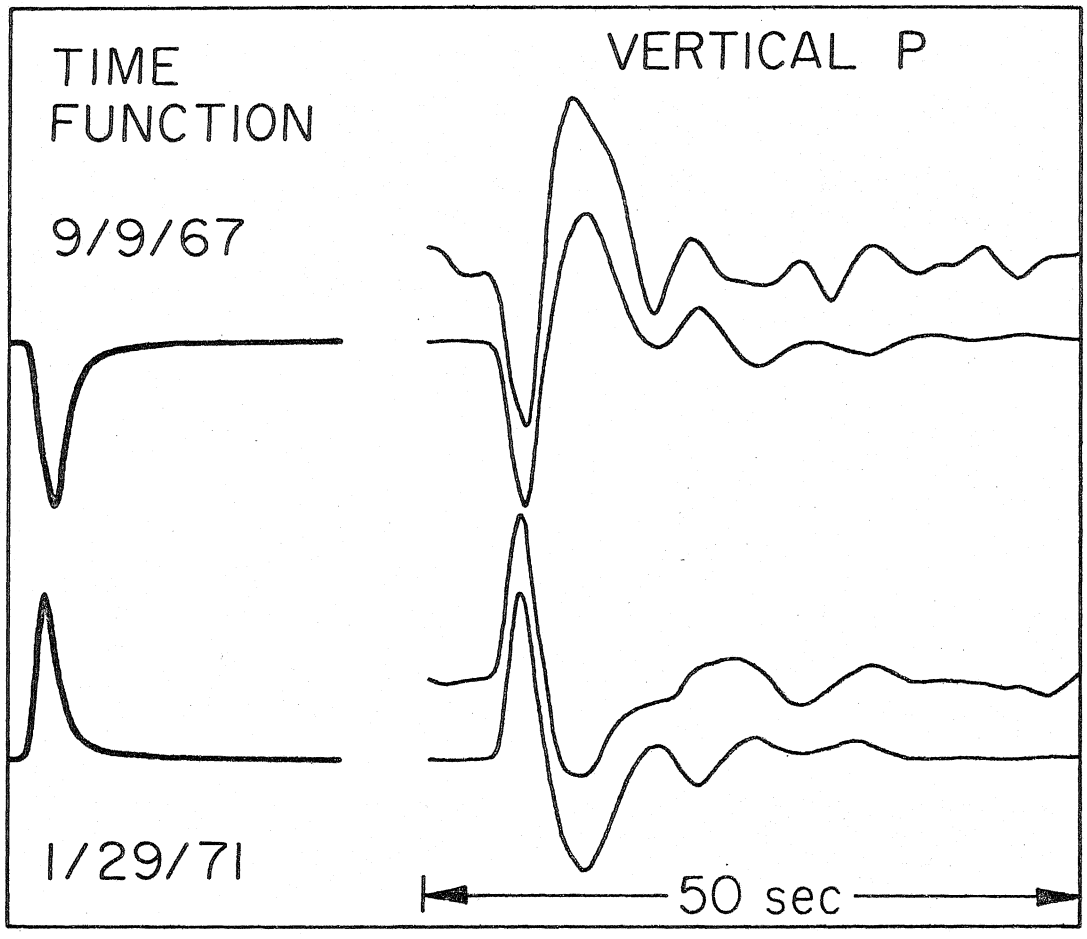

Figure 3.13. Comparison of observed and final synthetic waveforms for the vertical P component from two earthquakes. Same scheme as Figure 3.12.

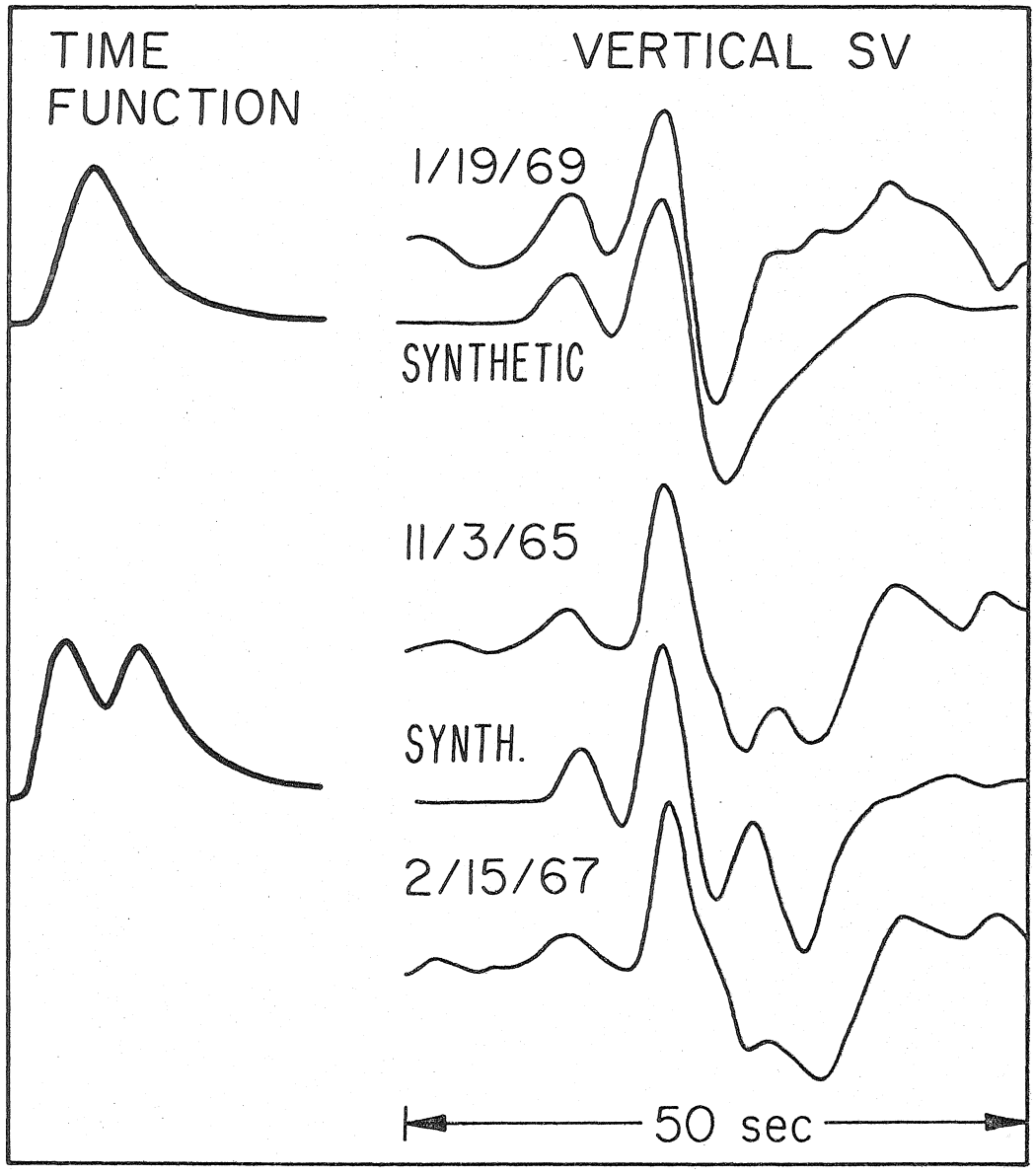

Figure 3.14. Comparison of observed and synthetic for the vertical SV component from three earthquakes. Same as Figure 3.12.

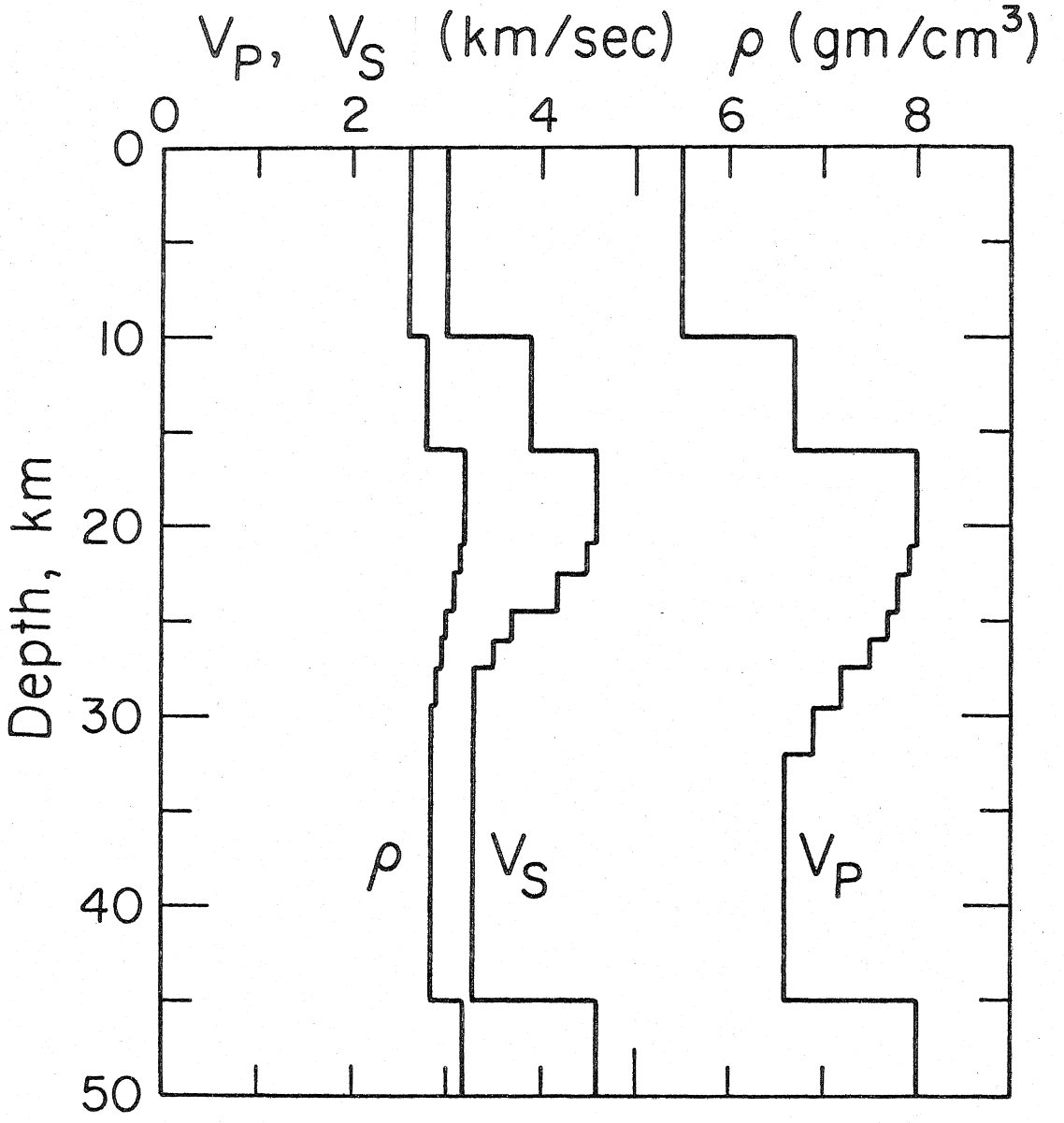

Figure 3.15. Final Corvallis crust and upper mantle model.

interfaces,the total crustal thickness, and hence, travel time, is too small for them to be directly observable. The model of Vancouver Island by White and Savage (1965), although thicker, still does not produce the desired amplitudes for later arrivals implying, at least, that there must be high velocity contrast interfaces under COR. The Puget Sound model inferred from the earthquake study produces conversions and reverberations which are too severe compared to the data. This indicates that the details of the Puget Sound structure do not extend to COR, a not totally unexpected result considering the geologic heterogeneity of the region.

An apparent paradox is raised by these model investigations. How can the model inferred from long range refraction (Berg et al., 1966),and supposedly appropriate for COR,be consistent with the need for a high contrast interface to produce large amplitude conversions and reverberations? The answer to this question can be found by examining the travel times of the observed phases.

An average travel time of 7.3 sec for Sp relative to direct S can be obtained from the three vertical SV components in Figure 3.14. The estimated reading error is about ± 1 sec. The change in travel time due to differing ray parameters is negligible for these ranges. A second S minus P time can be estimated from the Ps phase which is very prominent on the radial P wave component. Using the radial P observations of Figure 3.12 this travel time comes out to be

6.8 sec, relative to direct P. The Corvallis model synthetic calculation of Figure 3.11 has these phases identified for reference. The consistency between the Ps-P and S-Sp times is excellent and supports the contention that these phases originate from the same layer interface.

Assuming Berg's crustal structure and upper mantle velocity (see Table 3.3) and using the measured S-P times, assuming an average Poisson ratio of 0.25, yields a depth to the interface of about 65 km, a very remarkable result. However, unless unreasonably high upper mantle velocities exist under Corvallis to create the necessary shear velocity contrast of 1.0 to 1.5 km/sec a velocity inversion must take place between the Moho of Berg's model and the interface. This contrast was estimated using ray theory and the relative amplitudes of Sp (1/19/69 event) and Ps (12/27/67 event).

Fortunately, there are other model constraints which can be found directly from the teleseismic data. Since the contrast is large, as inferred from the relative amplitude of the converted phases, it is very reasonable to expect large reverberations also. In particular, if the first P multiple could be observed it would be extremely useful in constraining the average P velocity between the interface and free surface. This phase is indeed observable and is shown in Figures 3.12 and 3.13. Also apparent is an interesting azimuthal dependence for this phase. For the four earthquakes in

the southeast (9/9/67, 12/27/67, 11/3/65, 2/15/67) this P reverberation is very prominent. For the other two events situated to the northwest (1/19/69, 1/29/71) the phase is very weak or missing. There is a possibility that dipping or discontinuous structure might cause this, but this is not supported by the excellent Sp and pS observations of the 1/19/69 event. A more reasonable possibility is a near surface effect in which the effective reflection coefficient at the surface is modified by the geology. The bounce points for the southeastern events are in the alluviated Willamette Valley which would tend to cause relatively large P reflections. The northwest azimuths, however, contain outcrops of Eocene basalts (Bromerly and Snavely, 1964) whose higher velocities could conceivably reduce the free surface reflection coefficient or cause scattering. These speculations only illustrate that the model assumptions start to break down when multiples are considered.

Other problems arise from this phase interpretation. For example, the 11/3/65 and 2/15/67 event are at a range ($\Delta = 71°$) where PcP arrives very close to the inferred multiple time making the interpretations ambiguous for these events. To prove the existence of the P multiple a comparison was made of two earthquakes recorded at both COR and Longmire, Washington (LON, see Figure 3.1). A qualitative examination of the horizontal and vertical P waves revealed that the LON structure was more subdued in terms of large-contrast interfaces as compared to COR. LON is less than 200 km from

COR which should have negligible effect on waveshapes from teleseismic sources due to azimuthal variations in the radiation pattern. Figure 3.16 displays the comparison for the 12/27/67 and 9/9/67 events. This comparison demonstrates that the arrival is indeed a local structure effect and not due to the source.

An average travel time of 12 seconds is obtained for this phase using the vertical P components of Figures 3.12 and 3.13. If the reasonable assumption is used that this phase reflects off the same interface which produces the conversions, some very interesting results are obtained on material properties of the COR upper mantle. Using a simplification of Berg's model for the velocities in the crust and uppermost mantle along with the inferred average travel times for the converted phases implies shear velocities approximately half as large as P velocities. This corresponds to an average Poisson ratio, σ, of 0.33 using

$$\sigma = \frac{\alpha^2 - 2\beta^2}{2(\alpha^2 - \beta^2)} \tag{3.7}$$

This unusual material property coupled with the large velocity contrasts needed to produce the prominent phase conversions suggests strongly that a major low velocity zone exists under Corvallis.

The Corvallis model displayed in Figure 3.15 was a result of modelling the P waves from the 12/27/67 event and the vertical SV wave from the 1/19/69 event. These particular earthquakes were

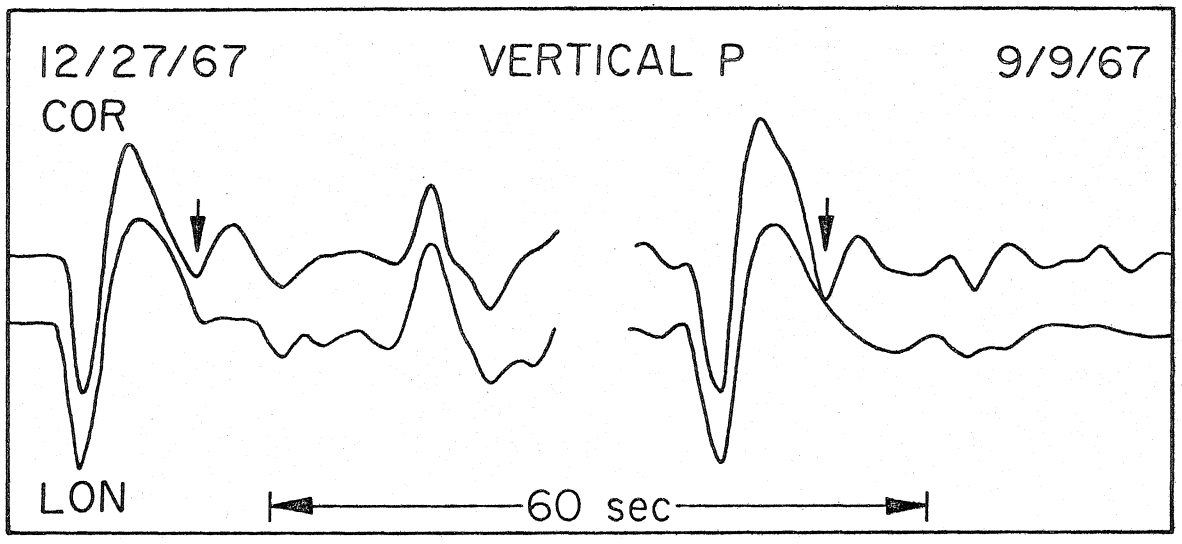

Figure 3.16. Comparison of the vertical P components for the same earthquakes recorded at LON and COR. The arrows designate the arrival time of the first P multiple for COR.

used on the basis of the simplicity of their inferred time functions. The absolute velocities of the LVZ and lowermost mantle in the Corvallis model are not constrained quantities and could vary by ± 0.5 km/sec without significantly changing the conclusions. The gradients at the top of the LVZ were put in to minimize SP conversions which are not observable in the data. The density profile is assumed and may be changed without much detriment to the fits. It does help the overall contrast at the bottom interface, however, and because of the large velocity contrasts, is reasonable. The details of the gradients can also be changed and are not unique as long as the contrast at the bottom interface and average S and P travel times are satisfied.

It was found that using the simplest events for the earth modelling procedure was sufficient to explain all other waveforms in the data set once an estimate of each source time function was known. For example, the vertical-radial comparisons of Figure 3.12 worked remarkably well for the time functions obtained from just the vertical components. The interference and relative amplitude behavior of Ps relative to P was found to be a sensitive function of incident pulse shape and justifies the careful search for relatively simple earthquake

It is interesting to note how well the reverberations after Ps, Figure 3.12, were fit both in timing and periodicity. These

particular phases were not used to constrain the earth model but fell naturally from it once the observed and amplitude of the direct conversions were matched. As such, these reverberations add to the consistency of the assumptions and interpretations used in the modelling procedure.

The vertical SV waves for the 11/3/65 and 2/15/67 events represent what can happen to amplitude and waveform studies which use a relatively complicated event. Burdick and Helmberger (1974) studied the 11/3/65 earthquake and concluded that it was a multiple source from a deconvolution technique. Jordan and Frazier (1975) used this source in their interpretation of Sp precursors in the Grenville Province of Canada. They observed a source time separation of about 6 sec and discovered that this source function introduced some ambiguity into their results due to the interference of the multiple peaks. The bottom time function of Figure 3.14 uses the time separation inferred by Jordan and Frazier. The resultant total response, although not perfect, clearly shows the complications introduced in the Sp to S amplitude ratio and the later arrivals in the waveform. The 2/15/67 observation is also shown with the 11/3/65 SV synthetic. The vertical P waves showed similarities to each other in terms of multiple arrivals but were somewhat different in width (Figure 3.12). Because of this and the almost identical behavior of the vertical SV waves it was concluded that this event too was a multiple source.

Discussion of the receiver modelling results

Although the Corvallis and Puget Sound earth models differ in detail, their remarkable general similarity strongly suggests that the LVZ may be a regional characteristic. Furthermore, this agreement lends support and justification for using earthquake sources for detailed structure determinations, opening a previously untapped source of data. It also appears that the straightforward methods used in the receiver structure determination may be superior to that of spectral interpretations since it is very easy to work with isolated phases.

The major low velocity zones discovered here are not without independent supporting evidence. Some of the most direct evidence comes from the refraction profile of Berg et al. (1966) and Johnson and Couch (1970). In the first case, a well developed Pn wave was observed to ranges of about 130 km where it suddenly disappeared. These authors admit several possibilities which include negative velocity gradients. Johnson and Couch (1970) interpreted the disappearance of Pn at the end of their unreversed profile across the Cascades into Puget Sound as the effect of anelastic attenuation. Again, a negative velocity gradient would accomplish the same effect. The great negative isostatic gravity anomaly centered over Puget Sound of Daneš (1969) suggests a very unusual density profile at depth which could conceivably be a result of a LVZ. In a study

of absolute P residuals from the Cannikin blast across the Olympic Mountains and Puget Sound, Lin (1974) stated that the relatively slow residuals observed in the Puget lowlands could be explained by the thickening of a LVZ.

Although it is very tempting to speculate on the geophysical implications of these low velocity zones their interpretation should wait until other regional stations are studied in the manner of COR. As demonstrated in the discussions of Jordan and Frazier (1975), who found a similar result in Canada, petrological arguments yield no useful constraints or unambiguous interpretations.

Conclusions

A major, distinct low velocity zone is inferred in the uppermost mantle under Puget Sound by modelling reflected arrivals in the long period P waveforms from the 1965 Puget Sound earthquake. The LVZ occurs in the depth interval of 41 to 56 km and is sandwiched between layers having mantle velocities. The velocity contrast at the bottom interface of the LVZ must be on the order of 2.5 km/sec as inferred from the theoretical relative P amplitudes from the point dislocation source.

The crust of southern Puget Sound is thin, less than 15 km, and has a thick sediment section near the surface as inferred from the shapes of the pP and sP phases. This is consistent with other

geophysical studies.

The earthquake source parameters determined by the P and SH waveform study are the following: 70° dip to the east; 344° strike; -75° rake, making it a normal dip-slip fault, consistent with previous studies; seismic moment of $1.4 \pm 0.6 \times 10^{26}$ dyne-cm; 63 km depth; and a simple time history represented by a triangular far-field source function with a rise time of 0.5 sec and a fall off of 2.5 sec. The depth is constrained by pP and sP travel times.

The synthetic P and SH waveforms computed from the given source and earth models reproduce the major azimuthal variations which occur in the data waveforms.

A short period stacking procedure utilizing the instantaneous amplitude of the analytic signal is presented and used to find reflected arrivals. An apparent attenuation is found for short period versus long period pP and is correlated with sediment thickness at the reflection point. The amplitude discrepancy yields an effective Q of about 65 for the earth structure above the earthquake.

To substantiate the unusual LVZ structure found for Puget Sound, teleseismic P and S waves records at the WWSSN station COR at Corvallis, Oregon, are used to study the earth structure under the station. From modelling the horizontal and vertical P wave component and vertical SV component in the time domain a slightly shallower

but distinct LVZ is again inferred. The amplitude and timing of Sp, Ps, and the first P multiple suggest a bottom LVZ interface contrast for P and S velocities of about 1.4 and 1.3 km/sec, respectively, and a depth of 45 km. The Poisson ratio for material in the LVZ is constrained by the travel times of these phases and has an unusually high value of 0.33. Changes in the absolute velocities of the Corvallis model are possible but are required to satisfy the large contrasts and high average Poisson ratio.

Using a data set composed of several different teleseismic earthquakes for direct time domain modelling is a useful way to approach the one station method for crustal and upper mantle structure determinations. Although the effective source function is an unknown for most earthquakes, a suitable choice of several simple, deep and intermediate depth events, based on the complexity of the observed vertical P wave, allows for straightforward manipulation and interpretation of the data.

Simultaneous source and structure modelling for simple earthquakes may prove to be a very useful reconnaissance tool in regions of the world where other geophysical studies are lacking or where most techniques fail. Convergence zones with many intermediate depth earthquakes would be most amenable to these techniques since these areas are often isolated with poor local station coverage.

REFERENCES

Abe, K. (1974). Fault parameters determined by near-and far-field data: The Wakaso Bay earthquake of March 26, 1963, Bull. Seism. Soc. Am., 64, 5, 1369-1382.

Abramowitz, M. and I. A. Stegun (1968). Handbook of Mathematical Functions, Dover Publications, New York, 1046 pages.

Aki, K. (1972). Recent results on the mechanism of earthquakes with implications for the prediction and control program Tectonophysics, 14, 227-243.

Alewine, R. W. (1974). Application of linear inversion theory towards the estimation of seismic source parameters, Ph. D. Thesis, California Institute of Technology.

Algermissen, S. T. and S. T. Harding (1965). Preliminary Seismological Report, in The Puget Sound, Washington Earthquake of April 29, 1965, U. S. Department of Commerce, Coast and Geodetic Survey, U. S. Government Printing Office, Washington, 51 pages.

Atwater, T. (1970). Implications of plate tectonics for the Cenozoic tectonic evolution of Western North America, Bull., Geol. Soc. Am., 81, 3513-3536.

Båth, M. and R. Stefánsson (1966). S-P conversion at the base of the crust, Ann. Geofis., 19, 119-130.

Ben-Menahem, A., S. W. Smith, and T. L. Teng (1965). A procedure for source studies from spectra of long-period seismic waves, Bull. Seism. Soc. Am., 55, 203-255.

Ben-Menahem, A. and M. Vered (1973). Extension and interpretation of the Cagniard-Pekeris method for dislocation sources, Bull. Seism. Soc. Am., 63, 1611-1636.

Berg, J. W., L. T. Trembly, D. A. Emilla, J. R. Hutt, J. M. King, L. T. Long, W. R. McKnight, S. K. Sarmah, R. Souders, J. V. Thiruvathukal, D. A. Vossler (1966). Crustal refraction profile, Oregon Coast Range, Bull. Seism. Soc. Am., 56, 1357-1362.

Blackwell, D. D. (1974). Terrestrial heat flow and its implications on the location of geothermal reservoirs in Washington, Energy Resources of Washington, Wash. Div. of Geol. and Earth Resources Inf. Circ. #50.

Bollinger, G. A. (1968). Determination of earthquake fault parameters from long-period P waves, J. Geophys. Res., 73, 2, 785-807.

Bonjer, K. P., K. Fuchs, and J. Wohlenberg (1970). Crustal structure of the East African rift system from spectral response ratios of long-period body waves, Zeitschr. Geophysics., 36, 287-297.

Bracewell, R. (1965). The Fourier Transform and Its Applications, McGraw-Hill Book Co., New York, 381 pages.

Bromery, R. W. and P. D. Snavely, Jr. (1964). Geologic interpretation of reconnaissance gravity and aeromagnetic surveys in northwestern Oregon, U. S. Geological Survey Bull. 1181-N.

Brown, A. S. (1966). Tectonic history of the insular belt of British Columbia, in Symposium on tectonic history and mineral deposits of western cordillera in British Columbia

and neighboring parts of United States: Can. Inst. Min. and Met. Spec. vol. 8, p. 83-100.

Brune, J. N. (1970). Tectonic stress and the spectra of seismic shear waves from earthquakes, J. Geophys. Res., 75, 4997-5009.

Bullen, K. E. (1965). An Introduction to the Theory of Seismology, Cambridge at the University Press, Cambridge, 381 pages.

Burdick, L. J. and D. V. Helmberger (1974). Time functions appropriate for deep earthquakes, Bull. Seism. Soc. Am., 64, 1419-1428.

Cady, W. M. and Tabor, R. W. (1964). Structural history of eastern Olympic Mountains (abstract), U.S. Geological Survey Prof. Paper 501A, A110-A111.

Carpenter, E. W. (1966). Absorption of elastic waves - an operator for a constant Q mechanism, AWRE Report No. 0-43/66, H. M. Stationery Office.

Chandra, U. (1974). Seismicity, earthquake mechanisms, and tectonics along the western coast of North America, from 42°N to 61°N, Bull. Seism. Soc. Am., 64, 1529-1549.

Chapman, C. H. (1974). Generalized ray theory for an inhomogeneous medium, Geophys. J. R. astr. Soc., 36, 673-704.

Crosson, R. S. (1972). Small earhtquakes, structure, and tectonics of the Puget Sound Region, Bull. Seism. Soc. Am., 62, 5, 1133-1171.

Daneš, Z. F. (1969). Gravity results in western Washington, EOS, 50, 348-350.

Daneš, Z. F., M. M. Bonno. E. Brau, W. D. Gilham, T. F. Hoffman, D. Johnson, M. H. Jones, B. Malfait, J. Masten, and G. O. Teague, (1965). Geophysical investigation of the southern Puget Sound area, Washington, J. Geophys. Res., 70, 5573-5580.

Dehlinger, P., E. F. Chiburis, and M. M. Collver (1965). Local travel-time curves and their geologic implications for the Pacific Northwest States, Bull. Seism. Soc. Am., 55, 587-607.

Dehlinger, P., R. W. Couch, M. Gemperle (1968). Continental and oceanic structure from the Oregon coast westward across the Juan de Fuca Ridge, Can. Jour. Earth Sci., 5, 1079-1090.

De Hoop, A. T. (1958). Representation theorems for the displacement in an elastic solid and their application to elastodynamic diffraction theory, Thesis, Technische Hogeschool, Delft.

Dickinson, W. R. (1970). Relations of andesites, granites, and derivative sandstones to arc-trench tectonics, Rev. Geophys. Space Phys., 8, 813-860.

Douglas, A., J. B. Young and J. A. Hudson (1974). Complex P-wave seismograms from simple earthquake sources, Geophys. J. R. astr. Soc., 37, 141-150.

Dutta, T. K. (1969). A note on the source parameter of the Koynanagar earthquake of 10th December 1967, Bull. Seism. Soc., Am., 59, 2, 935-944.

Farnbach, J. S. (1975). The complex envelope in seismic signal analysis, Bull. Seism. Soc. Am., 65, 951-962.

Fernandez, L. M. (1967). Master curves for the response of layered media to compressional seismic waves, Bull. Seism. Soc. Am., 57, 515-543.

Fernandez, L. M. and J. Careaga (1968). The thickness of the crust in crustal United States and La Paz, Bolivia, from the spectrum of longitudinal seismic waves, Bull. Seism. Soc. Am., 58, 711-741.

Fuchs, K. (1966). The transfer function for P-waves for a system consisting of a point source in a layered medium, Bull. Seism. Soc. Am., 56, 75-108.

Fukao, Y. (1970). Focal process of a deep focus earthquake as deduced from long period P and S waves, Bull. Earthquake Res. Inst., 48, 707-727.

Fukao, Y. (1971). Seismic body waves from surface faults, J. Phys. Earth, 19, 271-281.

Fukao, Y. (1972). Source process of a large deep-focus earthquake and its tectonic implications - the western Brazil earthquake of 1963, Phys. Earth Planet. Interiors, 5, 61-76.

Futterman, W. I. (1962). Dispersive body waves, J. Geophys. Res., 67, 5279-5291.

Gorbunova, I. V., N. V. Kondorskaya, and N. S. Landyreva (1970). On the determination of the extent of an Indian shock origin by kinematic data, Geophys. J. R. astr. Soc., 20, 457-471.

Guha, S. K., P. D. Goshari, M. M. Varma, S. P. Agarwal, J. G. Padale, and S. C. Morwadi (1970). Recent seismic disturbances in the Shivajisagar Lake area of the Koyna hydroelectric project, Maharashtra, India, Central Water and Power Research Station Khadakwasla (South), Poona 24 (India), 129 pages.

Guha, S. K., P. D. Gosavari, B. N. P. Agarwal, J. G. Padde, and S. C. Morwadi (1973). Case histories of some artifical crustal disturbances: in press, Proc. Conf. on Int. Colloq. on Seismic Effects of Reservoir Impounding, Royal Soc., London, Elsevier Publ., 27 pages.

Gupta, H., H. Narain, B. K. Rostogi, and I. Mohan (1969). A study of the Koyna earthquake of December 10, 1967, Bull. Seism. Soc. Am., 59, 3, 1149-1162.

Gupta, H. K., B. K. Rostogi, and H. Narain (1971). The Koyna earthquake of December 10, 1967: a multiple seismic event, Bull. Seism. Soc. Am., 61, 1, 167-176.

Hagiwara, T. (1958). A note on the theory of the electromagnetic seismograph, Bull. Earthquake Res. Inst., 36, 139-164.

Hamilton, W., and W. B. Myers (1966). Cenozoic tectonics of the Western United States, Rev. Geophys. and Space Physics, 4, 509-549.

Hanks, T. C. and M. Wyss (1972). The use of body-wave spectra in the determination of seismic-source parameters, Bull. Seism. Soc. Am., 62, 2, 561-589.

Hannon, W. J. (1964). An application of the Haskell-Thomson matrix method to the synthesis of the surface motion due to dilatational waves, Bull. Seism. Soc. Am., 54, 2067-2079.

Harkrider, D. G. (1964). Surface waves in multilayered elastic media I. Rayleigh and Love waves from buried sources in a multilayered elastic half-space, Bull. Seism. Soc. Am., 54, 627-679.

Harkrider, D. G. (1970). Surface waves in multilayered elastic media. Part II. Higher mode spectra and spectral ratios from point sources in plane layered earth models, Bull. Seism. Soc. Am., 60, 1937-1987.

Harkrider, D. G. (1975). Theoretical potentials and displacements for two seismic sources, in preparation.

Haskell, N. A. (1953). The dispersion of surface waves on multilayered media, Bull. Seism. Soc. Am., 43, 17-34.

Haskell, N. A. (1960). Crustal reflection of plane SH waves, J. Geophys. Res., 65, 4147-4150.

Haskell, N. A. (1962). Crustal reflection of plane P and SV waves, J. Geophys. Res., 67, 4751-4767.

Helmberger, D. V. (1968). The crust-mantle transition in the Bering Sea, Bull. Seism. Soc. Am., 58, 179-214.

Helmberger, D. V. (1973a). Numerical seismograms of long-period body waves, from seventeen to forty degrees, Bull. Seism. Soc. Am., 63, 633-646.

Helmberger, D. V. (1973b). On the structure of the low-velocity zone, Geophys. J. R. astr. Soc., 34, 251-263.

Helmberger, D. V. (1974). Generalized ray theory for shear dislocations, Bull. Seism. Soc. Am., 64, 45-64.

Helmberger, D. V. and G. R. Engen (1974). Upper mantle shear structure, J. Geophys. Res., 79, 4017-4028.

Hudson, J. A. (1969a). A quantitative evaluation of seismic signals at teleseismic distances - I radiation from point sources, Geophys. J. R. astr. Soc., 18, 233-249.

Hudson, J. A. (1969b). A quantitative evaluation of seismic signals at teleseismic distances - II Body waves and surface waves from an extended source, Geophys. J. R. astr. Soc., 18, 353-370.

Huntting, M. T., W. A. G. Bennett, V. E. Livingston, Jr., W. S. Moen (1961). Geologic Map of Washington, Washington Department of Conservation, Division of Mines and Geology.

Isacks, B. and P. Molnar (1971). Distribution of stresses in the descending lithosphere from a global survey of focal-mechanism solutions of mantle earthquakes, Rev. Geophys. Space Phys., 9, 103-174.

Johnson, L. R. (1974). Green's functions for Lamb's problem, Geophys. J. R. astr. Soc., 37, 99-131.

Johnson, S. H., and R. W. Couch (1970). Crustal structure in the north Cascade Mountains of Washington and British Columbia from seismic refraction measurements, Bull. Seism. Soc. Am., 60, 1259-1269.

Jordan, T. H. and L. N. Frazier (1975). Crustal and upper mantle structure from Sp phases, J. Geophys. Res., 80, 1504-1518.

Kailasam, L. N., P. R. Pant, S. M. Lahiri, and K. R. M. Simha (1969). Seismic investigations in the Deccan Trap area of Maharashtra and parts of Mysore and Andhes Pradesh, Mem. Geol. Surv. India, 100, 113-116.

Kailasam, L. N., and B. G. K. Murthy (1969). Geophysical investigations in the earthquake affected areas of Koyna, Satora district, Maharashtra, Mem. Geol. Surv. India, 100, 117-122.

Keilis-Borok, V. I. (1957). The determination of earthquake mechanisms using both longitudinal and transverse waves, Ann. Geofis., 10, 105-128.

Keilis-Borok, V. I. (1960). Investigation of the mechanism of earthquakes, Sov. Res. Geophys. 4, 29.

Khattri, K. N. (1970). The Koyna earthquake-seismic studies, Fourth Symposium on Earthquake Engineering, Roorkee, India, 369-374.

Knopoff, L. and F. Gilbert (1959). Radiation from a strike-slip fault, Bull. Seism. Soc. Am., 49, 163-178.

Krishna, J., A. R. Chandrasekaran, and S. S. Saini (1969). Analysis of Koyna accelerogram of December 11, 1967, Bull. Seism. Soc. Am., 59, 1719-1731.

Kurita, T. (1973a). A procedure for elucidating fine structure of the crust and upper mantle from seismological data, Bull. Seism. Soc. Am., 63, 189-209.

Kurita, T. (1973b). Regional variation in the structure of the crust in the central United States from P-wave spectra, Bull. Seism. Soc. Am., 63, 1663-1687.

Lanczos, C. (1961). Linear Differential Operators, D. Van Nostrand Co., Ltd.

Langston, C. A. (1976). A body wave inversion of the Koyna, India, earthquake of 10 December 1967 and some implications for body wave focal mechanisms, J. Geophys. Res., in press.

Langston, C. A. and D. V. Helmberger (1975). A procedure for modelling shallow dislocation sources, Geophys. J. R. astr. Soc., 42, 117-130.

Leblanc, G., S. J. (1967). Truncated crustal transfer functions and fine crustal structure determination, Bull. Seism. Soc. Am., 57, 719-733.

Lee, W. H. and C. B. Raleigh (1969). Fault-plane solutions of the Koyna (India) earthquake, Nature, 223, 172-173.

Leong, L. S. (1975). Crustal structure of the Baltic shield beneath Umea, Sweden, from the spectral behavior of long-period P waves, Bull. Seism. Soc. Am., 65, 113-126.

Lin, J. W. (1974). A study of upper mantle structure in the Pacific Northwest using P waves from teleseisms, Ph. D. Thesis, Univ. of Washington, 98 pp.

Long, R. E., K. Sundaralingam, and P.K.H. Maguire (1973). Crustal structure of the east African Rift Zone, Tectonophysics, 20, 269-281.

McCollom, R. L., and R. S. Crosson (1975). An array study of upper mantle velocity in Washington state, Bull. Seism. Soc. Am., 65, 467-482.

McKenzie, D., and B. Julian (1971). Puget Sound, Washington, earthquake and the mantle structure beneath the northwestern United States, Geol. Soc. Am. Bull., 82, 3519-3524.

Mellman, G., L. Burdick, and D. Helmberger (1975). Determination of source parameters from body wave seismograms (abstract), Earthquake Notes, 46, p. 44.

Minster, J. B., T. H. Jordan, P. Molnar, and E. Haines (1974). Numerical modelling of instantaneous plate tectonics, Geophys. J. R. astr. Soc., 36, 541-576.

Mitchell, B. J. and M. Landisman (1969). Electromagnetic seismograph constants by least-squares inversion, Bull. Seism. Soc. Am., 59, 3, 1335-1348.

Muller, G. (1969). Theoretical seismograms from some types of point sources in layered media. Part III-Single force and dipole sources of arbitrary orientation, Z. Geophys., 35, 347-371.

Narain, H. (1973). Crustal structure of the Indian subcontinent, Tectonophysics, 20, 249-260.

Narain, H. and H. Gupta (1968). Koyna earthquake, Nature, 217, 1138-1139.

Niazi, M. (1969). Source dynamics of the Dasht-e' Bayaz earthquake of August 31, 1968, Bull. Seism. Soc. Am., 59, 1843-1861.

Nuttli, O. W. (1952). The western Washington earthquake of April 13, 1949, Bull. Seism. Soc. Am., 42, 21-28.

Oike, K. (1971). On the nature of the occurrence of intermediate and deep earthquakes, Bull. Disas. Prev. Res. Inst., Kyoto Univ., 21, Part 2, 189, 153-178.

Peck, D. L., A. B. Griggs, H. G. Schlicker, F. G. Wells, and H. M. Dole (1964). Geology of the central and northern parts of the western Cascade Range in Oregon, U. S. Geological Survey Prof. Paper 449.

Phinney, R. A. (1964). Structure of the earth's crust from spectral behavior of long-period body waves, J. Geophys. Res., 69, 2997-3017.

Press, F., (1966). Seismic velocities, in Handbook of Physical Constants, Geol. Soc. Am. Mem. 97.

Raff, A. D., and R. G. Mason (1961). Magnetic survey off the west coast of North America, 40°N latitude to 52°N latitude, Geol. Soc. America Bull., 72, 1267-1270.

Roddick, J. A. (1966). Coast crystalline belt of British Columbia, in Symposium on Tectonic History and Mineral Deposits of Western Cordillera in British Columbia and Neighboring Parts of United States: Can. Inst. Min. and Met. Spec. vol. 8, 73-82.

Sato, Ryosuke (1972). Seismic waves in the near field, J. Phys. Earth, 20, 357-375.

Savage, J. C. (1966). Radiation from a realistic model of faulting, Bull. Seism. Soc. Am., 56, 577-592.

Shor, G. G., P. Dehlinger, H. K. Kirk, and W. S. French (1968). Seismic refraction studies off Oregon and Northern California, J. Geophys. Res., 73, 2175-2194.

Silver, E. A. (1971a). Transitional tectonics and late Cenozoic structure of the continental margin off northernmost California, Geol. Soc. Am. Bull., 82, 1-22.

Silver, E. A. (1971b). Small plate tectonics in the northeastern Pacific, Geol. Soc. Am. Bull., 82, 3491-3496.

Silver, E. A. (1972). Pleistocene tectonic accretion of the continental slope of Washington, Mar. Geol., 13, 239-249.

Singh, D. D., B. K. Rastogi and H. K. Gupta (1975). Surface-wave radiation pattern and source parameters of Koyna earthquake of December 10, 1967, Bull. Seism. Soc. Am., 65, 711-731.

Snavely, P. D. and H. C. Wagner (1963). Tertiary geologic history of western Oregon and Washington, Div. Mines Geol. Report of Inves. #22, 25 pages.

Snavely, P. D., N. S. MacLeod, H. C. Wagner (1968). Tholeiitic and alkalic basalts of the Eocene Siletz River volcanics, Oregon Coast Range, Am. J. Sci, 266, 454-481.

Stauder, W. (1962). The focal mechanisms of earthquakes in Advances in Geophysics, v. 9, ed. by Landsberg, H. E. and Von Mieghem, J., Academic Press, New York and London.

Stuart, D. J. (1961). Gravity study of crustal structure in western Washington, U. S. Geological Survey Prof. Paper 424-C, C-273 to C-276.

Sykes, L. R. (1970). Seismicity of the Indian Ocean and a possible Nascent Island Arc between Ceylon and Australia, J. Geophys. Res., 75, 5041-5055.

Tandon, A. N. and H. M. Chaudhury (1968). Koyna earthquake of December, 1967, India Meterological Dept., Scientific Report 59.

Tatel, H. E. and M. A. Tuve (1955). Seismic exploration of a continental crust, Geol. Soc. Am. Spec. Paper 62, 35-50.

Teng, T. and A. Ben-Menahem (1965). Mechanisms of deep earthquakes from spectrums of isolated body-wave signals, J. Geophys. Res., 70, 5157-5170.

Thiruvathukal, J. V., J. W. Berg, and D. F. Heinrichs (1970). Regional gravity of Oregon, Geol. Soc. Am. Bull., 81, 725-738.

Tobin, D. G., and L. R. Sykes (1968). Seismicity and tectonics of the northeast Pacific Ocean, J. Geophys. Res., 73, 3821-3845.

Tsai, Y-Ben and K. Aki (1971). The Koyna, India, earthquake of December 10, 1967 (abstract), Trans. Am. Geophys. Union, 52, p. 277.

Vine, F. J. (1966). Spreading of the ocean floor: New evidence, Science, 154, 1405-1414.

Vine, F. J. and J. T. Wilson (1965). Magnetic anomalies over a young oceanic ridge off Vancouver Island, Science, 150, 485-489.

Ward, R. W. and K. Aki (1975). Synthesis of teleseismic P waves from sources near sinking lithospheric slabs, Bull. Seism. Soc. Am., 65, 1667-1680.

Wells, F. G. and D. L. Peck (1961). Geologic map of Oregon west of the 121st meridian, Dept. of the Interior, U. S. Geological Survey Miscel. Geologic Investigations Map I-325.

White, W. R. H., and J. C. Savage. (1965). A seismic refraction and gravity study of the earth's crust in British Columbia, Bull. Seism. Soc. Am., 55, 463-486.

Wiggins, R. A. (1972). The general linear inverse problem: implication of surface waves and free oscillations for earth structure, Rev. Geophys. Space Phys., 10, 1, 251-283.

Wilson, J. T. (1965). Transform faults, oceanic ridges and magnetic anomalies southwest of Vancouver Island, Science, 150, 482-485.

Wu, F. T. (1968). Parkfield earthquake of June 28, 1966: Magnitude and source mechanism, Bull. Seism. Soc. Am., 58, 689-709.

Wyss, M. and J. N. Brune (1967). The Alaska earthquake of 28 March 1964: A complex multiple rupture, Bull. Seism. Soc. Am., 57, 5, 1017-1023.

Appendix I

This appendix will outline the details for deriving the first motion approximations from the potentials in equations (1.1). To illustrate these techniques the vertical strike-slip P potential will be utilized. We have, ignoring the multiplicative radiation pattern terms,

$$\bar{\phi} = - K \int_0^\infty k^2 F_\alpha J_2(kr)\, dk \qquad \text{(A1.1)}$$

where,

$$K = - \frac{\mu\, LH\, \bar{D}(\omega)}{4\pi\rho\omega^2}$$

$$F_\alpha = \frac{k\, e^{-\nu_\alpha |z-h|}}{\nu_\alpha}$$

$$\nu_\alpha = (k^2 - k_\alpha^2)^{1/2}$$

$$k = \omega/c$$

$$k_\alpha = \omega/\alpha$$

To make the transformation from the Fourier domain into the Laplace domain let

$$\omega = - is$$
$$k = is\, p \qquad \text{(A1.2)}$$
$$dk = - is\, dp$$

where,

s = Laplace transform variable

p = 1/c, the seismic ray parameter.

Therefore,

$$\hat{\phi} = - \frac{\mu \, LH \, \hat{D}(s) \, s}{4\pi\rho} \int_0^{+i\infty} p^2 \frac{p}{\eta_\alpha} e^{-s\eta_\alpha |z-h|} \, J_2(-ispr) \, dp \tag{A1.3}$$

where,

$$\eta_\alpha = \left(\frac{1}{\alpha^2} - p^2 \right)^{1/2} .$$

Expressing the J_2 Bessel function in terms of the modified Bessel function by (Abramowitz and Stegun, 1968)

$$J_2(-ispr) = - \frac{i}{\pi} K_2(spr) + \frac{i}{\pi} K_2(-spr) \tag{A1.4}$$

we obtain

$$\phi = - \frac{\mu LH\hat{D}(s) \, s}{4\pi\rho} \left\{ I_1 + I_2 \right\} \tag{A1.5}$$

where,

$$I_1 = - \frac{i}{\pi} \int_0^{+i\infty} p^2 \frac{p}{\eta_\alpha} e^{-s\eta_\alpha |z-h|} \, K_2(spr) \, dp \tag{A1.6}$$

$$I_2 = \frac{i}{\pi} \int_0^{+i\infty} p^2 \frac{p}{\eta_\alpha} e^{-s\eta_\alpha |z-h|} \, K_2(-spr) \, dp$$

Changing variables for I_2

$$\left.\begin{aligned} p &= -\,p' \\ dp &= -\,dp' \end{aligned}\right\} \tag{A1.7}$$

$$I_2 = -\frac{i}{\pi}\int_{-i\infty}^{0} p'^2\,\frac{p'}{\eta_\alpha}\,e^{-s\eta_\alpha|z-h|}\,K_2(sp'r)\,dp' \tag{A1.8}$$

Therefore equation (A1.5) becomes

$$\hat{\phi} = -\frac{\mu\,LH\hat{D}(s)\,s}{4\pi\rho}\left\{-\frac{i}{\pi}\int_{-i\infty}^{+i\infty} p^2\,\frac{p}{\eta_\alpha}\,e^{-s\eta_\alpha|z-h|}\,K_2(spr)\,dp\right\} \tag{A1.9}$$

Invoking the Schwarz reflection principle

$$\hat{\phi} = -\frac{M_o}{4\pi\rho}\,\frac{2}{\pi}\,\mathrm{Im}\int_{0}^{+i\infty} p^2\,\frac{p}{\eta_\alpha}\,e^{-s\eta_\alpha|z-h|}\,K_2(spr)\,dp \tag{A1.10}$$

where,

$$M_o = \mu LH\,D_o$$

and

$$\hat{D}(s) = \frac{D_o}{s}\ ,\ \text{step time history.}$$

To find the high frequency or far-field approximation of the exact potential representation, equation (A1.10), consider the asymptotic expansion for the modified Bessel function (Abramowitz and Stegun, 1968)

$$K_2(spr) \sim \sqrt{\frac{\pi}{2spr}}\, e^{-spr}\left\{1 + \frac{15}{8spr} + \cdots\right\} \qquad \text{(A1.11)}$$

Keeping the first term of this expansion gives

$$\hat{\phi} = -\frac{M_o}{4\pi\rho}\frac{2}{\pi}\,\mathrm{Im}\int_0^{+i\infty} p^2\left(\frac{p}{\eta_\alpha}\right)\sqrt{\frac{\pi}{2spr}}\; e^{-s(pr + \eta_\alpha|z-h|)}\, dp \qquad \text{(A1.12)}$$

This type of integral is now in a form which can readily be evaluated by the Cagniard-de Hoop method. Recognizing that if a simple transformation is made

$$t = pr + \eta_\alpha|z-h| \qquad \text{(A1.13)}$$

so that

$$\hat{\phi} = -\frac{M_o}{4\pi\rho}\frac{2}{\pi}\,\mathrm{Im}\int_c p^2\left(\frac{p}{\eta_\alpha}\right)\sqrt{\frac{\pi}{2spr}}\; e^{-st}\left(\frac{dp}{dt}\right)\, dt \qquad \text{(A1.14)}$$

where the contour c is defined by equation (A1.13), the integral appears to be a convolution in the Laplace domain. Inverting to the time domain gives

$$\phi(t) = -\frac{M_o}{4\pi\rho}\frac{1}{\pi}\sqrt{\frac{2}{r}}\frac{1}{\sqrt{t}} * \mathrm{Im}\left\{p^2\,\frac{\sqrt{p}}{\eta_\alpha}\left(\frac{dp}{dt}\right)\right\} \qquad \text{(A1.15)}$$

To form the first motion approximation, equations (1.8), assume that the only fast varying function in the integrand of equation (A1.14) is dp/dt. Expanding in a Taylor series about t_R, the ray arrival time with ray parameter p_o, we obtain (Helmberger, 1968)

$$t = t_R + \frac{dt}{dp}(p-p_o) + \frac{1}{2}\frac{d^2t}{dp^2}(p-p_o)^2 \qquad \text{(A1.16)}$$

Since,

$$\frac{dt}{dp} = 0 \quad \text{at} \quad p = p_o \qquad \text{(A1.17)}$$

$$t = t_R + \frac{1}{2}\frac{d^2t}{dp^2}(p-p_o)^2$$

and

$$p-p_o = \frac{\sqrt{2}\ (t-t_R)^{1/2}}{\left(\frac{d^2t}{dp^2}\right)^{1/2}} \qquad \text{(A1.18)}$$

Therefore, the derivative is

$$\frac{dp}{dt} = \frac{(t-t_R)^{-1/2}}{\left(2\frac{d^2t}{dp^2}\right)^{1/2}} \qquad \text{(A1.19)}$$

Using equation (A1.13)

$$\frac{dt^2}{dp^2} = -\frac{|z-h|}{\alpha^2 \eta_\alpha^3} \tag{A1.20}$$

so that

$$\frac{dp}{dt} = \frac{(t-t_R)^{-1/2}}{\left(-\frac{2|z-h|}{\alpha^2 \eta_\alpha^3}\right)^{1/2}} \tag{A1.21}$$

Substituting (A1.21) into equation (A1.15) we obtain

$$\phi(t) = -\frac{M_o}{4\pi\rho}\sqrt{\frac{1}{r}}\, p^2 \sqrt{\frac{p\eta_\alpha}{|z-h|}}\; H(t-t_R) \tag{A1.22}$$

since,

$$\frac{1}{\sqrt{t}} * \frac{1}{(t-t_R)^{1/2}} = \pi H(t-t_R) \tag{A1.23}$$

Recognizing that

$$\left.\begin{aligned} t_R &= \frac{R}{\alpha} \\ \eta_\alpha &= \frac{|z-h|}{\alpha R} = \frac{\cos i}{\alpha} \\ p &= \frac{r}{\alpha R} = \frac{\sin i}{\alpha} \\ R^2 &= (z-h)^2 + r^2 \\ i &= \text{vertical incidence angle} \end{aligned}\right\} \tag{A1.24}$$

we finally obtain the potential form

$$\phi(t) = - \frac{M_o}{4\pi\rho} p^2 \frac{H(t-R/\alpha)}{R} \qquad \text{(A1.25)}$$

For converted phases, such as pS, expression (A1.15) becomes

$$\Omega(t) = - \frac{M_o}{4\pi\rho} \frac{1}{\pi} \sqrt{\frac{2}{r}} \frac{1}{\sqrt{t}} * \text{Im} \left\{ p^2 \frac{\sqrt{p}}{\eta_\alpha} \left(\frac{dp}{dt} \right) R_{PS} \right\} \qquad \text{(A1.26)}$$

where R_{PS} is the appropriate reflection coefficient. The form of dp/dt will be the same as equation (A1.19) except that

$$\frac{d^2t}{dp^2} = - \frac{h}{\alpha^2 \eta_\alpha^3} - \frac{z}{\beta^2 \eta_\beta^3} \qquad \text{(A1.27)}$$

Assuming that z >>h

$$\frac{d^2t}{dp^2} \simeq - \frac{z}{\beta^2 \eta_\beta^3} \qquad \text{(A1.28)}$$

Therefore,

$$\Omega(t) = - \frac{M_o}{4\pi\rho} p^2 \left(\frac{\eta_\beta}{\eta_\alpha} \right) R_{PS} \beta \sqrt{\frac{1}{r}} \sqrt{\frac{p\eta_\beta}{z}} H(t-t_R) \qquad \text{(A1.29)}$$

Again recognizing

$$\left.\begin{aligned} p &= \frac{r}{\beta R} \\ \eta_\beta &= \frac{z}{\beta R} \\ t_R &\simeq R/\beta \end{aligned}\right\} \qquad \text{(A1.30)}$$

we obtain

$$\Omega(t) = -\frac{M_o}{4\pi\rho}\, p^2 \left(\frac{\eta_\beta}{\eta_\alpha}\right) R_{PS}\, \frac{H(t - R/\beta)}{R} \qquad \text{(A1.31)}$$

Appendix II

Analytic Partial Derivatives for the Body Wave Inversion Problem

The equation for a seismogram, g(t), is given by eq. (1.54); with summation convention

$$g(t) = B_j S_j(t-\tau_{L_j}) * \left\{ \alpha_{ij} \quad \delta(t-\tau_{s_{ij}}) \right\} * I(t)*Q(t) \qquad \text{(A2.1)}$$

where

j = index of the j^{th} point dislocation

i = index of the i^{th} ray

B_j = relative moment of the j^{th} source to that of the 1st source

$S_j(t-\tau_{L_j})$ = parameterized time function of the j^{th} source

τ_{L_j} = relative time lag of the j^{th} source relative to the 1st source

α_{ij} = amplitude of the i^{th} ray, j^{th}, source

$\delta(t-\tau_{s_{ij}})$ = lagged Dirac delta function

$\tau_{s_{ij}}$ = relative travel time of the i^{th} ray, j^{th} source

$*$ = convolution operator

We will want to find analytic derivatives of g(t) with respect to the parameterization to use in equation (1.53). The terms in equation (A2.1), to varying degrees, will all be functions of the source orientation, position, and time history parameterization.

Explicitly,

$$B_j = B_j$$

$$S_j(t) = S(t, \delta t_{1_j}, \delta t_{2_j}, \delta t_{3_j})$$

$$\tau_{L_j} = \tau_L(X_j, Y_j, T_{L_j}, AZ_j) \qquad \text{(A2.2)}$$

$$\alpha_{ij} = \alpha_i(\theta_j, \lambda_j, \delta_j)$$

$$\tau_{s_{ij}} = \tau_{s_i}(HS_j)$$

where

$\delta t_{1_j}, \delta t_{2_j}, \delta t_{3_j}$ = parameters of the trapezoidal time function

X_j, Y_j = lateral position of j^{th} source relative to the first source in km, north and east are positive, respectively.

TL_j = absolute time lag between the j^{th} and first sources

AZ_j = station azimuth, from north, from the j^{th} source

θ_j = strike of j^{th} station from the fault end

λ_j = rake of j^{th} source

δ_j = dip of j^{th} source

HS_j = depth of j^{th} source

Neglecting the I(t)*Q(t) terms, the derivatives per j and, implicitly, per station are given by the following straightforward developments (with summation conventions):

$$\frac{\partial g(t)}{\partial B} = S(t - \tau_L) * \left[\alpha_i \, \delta(t-\tau_{s_i}) \right] \tag{A2.3}$$

$$\frac{\partial g(t)}{\partial HS} = B \, S(t-\tau_L) * \left[\alpha_i \, \dot{\delta}(t-\tau_{S_i}) \left(- \frac{\partial \tau_{s_i}}{\partial HS} \right) \right] \tag{A2.4}$$

using

$$\int_{-\infty}^{+\infty} h(t) \, \dot{\delta}(t-\tau) \, dt = \int_{-\infty}^{+\infty} \dot{h}(t) \, \delta(t-\tau) \, dt \tag{A2.5}$$

$$\frac{\partial g(t)}{\partial HS} = B \, \dot{S}(t-\tau_L) * \left[\alpha_i \left(- \frac{\partial \tau_{s_i}}{\partial HS} \right) \delta(t-\tau_{s_i}) \right] \tag{A2.6}$$

where

$$\left(- \frac{\partial \tau_{s_i}}{\partial HS} \right) = \mp \eta_v \qquad \begin{array}{l} - \text{ upgoing rays} \\ + \text{ downgoing rays} \end{array} \tag{A2.7}$$

$$\frac{\partial g(t)}{\partial \lambda} = B \cdot S(t-\tau_L) * \left[\left(\frac{\partial \alpha_i}{\partial \lambda} \right) \delta(t-\tau_{s_i}) \right] \tag{A2.8}$$

where, taking a P wave for an example,

$$\frac{\partial \alpha_i}{\partial \lambda} = \frac{\partial (C_1 \cdot A_1 + C_2 \cdot A_2 + C_3 \cdot A_3)}{\partial \lambda} \tag{A2.9}$$

so,

$$\frac{\partial A_1}{\partial \lambda} = - \sin 2\theta \sin \lambda \sin \delta + \frac{1}{2} \cos 2\theta \cos \lambda \sin 2\delta$$

$$\frac{\partial A_2}{\partial \lambda} = - \cos \theta \sin \lambda \cos \delta - \sin \theta \cos \lambda \cos 2\delta$$

$$\frac{\partial A_3}{\partial \lambda} = \frac{1}{2} \cos \lambda \sin 2\delta \tag{A2.10}$$

$$\frac{\partial A_4}{\partial \lambda} = - \cos 2\theta \sin \lambda \sin \delta - \frac{1}{2} \sin 2\theta \cos \lambda \sin 2\delta$$

$$\frac{\partial A_5}{\partial \lambda} = \sin \theta \sin \lambda \cos \delta - \cos \theta \cos \lambda \cos 2\delta$$

$$\frac{\partial g(t)}{\partial \delta} = B \cdot S(t - \tau_L) * \left[\left(\frac{\partial \alpha_i}{\partial \delta} \right) \delta(t - \tau_{s_i}) \right] \tag{A2.11}$$

likewise, by a similar argument as eq. (A2.8),

$$\frac{\partial A_1}{\partial \delta} = \sin 2\theta \cos \lambda \cos \delta + \cos 2\theta \sin \lambda \cos 2\delta$$

$$\frac{\partial A_2}{\partial \delta} = - \cos \theta \cos \lambda \sin \delta + 2 \sin \theta \sin \lambda \sin 2\delta$$

$$\frac{\partial A_3}{\partial \delta} = \sin\lambda \cos 2\delta \qquad \text{(A2.12)}$$

$$\frac{\partial A_4}{\partial \delta} = \cos 2\theta \cos \lambda \cos \delta - \sin 2\theta \sin \lambda \cos 2\delta$$

$$\frac{\partial A_5}{\partial \delta} = \sin\theta \cos \lambda \sin \delta + 2 \cos \theta \sin \lambda \sin 2\delta$$

$$\frac{\partial g(t)}{\partial \theta} = A \cdot S(t-\tau_L) * \left[\left(\frac{\partial \alpha_i}{\partial \theta} \right) \delta(t-\tau_{s_i}) \right]$$

$$+ A \cdot \dot{S}(t-\tau_L) \left(- \frac{\partial \tau_L}{\partial \theta} \right) * \left[\alpha_i \ \delta(t-\tau_{s_i}) \right] \qquad \text{(A2.13)}$$

Again, by similar argument to eq. (A2.8),

$$\frac{\partial A_1}{\partial \theta} = 2 \cos 2\theta \cos \lambda \sin \delta - \sin 2\theta \sin \lambda \sin 2\delta$$

$$\frac{\partial A_2}{\partial \theta} = - \sin\theta \cos\lambda \cos \delta - \cos \theta \sin \lambda \cos 2\delta$$

$$\frac{\partial A_3}{\partial \theta} = 0 \qquad \text{(A2.14)}$$

$$\frac{\partial A_4}{\partial \theta} = - 2 \sin 2\theta \cos \lambda \sin \delta - \cos 2\theta \sin \lambda \sin 2\delta$$

$$\frac{\partial A_5}{\partial \theta} = - \cos \theta \cos \lambda \cos \delta + \sin \theta \sin \lambda \cos 2\delta$$

and

$$- \frac{\partial \tau_L}{\partial \theta} = p\left[- X \sin (\theta + STRK) + Y \cos (\theta + STRK)\right] \qquad \text{(A2.15)}$$

where,

p = ray parameter

STRK = strike of the fault measured clockwise from north.

$$\frac{\partial g(t)}{\partial X} = B \cdot \dot{S}(t-\tau_L) \left(- \frac{\partial \tau_L}{\partial X}\right) * \left[\alpha_i \, \delta(t-\tau_{s_i})\right] \qquad \text{(A2.16)}$$

where,

$$\left(\frac{\partial \tau_L}{\partial X}\right) = - P \cos (AZ) \qquad \text{(A2.17)}$$

$$\frac{\partial g(t)}{\partial Y} = B \cdot \dot{S}(t-\tau_L) \left(- \frac{\partial \tau_L}{\partial Y} \right) * \left[\alpha_i \, \delta(t-\tau_{s_i}) \right] \qquad \text{(A2.18)}$$

where

$$\left(- \frac{\partial \tau_L}{\partial Y} \right) = - P \sin (AZ) \qquad \text{(A2.19)}$$

$$\frac{\partial g(t)}{\partial TL} = B \cdot \dot{S}(t-\tau_L) * \left[\alpha_i \, \delta(t-\tau_{s_i}) \right] \qquad \text{(A2.20)}$$

Finally,

$$\frac{\partial g(t)}{\partial \delta t_\ell} = B \cdot \frac{\partial S(t-\tau_L)}{\partial \delta t_\ell} * \left[\alpha_i \, \delta(t-\tau_{s_i}) \right] \quad (\ell = 1,2,3) \qquad \text{(A2.21)}$$

It proved to be computationally convenient to take the time function derivatives, with respect to the δt's, in the frequency domain. Remembering that the time function is normalized to unit area (equation 1.14) we have,

$$S(t) = D(\delta t_\ell) \cdot f(t, \delta t_\ell) \qquad (\ell = 1,2,3) \qquad \text{(A2.22)}$$

where,

$$D(\delta t_\ell) = \left(\frac{1}{2} \delta t_1 + \delta t_2 + \frac{1}{2} \delta t_3 \right)^{-1} \qquad \text{(A2.23)}$$

therefore,

$$\frac{\partial S(t)}{\partial \delta t_\ell} = \frac{\partial D(\delta t_\ell)}{\partial \delta t_\ell} \cdot f(t, \delta t_\ell) + D \, \frac{\partial f(t, \delta t_\ell)}{\partial \delta t_\ell} \qquad \text{(A2.24)}$$

Computing the partials of $D(\delta t_\ell)$,

$$\frac{\partial D}{\partial \delta t_1} = \frac{\partial D}{\partial \delta t_3} = -\frac{1}{2} D^2$$

$$\frac{\partial D}{\partial \delta t_2} = -D^2 \qquad \text{(A2.25)}$$

Since the δt_ℓ are independent from t we can express the derivatives in the frequency domain by

$$\frac{\partial F(\omega)}{\partial \delta t_\ell} = \frac{\partial \text{ Re } F(\omega)}{\partial \delta t_\ell} + i \frac{\partial \text{ Im } F(\omega)}{\partial \delta t_\ell} \qquad (\ell = 1,2,3) \qquad \text{(A2.26)}$$

where $F(\omega)$ is the Fourier transform of $f(t)$.

These derivatives are:

$$\frac{\partial \ \mathrm{Re}\ F(\omega)}{\partial \delta t_1} = \frac{(1-\cos\ \omega\delta t_1)}{\omega^2 \delta t_1^2}$$

$$+ \frac{1}{\omega}\left\{ - \frac{\sin\ \omega\delta t_1}{\delta t_1} + \frac{1}{\delta t_3}\Big(\sin\ \omega(\delta t_1 + \delta t_2 + \delta t_3) - \sin\ \omega(\delta t_1 + \delta t_2)\Big)\right\}$$

$$\frac{\partial\ \mathrm{Im}\ F(\omega)}{\partial \delta t_1} = \frac{\sin\ \omega\delta t_1}{\omega^2 \delta t_1^2} - \frac{1}{\omega}\left\{\frac{\cos\ \omega\delta t_1}{\delta t_1} + \frac{1}{\delta t_3}\right.$$

$$\cdot \ \left. -\Big(\cos\ \omega(\delta t_1 + \delta t_2 + \delta t_3) + \cos\ \omega(\delta t_1 + \delta t_2)\Big)\right\}$$

$$\frac{\partial\ \mathrm{Re}\ F(\omega)}{\partial \delta t_2} = \frac{1}{\omega \delta t_3}\Big(\sin\ \omega(\delta t_1 + \delta t_2 + \delta t_3) - \sin\ \omega(\delta t_1 + \delta t_2)\Big)$$

$$\frac{\partial\ \mathrm{Im}\ F(\omega)}{\partial \delta t_2} = \frac{1}{\omega \delta t_3}\Big(\cos\ \omega(\delta t_1 + \delta t_2 + \delta t_3) - \cos\ \omega(\delta t_1 + \delta t_2)\Big)$$

$$\frac{\partial\ \mathrm{Re}\ F(\omega)}{\partial \delta t_3} = \frac{1}{\omega^2 \delta t_3^2}\Big(\cos\ \omega(\delta t_1 + \delta t_2 + \delta t_3) - \cos\ \omega(\delta t_1 + \delta t_2)\Big)$$

$$+ \frac{1}{\omega \delta t_3}\sin\ \omega(\delta t_1 + \delta t_2 + \delta t_3)$$

$$\frac{\partial\ \mathrm{Im}\ F(\omega)}{\partial \delta t_3} = \frac{1}{\omega^2 \delta t_3^2}\Big(-\sin\ \omega(\delta t_1 + \delta t_2 + \delta t_3) + \sin\ \omega(\delta t_1 + \delta t_2\Big)$$

$$+ \frac{1}{\omega t_3}\cos\ \omega(\delta t_1 + \delta t_2 + \delta t_3)$$

(A2.27)